

ADVANCED TORQUE RIPPLE REDUCTION  
METHODS IN SWITCHED RELUCTANCE  
MOTOR DRIVES

ADVANCED TORQUE RIPPLE REDUCTION METHODS IN  
SWITCHED RELUCTANCE MOTOR DRIVES

BY

ZEKUN XIA, M.A.Sc, B.Eng.

A THESIS

SUBMITTED TO THE DEPARTMENT OF ELECTRICAL & COMPUTER ENGINEERING

AND THE SCHOOL OF GRADUATE STUDIES

OF MCMASTER UNIVERSITY

IN PARTIAL FULFILMENT OF THE REQUIREMENTS

FOR THE DEGREE OF

DOCTOR OF PHILOSOPHY

© Copyright by Zekun Xia, November 2020

All Rights Reserved

Doctor of Philosophy (2020)  
(Electrical and Computer Engineering)

McMaster University  
Hamilton, Ontario, Canada

TITLE: Advanced Torque Ripple Reduction Methods in Switched  
Reluctance Motor Drives

AUTHOR: Zekun Xia  
M.A.Sc., (Electrical Engineering)  
B.Eng. (Electrical Engineering)  
Northwestern Polytechnical University, Xi'an, China

SUPERVISOR: Ali Emadi, Professor  
Ph. D. (Texas A&M University)  
Fellow IEEE, SAE, and NAI  
Canada Excellence Research Chair Laureate

NUMBER OF PAGES: xix, 191

谨以此献给我的父母，夏赋池 刘宝珠

*To My Dad, Fuchi Xia,*

*My Mom, Baozhu Liu*

# Abstract

This thesis presents advanced torque control methods for torque ripple reduction and performance improvement in switched reluctance motor (SRM) drives.

A new offline torque sharing function (TSF) method is proposed for torque ripple reduction in SRMs. The proposed TSF achieves lower current tracking error by establishing a new current reference generation strategy. The phase current reference is first derived from the torque command using offline calculations and also from the phase current response that is obtained from the dynamic model of the SRM. Then, an optimization problem is formulated to shape the current reference for the objective of minimizing the torque ripple and copper losses, while maintaining the required average output torque at the given operating speed. The dynamic simulation of the SRM model is also utilized in the optimization problem.

A new online TSF method is proposed for torque ripple reduction in SRMs. The proposed TSF takes the current dynamics and induced electromotive force into account by establishing a new online current profile generation technique. First, a primary phase current reference derived from the torque reference is applied to the SRM. Then, the decaying phase current after the turn-off angle is sampled, and it is used to update the

current reference. A new online optimization strategy is performed to shape the current reference during the operation of the machine. Owing to the proposed current profile generation technique, the optimization process is decoupled to independently minimize the torque ripple by optimizing the turn-on angle and minimizing copper losses by optimizing the turn-off angle.

Compared to the conventional TSFs and existing optimization-based TSFs, the proposed two TSFs achieve accurate torque control, improved torque-speed capability, reduced torque ripple, and better current tracking performance. All the proposed TSF methods are validated by both simulations and experiments on a 3-phase, 12/8 SRM.

# Acknowledgments

First and foremost, I would like to express my sincere appreciation to my supervisor, Dr. Ali Emadi, for providing me his guidance, support, and encouragement throughout my Ph. D. study. It has been a great honor to be one of his Ph. D. students, and I take pride in being part of McMaster Automotive Research Centre (MARC).

Special thanks to Dr. Berker Bilgin for his helpful and insightful suggestions in my research. I was fortunate to attend Dr. Bilgin's course on switched reluctance machines. He is always enthusiastic and helpful and has offered me numerous advices on machine design, control, and testing. Special thanks to my committee members, Dr. Mehdi Narimani and Dr. Yingye Yang, for their valuable comments and discussions throughout my Ph. D. program.

I would also like to express my appreciation to Dr. Shamsuddeen Nalakath for providing me insightful suggestions on permanent magnet machines. Special thanks to Gaoliang Fang, Robert Lau, Christopher Mak, Dianxun Xiao, Yuhang Yang, Silvio Filho, and Jianbin Liang for assisting with my experimental setup.

I would also like to thank the BorgWarner team at MARC: Yu Miao, Deqiang Wang, Giorgio Pietrini, Rasul Tarvirdilu Asl, Jing Zhao, Xueqing Wang, Guanghan Zhao, Parisa M. Shamsabadi, Alice Dong, Xiaoqiang Guo, Haoming Li, and Helia Jamali. It was an honour to work with you as part of the team.

Finally, I would express my deepest love and gratitude to my parents for their endless love, care, and support. Special thanks to Yihui Li for her understanding, trust and support.

# Contents

<b>Abstract</b>	<b>iv</b>
<b>Acknowledgments</b>	<b>vi</b>
<b>Contents</b>	<b>viii</b>
<b>List of Figures</b>	<b>xiii</b>
<b>List of Tables</b>	<b>xix</b>
<b>Chapter 1 Introduction</b>	<b>1</b>
1.1 Background	1
1.2 Motivation	7
1.3 Contributions	10
1.4 Outline of the Thesis	11
<b>Chapter 2 Fundamentals of Switched Reluctance Machines</b>	<b>14</b>
2.1 Introduction	14
2.2 Electromagnetic Energy Conversion	15

2.2.1	Equivalent Circuit of SRM .....	15
2.2.2	Power Conversion and Torque Generation Mechanism .....	16
2.3	Power Converters for Switched Reluctance Machines.....	18
2.3.1	Asymmetric Half-bridge Converter .....	18
2.3.2	Dissipative Converter .....	21
2.3.3	Energy Recovery Converter .....	22
2.4	Basic Control Methods for Switched Reluctance Machine .....	23
2.4.1	Single-pulse Voltage Control .....	24
2.4.2	Hysteresis Current Control .....	25
2.4.3	PWM Voltage Control.....	26
<b>Chapter 3 Torque Ripple Reduction Methods for Switched Reluctance Motor Drives</b>		
	.....	<b>28</b>
3.1	Introduction.....	28
3.2	Motor Geometry Improvements .....	30
3.3	Motor Drive Developments .....	31
3.4	Control Methods Developments .....	32
3.4.1	Direct Torque Control.....	33
3.4.2	Direct Instantaneous Torque Control.....	34
3.4.3	Conduction Angle Control.....	35

3.4.4	Average Torque Control .....	35
3.4.5	Model Predictive Control .....	36
3.4.6	Intelligent Control.....	37
3.4.7	Iterative Learning Control .....	39
3.4.8	Torque Sharing Function .....	40
3.5	Conclusion .....	41
<b>Chapter 4 Design and Implementation of a Switched Reluctance Motor Drive Setup</b>		
	.....	<b>42</b>
4.1	Introduction.....	42
4.2	Device Selection .....	43
4.2.1	Dynamometer Drive .....	45
4.2.2	Torque Transducer.....	46
4.2.3	Shaft Couplings .....	46
4.3	Mechanical and Electrical Design .....	47
4.4	Measurement of Static Electromagnetic Characteristics of SRM .....	52
4.4.1	Static Flux Linkage Characteristic.....	52
4.4.2	Static Torque Characteristic .....	55
4.5	Conclusion .....	57

<b>Chapter 5</b>	<b>A New Torque Sharing Function Method For Switched Reluctance Machines With Lower Current Tracking Error.....</b>	<b>58</b>
5.1	Introduction.....	58
5.2	Conventional and Optimization-based TSFs .....	59
5.3	Proposed Offline TSF.....	69
5.4	Simulation Evaluation .....	82
5.5	Experimental Validation.....	94
5.6	Conclusion .....	103
<b>Chapter 6</b>	<b>An Online Torque Sharing Function Involving Current Dynamics for Switched Reluctance Motor Drives .....</b>	<b>104</b>
6.1	Introduction.....	104
6.2	Induced EMF and Current Dynamics .....	105
6.3	Proposed Online TSF.....	109
6.3.1	Outer Optimization Loop: Copper Loss Reduction.....	110
6.3.2	Inner Optimization Loop: Torque Ripple Reduction.....	113
6.4	Simulation Evaluation .....	121
6.5	Experimental Validation.....	135
6.6	Conclusion .....	149

<b>Chapter 7</b>	<b>Ripple-Free Torque-Speed Characteristic of Switched Reluctance</b>	
<b>Machines</b>	.....	<b>150</b>
7.1	Introduction.....	150
7.2	Torque-Speed Characteristic of IPMSMs.....	151
7.3	Torque-Speed Characteristic of SRMs .....	154
7.4	Ripple-Free Torque-Speed Characteristic of SRMs .....	159
7.5	Conclusion .....	168
<b>Chapter 8</b>	<b>Conclusions and Future Work .....</b>	<b>169</b>
8.1	Conclusions.....	169
8.2	Future Work.....	171
<b>Reference</b>	.....	<b>173</b>

# List of Figures

Fig. 2.1. The equivalent circuit for one phase of SRM.....	16
Fig. 2.2. Asymmetric half-bridge converter for 3-phase SRMs. ....	19
Fig. 2.3. Three-phase asymmetric half-bridge converter constructed by standard industrial switch modules. (a). H-bridge. (b). 3-phase full bridge modules. ....	20
Fig. 2.4. Three-phase dissipative converter. ....	21
Fig. 2.5. Three-phase C-dump converter. ....	23
Fig. 2.6. Three-phase bifilar converter.....	23
Fig. 2.7. Phase current profiles with SPV control under different $\theta_{on}$ and $\theta_{off}$ .....	24
Fig. 2.8. Schematic diagram of the hysteresis current control method.....	25
Fig. 2.9. Phase current waveforms with HCC under different current references.....	26
Fig. 2.10. Schematic diagram of the PWM voltage control method.....	26
Fig. 2.11. Phase current waveforms with PWM control under different duty ratios.....	27
Fig. 3.1. Classification of the torque ripple reduction methods for SRM drives.....	29
Fig. 3.2. An integrated modular converter for 3-phase SRM [70].....	32
Fig. 3.3. Block diagram of DTC method for 3-phase SRM [81], [82]. ....	33
Fig. 3.4. Block diagram of the DITC method [85]. ....	34

Fig. 3.5. Block diagram of average torque control method [96], [97].	36
Fig. 3.6. Block diagram of model predictive control [99].	37
Fig. 3.7. Block diagram of the fuzzy logic control method [106].	38
Fig. 3.8. Block diagram of the fuzzy control method in [108].	39
Fig. 3.9. Block diagram of an ILC-based current controller [53].	40
Fig. 4.1. Schematic diagram of the experimental setup.	43
Fig. 4.2. 3D model of SRMs. (a). SRM-I. (b). SRM-II.	47
Fig. 4.3. Faceplates for SRMs. (a). For SRM-I. (b). For SRM-II. (c). For dyno. (d). Angle bracket.	48
Fig. 4.4. Stepped shaft.	48
Fig. 4.5. 3D model of the torque sensor and its clamping holder.	49
Fig. 4.6. Overview of the SRM experimental setup design.	50
Fig. 4.7. Picture of the final experimental setup.	50
Fig. 4.8. 3D model of inverter design. (a). Enclosure. (b). Inverter model [111].	51
Fig. 4.9. Picture of the flux linkage measurement platform.	53
Fig. 4.10. Measurement of the phase winding resistance.	54
Fig. 4.11. Measurement result of flux linkage.	55
Fig. 4.12. Static torque characteristic.	56
Fig. 5.1. Phase torque profiles of the linear TSF.	60
Fig. 5.2. Phase torque profiles of the cubic TSF.	61
Fig. 5.3. Phase torque profiles of the sinusoidal TSF.	62
Fig. 5.4. Phase torque profiles of the exponential TSF.	63

Fig. 5.5. Flowchart for the TSF in [41].	66
Fig. 5.6. Phase current references for the TSF in [41] with varying weight parameters. (a). Incoming and outgoing phase current references. (b). Phase current references in one electrical cycle.	68
Fig. 5.7. Flowchart for the proposed offline TSF.	70
Fig. 5.8. Reference current profile from each step. (a) Step I. (b) Step II. (c) Step III. (d) Step IV. (e) Inductance profile.	72
Fig. 5.9. Effect of the conduction angle. (a) Varying $\theta_{on}$ when $\theta_{off} = 160^\circ$ . (b) Varying $\theta_{off}$ when $\theta_{on} = 10^\circ$ .	81
Fig. 5.10. An example of the final current reference.	82
Fig. 5.11. Measured characteristics of the adopted SRM.	83
Fig. 5.12. Dynamic simulation results (Speed = 400 r/min, $T_{ref} = 20$ Nm). (a). Linear TSF. (b) Cubic TSF. (c). TSF in [41]. (d). Proposed TSF.	86
Fig. 5.13. Dynamic simulation results (Speed = 1000 r/min, $T_{ref} = 20$ Nm). (a). Linear TSF. (b) Cubic TSF. (c). TSF in [41]. (d). Proposed TSF.	89
Fig. 5.14. Quantitative comparison among the conventional TSFs, TSF in [41] and the proposed TSF. (a) Average torque. (b). RMS torque ripple. (c). RMS phase current. (d). Torque ripple percentage.	91
Fig. 5.15. Dynamic simulation results (Speed = 1500 r/min, $T_{ref} = 5$ Nm). (a). Linear TSF. (b) Cubic TSF. (c). TSF in [41]. (d). Proposed TSF.	93
Fig. 5.16. The picture of the experimental setup.	95

Fig. 5.17. Experimental results (Speed = 400 r/min, $T_{ref} = 20$ Nm). (a). Linear TSF. (b) Cubic TSF. (c). TSF in [41]. (d). Proposed TSF.....	97
Fig. 5.18. Experimental results (Speed = 1000 r/min, $T_{ref} = 20$ Nm). (a). Linear TSF. (b) Cubic TSF. (c). TSF in [41]. (d). Proposed TSF.....	100
Fig. 5.19. Experimental results (Speed = 1500 r/min, $T_{ref} = 5$ Nm). (a). Linear TSF. (b) Cubic TSF. (c). TSF in [41]. (d). Proposed TSF.....	102
Fig. 6.1. Dynamic profiles of the phase current, torque, and induced EMF under different operating speeds and the same conduction angles. ....	106
Fig. 6.2. Dynamic profiles of the phase current, torque, and induced EMF with different firing angles at the same operating speed. ....	108
Fig. 6.3. Flowchart for the proposed online TSF. ....	112
Fig. 6.4. Block diagram for the inner loop optimization.....	114
Fig. 6.5. Current reference generated in the inner optimization loop. (a) Step A. (b) Step B. (c). Adaptive turn-on angle adjustment.....	118
Fig. 6.6. Simulation results at 500 r/min and 10 Nm torque reference. (a) Linear TSF, $\theta_{on} = 40.42^\circ$ , $\theta_{ov} = 16.37^\circ$ . (b). Sinusoidal TSF, $\theta_{on} = 39.23^\circ$ , $\theta_{ov} = 4.66^\circ$ . (c). Cubic TSF, $\theta_{on} = 39.96^\circ$ , $\theta_{ov} = 6.55^\circ$ . (d). Exponential TSF, $\theta_{on} = 41.36^\circ$ , $\theta_{ov} = 15.77^\circ$ . (e). TSF in [41], $\sigma = 1.75$ . (f). Proposed online TSF, $\theta_{on} = 39.41^\circ$ , $\theta_{off} = 163.36^\circ$ . ....	125
Fig. 6.7. Simulation results at 1000 r/min and 10 Nm torque reference. (a) Linear TSF, $\theta_{on} = 29.84^\circ$ , $\theta_{ov} = 28.53^\circ$ . (b). Sinusoidal TSF, $\theta_{on} = 29.18^\circ$ , $\theta_{ov} = 28.81^\circ$ . (c). Cubic TSF, $\theta_{on} = 25.86^\circ$ , $\theta_{ov} = 33.91^\circ$ . (d). Exponential TSF, $\theta_{on} = 31.51^\circ$ , $\theta_{ov} = 20.53^\circ$ . (e). TSF in [41], $\sigma = 38.79$ . (f). Proposed online TSF, $\theta_{on} = 34.07^\circ$ , $\theta_{off} = 162.05^\circ$ . ....	129

Fig. 6.8. Simulation comparison between different TSFs. (a). Average torque. (b). rms torque ripple. (c). rms current. (d). Torque ripple percentage. ....	131
Fig. 6.9. Simulation results at 1500 r/min and 5 Nm torque reference. (a) Linear TSF, $\theta_{on} = 24.24^\circ$ , $\theta_{ov} = 35.27^\circ$ . (b). Sinusoidal TSF, $\theta_{on} = 17.49^\circ$ , $\theta_{ov} = 38.93^\circ$ . (c). Cubic TSF, $\theta_{on} = 14.99^\circ$ , $\theta_{ov} = 3.81^\circ$ . (d). Exponential TSF, $\theta_{on} = 15.07^\circ$ , $\theta_{ov} = 1.95^\circ$ . (e). TSF in [41], $\sigma = 715.24$ . (f). Proposed online TSF, $\theta_{on} = -23.97^\circ$ , $\theta_{off} = 126.95^\circ$ .....	134
Fig. 6.10. Photograph of the experimental setup. ....	136
Fig. 6.11. Experimental results at 500 r/min and 10 Nm torque reference. (a) Linear TSF, $\theta_{on} = 40.42^\circ$ , $\theta_{ov} = 16.37^\circ$ . (b). Sinusoidal TSF, $\theta_{on} = 39.23^\circ$ , $\theta_{ov} = 4.66^\circ$ . (c). Cubic TSF, $\theta_{on} = 39.96^\circ$ , $\theta_{ov} = 6.55^\circ$ . (d). Exponential TSF, $\theta_{on} = 41.36^\circ$ , $\theta_{ov} = 15.77^\circ$ . (e). TSF in [41], $\sigma = 1.75$ . (f). Proposed online TSF, $\theta_{on} = 45.79^\circ$ , $\theta_{off} = 163.11^\circ$ .....	139
Fig. 6.12. Experimental results at 1000 r/min and 10 Nm torque reference. (a) Linear TSF, $\theta_{on} = 29.84^\circ$ , $\theta_{ov} = 28.53^\circ$ . (b). Sinusoidal TSF, $\theta_{on} = 29.18^\circ$ , $\theta_{ov} = 28.81^\circ$ . (c). Cubic TSF, $\theta_{on} = 25.86^\circ$ , $\theta_{ov} = 33.91^\circ$ . (d). Exponential TSF, $\theta_{on} = 31.51^\circ$ , $\theta_{ov} = 20.53^\circ$ . (e). TSF in [41], $\sigma = 38.79$ . (f). Proposed online TSF, $\theta_{on} = 36.14^\circ$ , $\theta_{off} = 163.11^\circ$ .....	143
Fig. 6.13. Experimental results at 1500 r/min and 5 Nm torque reference. (a) Linear TSF, $\theta_{on} = 24.24^\circ$ , $\theta_{ov} = 35.27^\circ$ . (b). Sinusoidal TSF, $\theta_{on} = 17.49^\circ$ , $\theta_{ov} = 38.93^\circ$ . (c). Cubic TSF, $\theta_{on} = 14.99^\circ$ , $\theta_{ov} = 3.81^\circ$ . (d). Exponential TSF, $\theta_{on} = 15.07^\circ$ , $\theta_{ov} = 1.95^\circ$ . (e). TSF in [41], $\sigma = 715.24$ . (f). Proposed online TSF, $\theta_{on} = 5.82^\circ$ , $\theta_{off} = 138.89^\circ$ .....	146
Fig. 6.14. Performance comparison at 1000 r/min and 10 Nm torque reference. (a) $i_{ref}$ is generated offline. (b) $i_{ref}$ is generated online. (c). $i_{ref}$ comparison. (d) Total torque comparison.....	148

Fig. 7.1. $dq$ plane of IPMSM. ....	153
Fig. 7.2. Torque-speed characteristic of IPMSM.....	153
Fig. 7.3. Flowchart for the conduction angle optimization. ....	155
Fig. 7.4. Results of conduction angle optimization, when the objective function is $f_1 = -T_{ave}$ . (a). Average torque. (b). RMS current. (c). RMS torque ripple. (d). Torque ripple percentage. ....	157
Fig. 7.5. Dynamic simulation results at 1000 r/min and 100 A current command. ....	158
Fig. 7.6. Results of the cubic TSF optimization, when the objective function is $f_2 = [T_{Rrms},$ $I_{rms}]$ . (a). Average torque. (b). RMS current. (c). RMS torque ripple. (d). Torque ripple percentage. ....	162
Fig. 7.7. Results of the proposed offline TSF optimization, when the objective function is $f_2 = [T_{Rrms}, I_{rms}]$ . (a). Average torque. (b). RMS current. (c). RMS torque ripple. (d). Torque ripple percentage. ....	165
Fig. 7.8. Comparison of the torque-speed characteristics of SRMs. (a). Average torque versus speed. (b). RMS torque ripple versus speed. ....	166
Fig. 7.9. Dynamic simulation results at 1000 r/min and 52.5 Nm torque command. (a). Total torque. (b). Phase torque. (c). Phase current. ....	167

# List of Tables

Table 4.1. Design specifications of SRM-I.....44

Table 4.2. Design specifications of SRM-II .....44

Table 4.3. Rating parameters of the induction dyno. ....45

Table 5.1. Design specifications of the 3-phase 12/8 SRM .....83

# Chapter 1

## Introduction

### 1.1 Background

Clean energy solutions and reduction of CO<sub>2</sub> emissions have drawn increasing attention over the decades. Vehicle electrification, such as electric vehicles (EVs) and hybrid electric vehicles (HEVs), which save on fuel and emit fewer greenhouse gases, are the solutions to sustainable transportation in future [1]–[7]. Interior permanent magnet synchronous machines (IPMSMs) have been widely used in the transportation application thanks to their high operation efficiency and high power density [8]–[11]. However, IPMSMs employ rare earth materials, which have been suffering from unstable supply and fluctuating prices.

Switched reluctance machines (SRMs) are the rare-earth-free type of motors, renowned for their simple structure, low cost, high reliability, large torque density

and satisfactory performance over a wide speed range. They are considered as potential candidates for applications in EVs and HEVs. In [12], a 60 kW SRM was designed with the same outer diameter and axial length as the IPMSM used in the Toyota Prius. The operating efficiency and output performance were tested in [13] and [14]. In [15], a 5-hp, 6/10 SRM was developed for HEVs. The self-starting capability and fault tolerance were investigated. In [16], a double rotor SRM was designed for HEVs, and a scaled prototype motor was constructed and tested for Urban Dynamometer (UDDS) and Highway Fuel Economy Test (HWFET) driving cycles. In [17], a 24/16 SRM was designed for traction applications. The torque-speed characteristic is competitive to the IPMSM employed in the 2010 Prius powertrain.

Except for the traction applications, SRM is also a promising alternative in the residential [18]–[20] and industrial applications [21]–[23]. However, due to its doubly salient structure, SRM inherently shows high torque ripple, which limits its widespread use in these applications. Torque ripple can be detrimental to the lifetime of the rotating components [24], [25]. It can also cause drivetrain vibration and acoustic noise [26]. There are many investigations in the literature to minimize the torque ripple in SRM. Phase current profiling and, particularly torque sharing functions (TSFs), are considered as a more effective solution for torque ripple reduction in SRMs. In a TSF, the expected torque is distributed among the phases and, hence, the total torque equals to the reference torque.

The offline TSF methods can be classified as conventional TSFs and optimization-based TSFs. In the conventional TSF method, specific functions are used to approximate the phase torque waveform. Linear, cubic, sinusoidal/cosine, and exponential functions are commonly used [27]. Based on the torque reference, only the turn-on, turn-off, and overlapping angles are defined to generate the TSF function. Different methods have been proposed in the literature to improve the performance of the conventional TSFs. In [27], the turn-on and overlapping angles are optimized at different operating conditions using Genetic Algorithm (GA). In [28], the conventional TSFs were combined with a fuzzy logic controller to compensate for the torque tracking error. In [29], the cubic TSF was combined with a flux linkage controller to avoid the saturation of the current controller. In [30], cosine TSF is modified to compensate for the negative torque produced by the tail current in the high-speed operation. In [31], the linear TSF was modified to compensate for the torque tracking error in the commutation region. In [32], the expression for the rise and fall portions of the linear TSF is divided into three segments based on the motor characteristics to improve its performance. In [33], a non-unity piecewise quadratic TSF was employed to reduce the torque ripple for a switched reluctance generator. In [34], an analytical TSF was proposed incorporating two quadratic and one linear functions to approximate the torque waveform. A series of B-Spline functions was adopted in [35] to represent the phase current profile. The negative torque production region was also considered in the definition of the TSF. In [36], a nonlinear logical TSF was proposed to improve the

torque profile for torque ripple reduction and efficiency improvement in the motor and inverter. In [37], the design process and control algorithm were combined for the torque ripple reduction of an SRM. A simple initial current profile was defined at first, and then simulation or experiments were carried out. The current profile was fine tuned for the torque ripple reduction using the output torque of SRM from the simulation or experimental results. The varying degrees of freedom (DoFs) for the piecewise conventional TSFs is presented in [38] to minimize the torque ripple at different speed and torque references. It was concluded that high number of DoFs help improve the accuracy of the TSF.

By using specific mathematical functions, conventional TSFs model the optimal shape of the phase torque/current to reduce the torque ripple. These functions simplify the nonlinear problem by parameterizing the torque and current waveforms. However, the precision of the torque waveform approximation is limited because there is no theoretical relationship between these mathematical expressions and motor characteristics. Thus, they have inherent torque and current tracking error.

Unlike the conventional TSF methods, the optimization-based TSF methods do not rely on analytical expressions to represent the phase torque and current waveforms. Instead, the optimal phase current reference is derived by solving an optimization problem, which is more flexible. In [39], the adjacent two-phase currents were used as the optimization objectives, and all phases were energized in the positive torque region. By tuning the weight parameter in the objective function,

a tradeoff was made between the maximum rate of change of flux linkage (RCFL) and the copper loss. In [40], the square of the phase current and its derivative were considered as the secondary objectives in the optimization. In [41], a simplified objective function has been proposed, which uses a single weight parameter to penalize the current of the outgoing phase. In [42], besides the torque ripple and copper loss, radial forces were also taken into consideration in the objective function. More weight parameters were used to establish a tradeoff among the three objectives.

One of the common features of the optimization-based TSF methods is the weight parameters used in the objective function. They need to be tuned for different operating conditions for the given motor. The weight parameters may change the physical meaning of the objective function. For example, in [39], the objective function is defined as the two adjacent phase currents to the  $p^{th}$  power, where  $p$  is the weight parameter. Only when  $p$  equals to 2, the square of the phase current or the copper loss can be minimized. Another limitation of the optimization-based TSFs is that the turn-on and turn-off angles cannot be optimized directly. This is because the objective functions only include the phase current. This might also cause tracking error and restrain the torque-speed capability. For example, it might not be possible to advance the turn-on angle beyond the unaligned position [41]. This means that the rising time of the phase current may be insufficient, reducing the effectiveness of the TSF at high-speed conditions.

The performances of the offline TSFs rely on the SRM model, which is built using the static characteristics of the machine obtained from measurements or finite element analysis (FEA) [43]. The non-negligible error in the experimental characterization procedure [44] and assumptions applied in FEA [45] may affect the accuracy of the SRM model and, thereby, cause torque ripple. The static characteristics may also vary in time in the practical application. Furthermore, one current reference lookup table (LUT) from the offline optimization may only be suitable for a single operating condition. Thus, a large memory space might be required for different operating conditions.

There are many online methods to minimize the torque ripple in SRM [46]–[55]. Direct instantaneous torque control (DITC) [46] is one of the online torque control methods, which control the real-time torque using a hysteresis torque controller. However, magnetic saturation in the core can impact the effectiveness of DITC [49]. Some other online methods have been reported to tune the conduction angles to improve the motor efficiency or reduce the torque ripple for SRMs [47]–[51]. In [49], an adapted commutation strategy combined with DITC was proposed. The firing angles were adjusted online based on a torque error regulator to improve system efficiency. In [50], the commutation region was subdivided into two parts based on the conventional DITC scheme, and the boundary angles were optimized by GA to improve the motor efficiency. In [51], the advanced conduction angle is automatically updated to improve the current tracking performance of an SRM.

The other type of online control techniques for torque ripple reduction is compensation-based methods. In [52] and [53], an iterative learning controller was adopted to compensate for the phase current based on the torque tracking error. This method requires a high sampling frequency. Thus, it is only suitable for the low-speed drive. The existing online TSF methods are also compensation based. In [54] and [55], the absolute values of the rate of change of flux linkage (ARCFL) of the incoming phase and outgoing phase are first calculated. The phase, which has lower ARCFL, is assumed to have zero torque tracking error. However, the torque tracking error may still exist because it can only be indicated that the phase, which owes lower ARCFL, has lower torque tracking error.

## 1.2 Motivation

Although the existing TSF methods have a lot of merits, there are also some drawbacks:

For conventional TSFs:

- 1) The precision of the torque waveform approximation is limited because there is no theoretical relationship between these mathematical expressions and motor characteristics. There are still inherent torque and current tracking error.
- 2) Negative torque is not allowed. The demagnetization current has to decay to zero before the aligned position.

For the existing optimization-based TSFs:

- 3) The weight parameters used in the objective function need to be tuned for different operating conditions for the given motor.
- 4) The weight parameters may change the physical meaning of the objective function.
- 5) The turn-on and turn-off angles cannot be optimized directly.
- 6) Negative torque is not allowed in some of the optimization-based TSFs.

For all the existing TSFs:

- 1) The machine dynamics are not considered or not fully considered. Thus, current tracking error may exist, which causes torque ripple.
- 2) The torque control performance may degrade with the increase of speed.

Motivated by the aforementioned development and challenges of the existing TSF methods, the research has been conducted and accomplished. A comprehensive analysis of the torque ripple reduction methods is presented in this thesis. Two new TSF methods are proposed for torque ripple reduction in SRM drives.

A new offline TSF method is proposed for torque ripple reduction in SRMs. The proposed offline TSF achieves lower current tracking error by establishing a new current reference generation strategy. The phase current reference is first

derived from the torque command using offline calculations and also from the phase current response that is obtained from the dynamic model of the SRM. Then, an optimization problem is formulated to shape the current reference for the objective of minimizing the torque ripple and copper losses, while maintaining the required average output torque at the given operating speed. The dynamic simulation of the SRM model is also utilized in the optimization problem. Compared to the existing conventional and optimization-based TSFs, the proposed TSF exhibits lower current tracking error due to the consideration of the current dynamics. Better torque-speed performance with improved average torque and reduced torque ripple is also obtained, especially during commutation.

A new online TSF method is proposed for torque ripple reduction in SRMs. The proposed TSF takes the current dynamics and induced electromotive force into account by establishing a new online current profile generation technique. First, a primary phase current reference derived from the torque reference is applied to the SRM. Then, the decaying phase current after the turn-off angle is sampled and it is used to update the current reference. A new online optimization strategy is performed to shape the current reference during the operation of the machine. Owing to the proposed current profile generation technique, the optimization process is decoupled to independently minimize the torque ripple by optimizing the turn-on angle and minimizing copper losses by optimizing the turn-off angle. Compared to the conventional TSFs and existing optimization-based TSFs, the

proposed TSF achieves accurate torque control, improved torque-speed capability, reduced torque ripple, and better current tracking performance.

The torque-speed characteristics of the SRM are derived with and without considering the torque quality. The conduction angle control method, conventional TSF method, and the proposed TSF method are investigated and compared in terms of the torque-speed characteristic.

In order to validate the proposed TSF methods, a new experimental setup was designed and built with an off-the-shelf 5.5 kW, 1000 r/min, 3-phase 12/8 SRM. The flux linkage-current-position and torque-current-position characteristics are experimentally-measured. Simulations and experiments under different operating conditions are carried out to verify the proposed offline and online TSF methods.

### 1.3 Contributions

The author contributes to a number of original developments, which are briefly described as follows:

- 1) A comprehensive review on torque ripple reduction methods for switched reluctance machine drives is presented.
- 2) A comprehensive analysis of the machine dynamics and current/torque tracking performance for switched reluctance machines is presented.

- 3) A multi-objective optimization is formed and used to generate the ripple-free torque-speed characteristic of switched reluctance machine for the entire speed range.
- 4) A novel offline torque sharing function for torque ripple reduction in switched reluctance machine is proposed.
- 5) A novel online torque sharing function for torque ripple reduction in switched reluctance machine is proposed.
- 6) A SRM experimental setup is designed and developed.

## 1.4 Outline of the Thesis

This thesis presents advanced torque ripple reduction methods in switched reluctance motor drives.

Chapter 2 presents the fundamentals of switched reluctance motor drives. It starts with the operational principles, including the equivalent circuit and power conversion in SRM. Then, several typical power converters and basic control methods, such as single pulse voltage control, hysteresis current control, and PWM voltage control, are described.

Chapter 3 presents a comprehensive review of torque ripple reduction methods for switched reluctance machine drives. These methods are discussed from three aspects, namely motor geometry improvements, motor drive developments, and control method developments.

Chapter 4 describes the design and implementation of a switched reluctance machine drive setup from the view of device selection, mechanical design and electrical design. Then, the static flux linkage and torque characteristics of the reference SRM are experimentally measured.

Chapter 5 proposes an offline torque sharing function for torque ripple reduction in switched reluctance machines. The drawbacks of the existing conventional and optimization-based TSFs are firstly analyzed in detail. Then the proposed current reference generation strategy is stated. An optimization problem is formulated to shape the current reference for the objective of minimizing the torque ripple and copper losses, while maintaining the required average output torque at the given operating speed. Finally, the performance of the proposed TSF is compared with the conventional TSFs and existing optimization-based TSFs through both simulations and experiments.

Chapter 6 proposes a novel online torque sharing function for torque ripple reduction in switched reluctance machines. The induced voltage and phase current dynamics of SRM are first analyzed. Then the proposed online current reference generation strategy and adaptive turn-on angle adjustment strategy are stated. The optimization process is decoupled to independently minimize the torque ripple by optimizing the turn-on angle and minimizing copper losses by optimizing the turn-off angle. Finally, the performance of the proposed TSF is compared with the conventional TSFs and existing optimization-based TSFs through both simulations and experiments.

Chapter 7 presents the torque-speed characteristics of the SRMs. Firstly, the output characteristic of an interior permanent magnet synchronous machine is introduced for comparison. Then, the torque-speed characteristics of the SRM are derived with and without considering the torque quality. The conduction angle control method, conventional TSF method, and the proposed TSF method are investigated and compared in terms of the torque-speed characteristic.

Chapter 8 concludes the thesis and proposes potential future works.

## **Chapter 2**

# **Fundamentals of Switched Reluctance Machines**

### 2.1 Introduction

Switched reluctance machines are considered as the potential candidate for applications in EVs and HEVs comparing to permanent magnet machines and induction machines. However, their doubly salient structure inherently cause high nonlinearity, high torque ripple, serious vibration and acoustic noise. This chapter briefly presents the fundamentals of switched reluctance machines. The equivalent circuit of SRM, power conversion and torque generation mechanism are first introduced. Then, typical power converters and control methods for SRM are presented.

## 2.2 Electromagnetic Energy Conversion

### 2.2.1 Equivalent Circuit of SRM

Based on the Faraday's law, when a voltage is applied to a phase winding of SRM, the phase voltage equation can be expressed as

$$V = iR + \frac{d\lambda}{dt} \quad (2.1)$$

where  $V$  is the voltage across the phase winding.  $R$  represents the phase resistance.  $i$  and  $\lambda$  are the phase current and flux linkage, respectively.

Due to the doubly salient-pole rotor and stator in SRM, the phase inductance  $L$  is the function of the rotor position. If the magnetic saturation is ignored, the flux linkage  $\lambda$  can be expressed as

$$\lambda = L(\theta)i. \quad (2.2)$$

Thus, the voltage equation (2.1) can be rewritten as

$$V = iR + L(\theta) \frac{\partial i}{\partial t} + \varepsilon \quad (2.3)$$

$$\varepsilon = i \frac{\partial L(\theta)}{\partial \theta} \omega \quad (2.4)$$

where  $\varepsilon$  and  $\omega$  represent the induced EMF and angular speed, respectively.  $\omega$  is derived by

$$\omega = \frac{d\theta}{dt}. \quad (2.5)$$

From (2.3), the equivalent circuit for one phase of SRM can be derived. It is shown in Fig. 2.1.

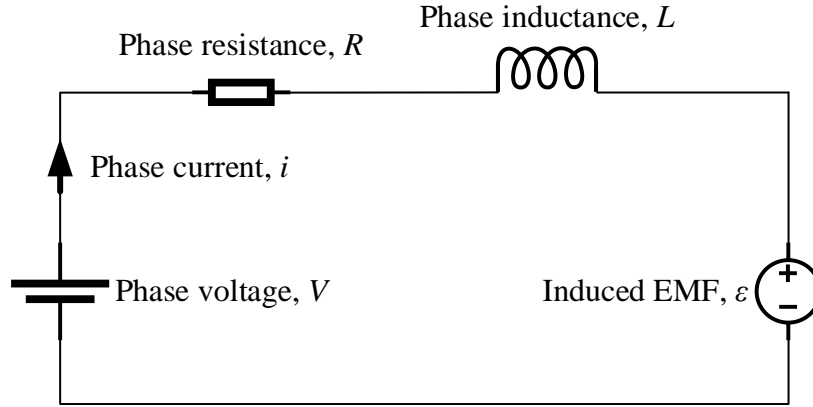


Fig. 2.1. The equivalent circuit for one phase of SRM.

### 2.2.2 Power Conversion and Torque Generation Mechanism

The instantaneous input power in one SRM phase,  $P_{Ph\_in}$  can be obtained by the product of phase voltage and current, and it is defined as

$$P_{Ph\_in} = Vi = i^2R + i \frac{d\lambda}{dt} = i^2R + iL(\theta) \frac{di}{dt} + i^2 \frac{dL(\theta)}{d\theta} \omega. \quad (2.6)$$

The equation (2.6) can also be rearranged as

$$\begin{aligned}
 P_{Ph\_in} &= i^2 R + \frac{d}{dt} \left( \frac{1}{2} i^2 L(\theta) \right) + \frac{1}{2} i^2 \frac{dL(\theta)}{d\theta} \omega \\
 &= i^2 R + \frac{dW_f}{dt} + \frac{dW_m}{dt}
 \end{aligned} \tag{2.7}$$

where  $W_f$  and  $W_m$  represent the magnetic energy and mechanical energy.

It can be observed from (2.7) that the input power  $P_{Ph\_in}$  is dissipated by the resistance as copper losses, stored in the magnetic field  $W_f$ , and converted to the mechanical power  $W_m$ .

The mechanical power is also the product of the instantaneous torque  $T$  and speed  $\omega$ , expressed as in (2.8). By combining (2.7) and (2.8), the phase torque expression can be derived as in (2.9).

$$W_m = T\omega \tag{2.8}$$

$$T = \frac{1}{2} i^2 \frac{dL(\theta)}{d\theta} \tag{2.9}$$

It is worth noting that the equation (2.9) is the phase torque expression in the linear region, where the magnetic saturation effect is ignored.

## 2.3 Power Converters for Switched Reluctance Machines

Due to the special operating principle of the SRM, the power converter plays an important role in SRM drives. Power converters greatly affect the performance and cost of the SRM drives [56]. Many efforts were made to improve the performance and reduce the cost of the power converters in SRM drives. In [57], the power converter topologies for SRM were classified by the number of switch components. For  $m$ -phase SRMs, the topologies in the literature were mainly divided into four categories: (i) converters with  $m$  switches and  $m$  diodes; (ii) converters with  $m+1$  switches and  $m-1$  diodes; (iii) converters with  $m$  switches and  $2m$  diodes; (iv) converters with  $1.5m$  switches and  $1.5m$  diodes; In [58] and [59], the power converter topologies for SRM were classified from the aspect of energy flow.

### 2.3.1 Asymmetric Half-bridge Converter

The asymmetric half-bridge converter is one of the most commonly used converters, shown in Fig. 2.2 for 3-phase SRMs. Comparing to other topologies, it requires a minimum number of passive components. Each phase can independently operate in magnetization, freewheeling, and demagnetization modes, which enables great

flexibility in control. However, it needs two switches and two diodes per phase, thereby increasing the cost of the SRM drive.

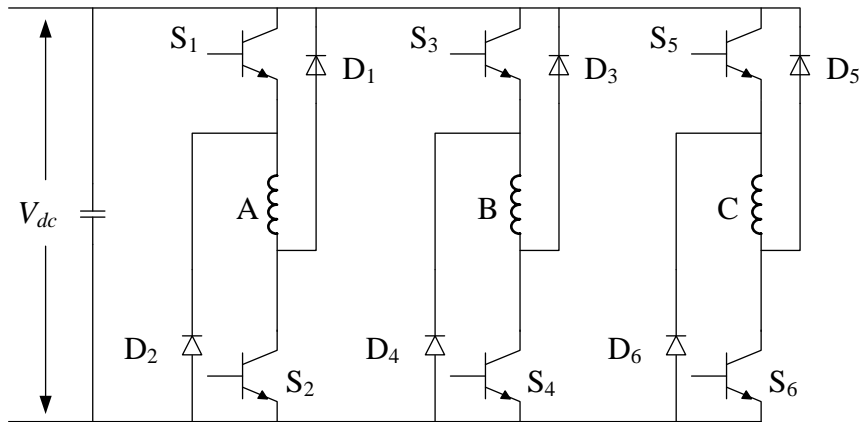


Fig. 2.2. Asymmetric half-bridge converter for 3-phase SRMs.

There are few manufacturers of semiconductors providing the asymmetric half-bridge switch module. Discrete components are usually used to build the asymmetric half-bridge converter. Infineon provided an asymmetric half-bridge IGBT module F4-400R12ME4\_B29 in 2013 and stopped production a few years later. The asymmetric half-bridge converter can also be realized by the standard industrial switch modules [58]. Fig. 2.3 shows the asymmetric half-bridge converter realized by H-bridge switch modules and three-phase full bridge switch modules. However, only half of the switches and diodes are useless. This causes a large size of the drive circuit and a low utilization rate of the components.

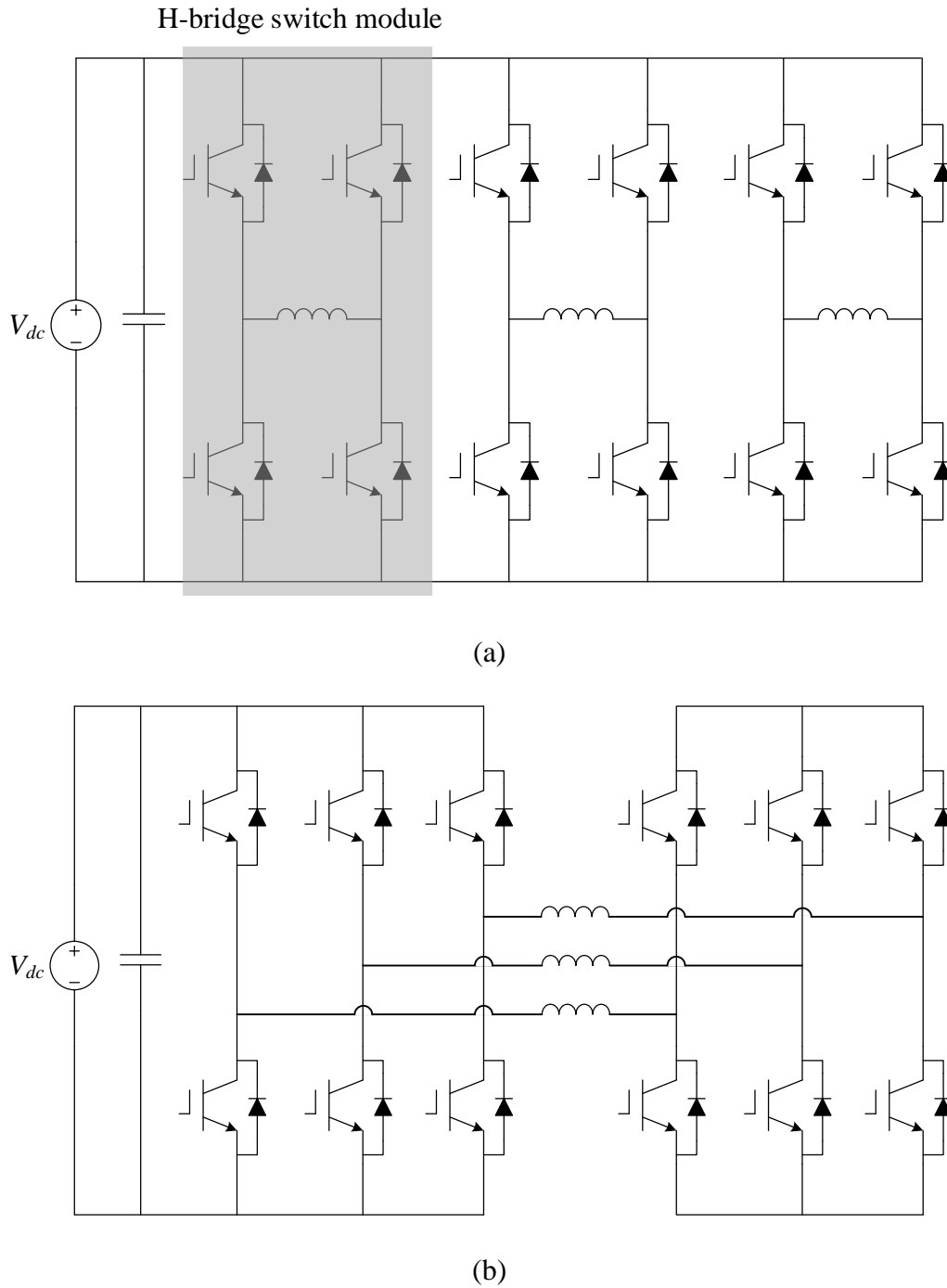


Fig. 2.3. Three-phase asymmetric half-bridge converter constructed by standard industrial switch modules. (a). H-bridge. (b). 3-phase full bridge modules.

### 2.3.2 Dissipative Converter

Fig. 2.4 shows a typical three-phase dissipative converter for SRM. For  $m$ -phase SRM, it only requires  $m$  switch components and  $m$  diodes. When the switch being in series with the phase winding is turned off, the energy stored in the inductance is dissipated by the resistor.

It can be observed from the operating modes that the efficiency of this kind of converters is low compared to other converters. However, this kind of converters is suitable for low-power applications, and the cost is also low due to the minimum number of switches and diodes [59], [60].

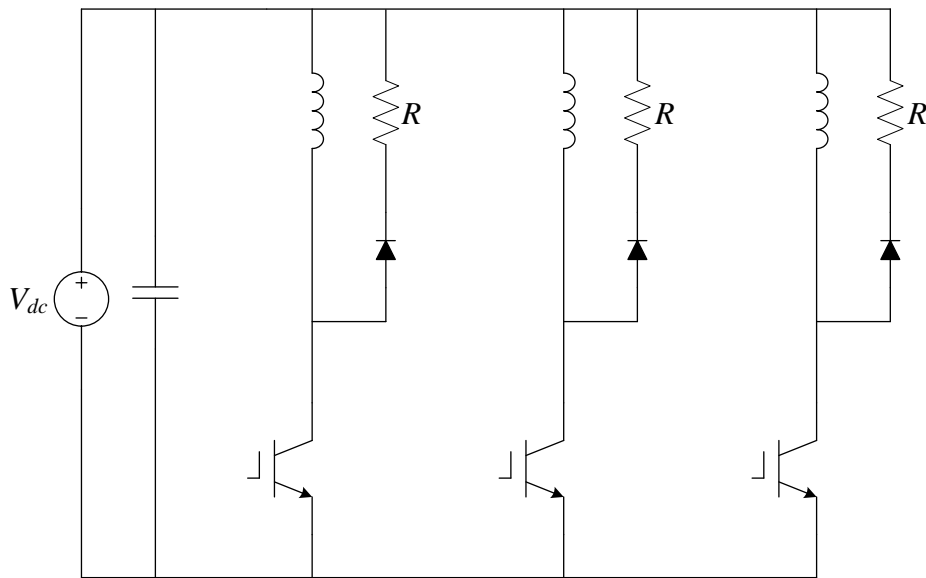


Fig. 2.4. Three-phase dissipative converter.

### 2.3.3 Energy Recovery Converter

Unlike the dissipative converters that dissipate the energy stored in the phase winding, the energy recovery converters transfer the freewheeling energy to a capacitor or inductor. There are two kinds, capacitive energy recovery converters and magnetic energy recovery converters.

Fig. 2.5 shows a typical three-phase C-dump converter for SRM. When the switch being in series with the phase winding is turned off, the energy stored in the inductance is transferred into a capacitor. The elevated voltage on this capacitor increases the phase voltage, which enables fast magnetization and demagnetization modes. However, a higher voltage rating of the components is required.

The magnetic energy recovery converter usually has auxiliary windings. Fig. 2.6 shows a typical three-phase bifilar converter for SRM. When the switch being in series with the primary phase winding is turned off, the energy stored in the primary phase winding is transferred into the secondary phase winding by the freewheeling diode. This allows a high rate of change of current. However, this converter requires secondary windings, thereby, increasing the manufacturing cost.

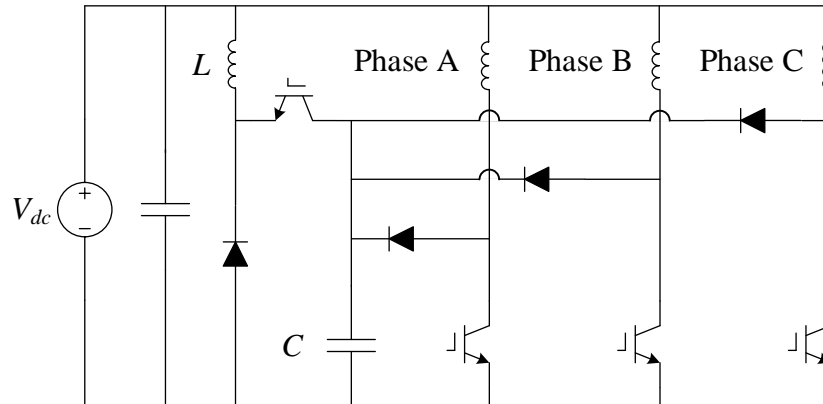


Fig. 2.5. Three-phase C-dump converter.

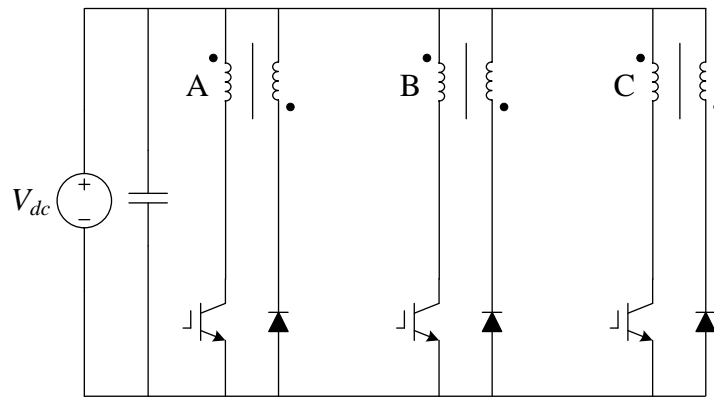


Fig. 2.6. Three-phase bifilar converter.

## 2.4 Basic Control Methods for Switched Reluctance Machine

Single-pulse voltage control (SPV), hysteresis current control (HCC), and pulse width modulation (PWM) voltage control are the three basic control methods of

SRM, which are very simple to implement and widely used in industrial applications.

### 2.4.1 Single-pulse Voltage Control

Single-pulse voltage control is the most basic control method for SRM. It is also called angle position control because of its dependence on the rotor position. By adjusting the turn-on angle,  $\theta_{on}$  and turn-off angle,  $\theta_{off}$ , the phase current profiles can be changed. This method is always used for high-speed applications. Fig. 2.7 shows the phase current of SRM with different turn-on and turn-off angles.

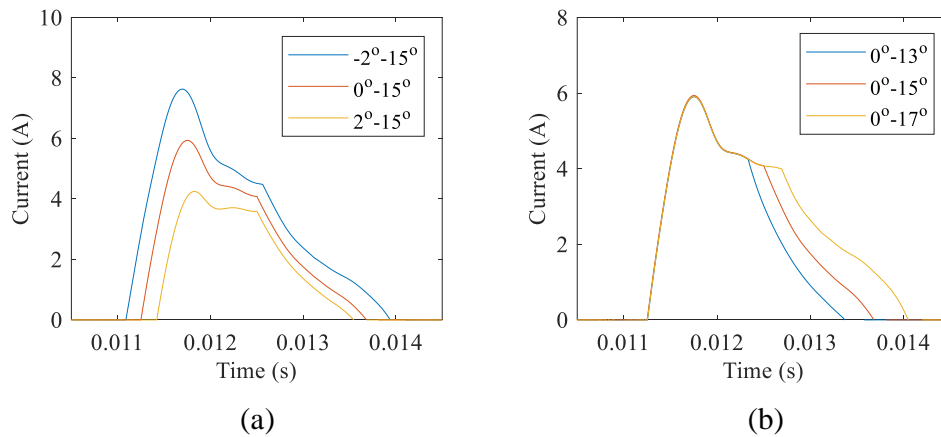


Fig. 2.7. Phase current profiles with SPV control under different  $\theta_{on}$  and  $\theta_{off}$ .

### 2.4.2 Hysteresis Current Control

Hysteresis current control is suitable for low-speed applications when the phase current of SRM is expected to maintain the constant value. Fig. 2.8 shows the schematic diagram of the hysteresis current control technique. When the SRM is operating at low speed, the induced EMF is low. The hysteresis current control method is usually implemented to (i) keep the phase current at constant value; (ii) prevent the phase current exceeding the limit. For the given current reference  $i_{ref}$  and hysteresis bandwidth  $\beta$ , the lower and upper current bounds can be calculated, as expressed in (2.10) and (2.11). Fig. 2.9 shows the phase current waveforms with different current references.

$$i_{up} = i_{ref} + \frac{\beta}{2} \quad (2.10)$$

$$i_{down} = i_{ref} - \frac{\beta}{2} \quad (2.11)$$

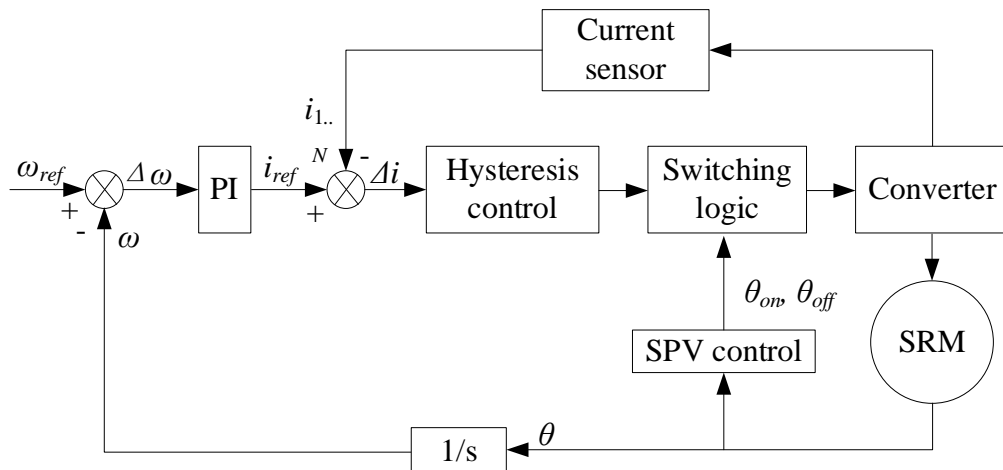


Fig. 2.8. Schematic diagram of the hysteresis current control method.

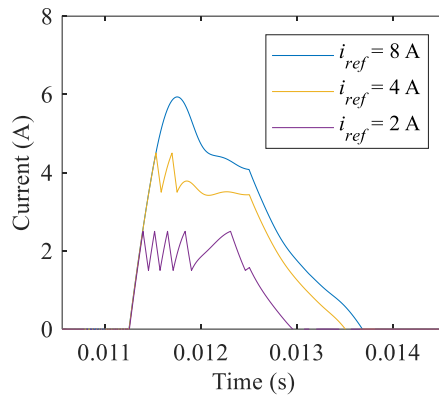


Fig. 2.9. Phase current waveforms with HCC under different current references.

### 2.4.3 PWM Voltage Control

PWM voltage control is commonly used at low-speed and medium-speed operations. By adjusting the duty ratio, the voltage applied on each phase is changed, and then the phase current is changed. The block diagram of the PWM voltage control technique is shown in Fig. 2.10, and the phase current waveforms with different duty ratio is shown in Fig. 2.11.

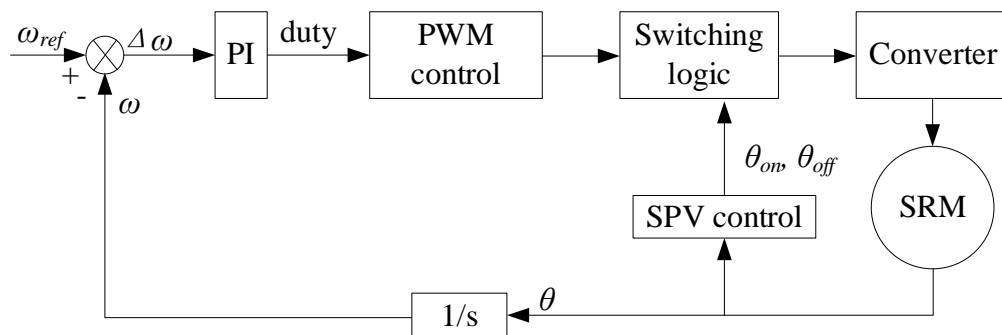


Fig. 2.10. Schematic diagram of the PWM voltage control method.

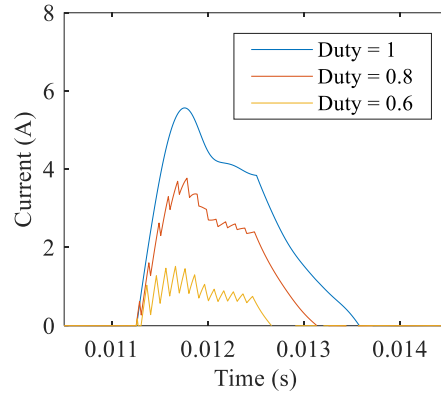


Fig. 2.11. Phase current waveforms with PWM control under different duty ratios.

## **Chapter 3**

# **Torque Ripple Reduction Methods for Switched Reluctance Motor Drives**

### **3.1 Introduction**

Switched reluctance machines are gaining attentions in industry and research community, owing to their simple structure, low cost and high reliability. However, SRMs suffer from high torque ripple compared to other ac machines, which limit their applications. Many efforts have been made in the literature to reduce the torque ripple and improve the torque control performance for SRM drives. Fig. 3.1 shows the classification of the torque ripple reduction methods for SRM drives. These methods are divided into three aspects, namely motor geometry

improvements, motor drive developments, and control method developments, which are discussed and analyzed in this chapter.

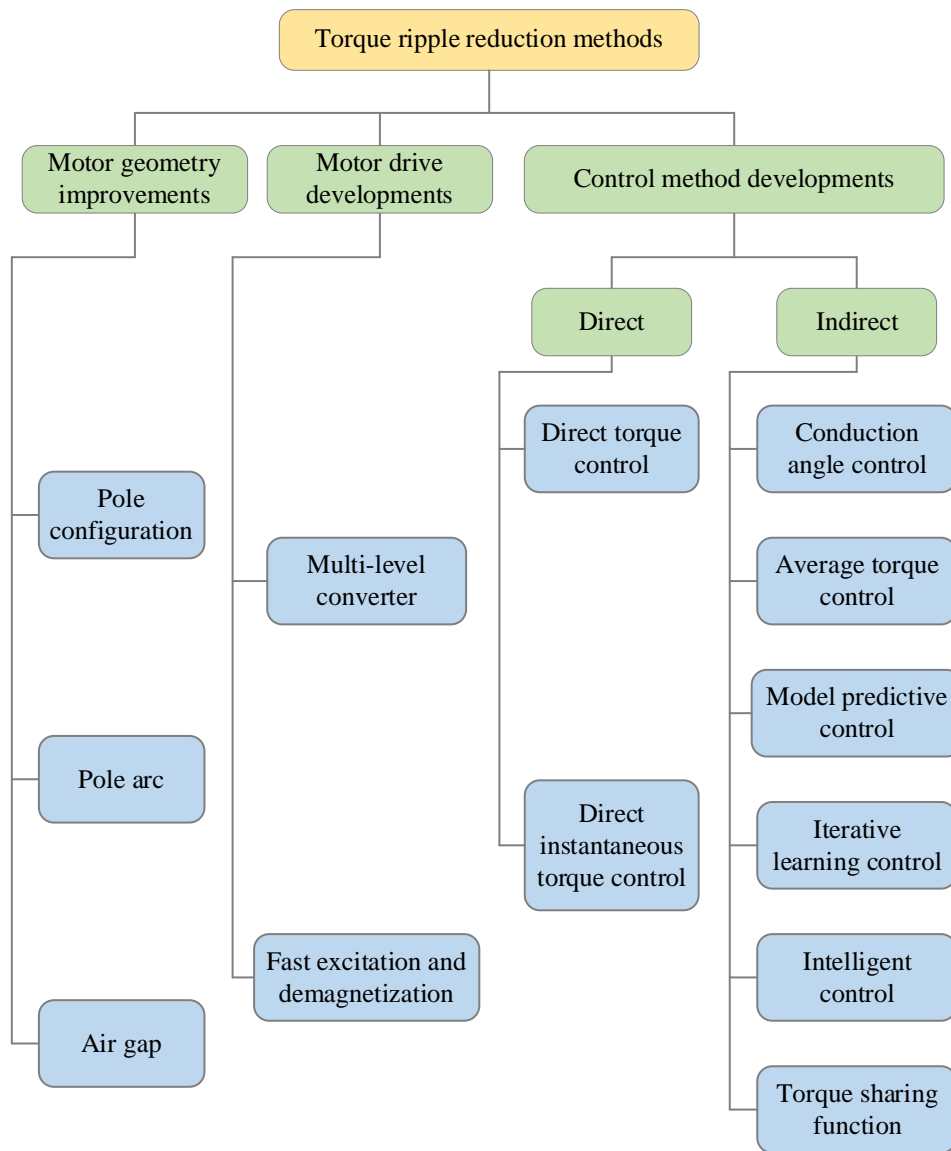


Fig. 3.1. Classification of the torque ripple reduction methods for SRM drives.

## 3.2 Motor Geometry Improvements

The doubly salient structure is one of the main reasons why a SRM has high torque ripple. Torque ripple can be reduced by optimizing the geometrical parameters. The combinations of the stator and rotor poles have an influence on the torque ripple and average output torque. In [61], a new pole-design formula has been proposed, and a group of SRMs that own a higher number of rotor poles than stator poles have been investigated. Simulations and experiments results on a 6/10 SRM shown that this new pole configuration can produce lower torque ripple compared with a conventional 6/4 SRM. In [62], 6/4, 6/8, 6/10 in-wheel SRMs are evaluated. It is concluded that the torque ripple reduces with the increase of the number of rotor poles. The same conclusion can be found in [63] for the comparison of 12/8 and 12/16 SRMs. In [64], two segmented-rotor SRMs with 16/10 and 16/14 pole configurations have been investigated. It has been shown that the 16/14 SRM provides larger torque and lower torque ripple at low-speed operation, and vice versa.

In [65], a neural network is trained to minimize the torque ripple by optimizing the tooth pitch and width. In [66], the stator and rotor pole arcs of a 8/6 SRM have been optimized to achieve higher average torque and lower torque ripple. In [67], the influence of the pole arc/pole pitch ratio of the stator and rotor has been investigated. It has been concluded that the stator pole arc has a larger influence on the average torque compared with the rotor pole arc. Novel stator pole face and

rotor pole shoe are developed in [68], which generates a non-uniform air-gap. Torque ripple is reduced by optimizing the air-gap profile and pole shoe. In [69], the influence of the locations of the moulding clinches has been investigated. It has been concluded that lower torque ripple can be obtained if the locations of the moulding clinches are closer to the rotor pole head.

### 3.3 Motor Drive Developments

Many converter topologies have been proposed to improve the torque control performance of SRMs. The common feature of these topologies is the accelerated excitation/demagnetization process of the phase windings. In [70], a highly integrated modular converter for SRMs has been proposed for range-extended electric vehicles. The topology is shown in Fig. 3.2. fast excitation and demagnetization are realized owing to the front-end circuit, and better torque control performance is obtained. Similar strategies appear in [71]–[76]. Compared to the conventional asymmetric half-bridge converter, the multi-level converters exhibit the advantages, such as lower current ripple and more voltage level with lower switching frequency. In [77], a 7-level neutral point clamped (NPC) converter has been proposed. It has been shown that the torque ripple caused by switching harmonics is much reduced. In [78] and [79], the direct instantaneous torque control (DITC) has been applied to the 4-level converter and 5-level converter, respectively. In [80], the DITC method has been applied to a 3-level

modular converter. It can be concluded from [78]–[80] that lower torque ripple can be achieved due to the shorter demagnetization time.

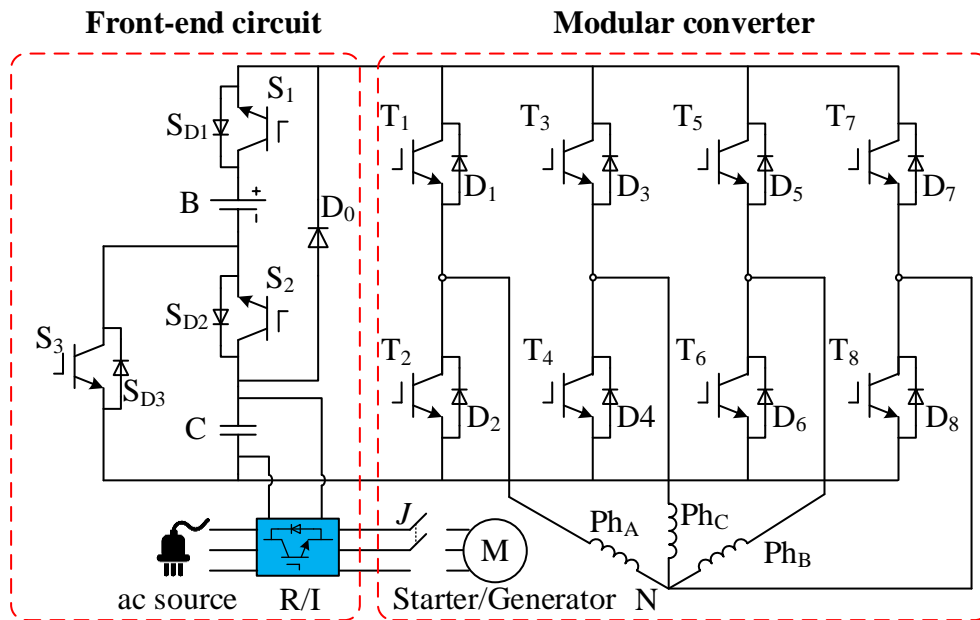


Fig. 3.2. An integrated modular converter for 3-phase SRM [70].

### 3.4 Control Methods Developments

The motor geometry and drive improvement methods are not suitable for the SRM drive already manufactured. Comparing to those methods, it is more straightforward and cost-effective to reduce the torque ripple from the control aspect. The torque control can be direct or indirect. The former one includes direct torque control (DTC) and DITC methods. The later one can be further classified

into conduction angle control, average torque control, model predictive control, iterative learning control, intelligent control, and torque sharing function methods.

### 3.4.1 Direct Torque Control

The direct torque control methods have been well established and commonly used for ac machines. Similar techniques are employed to minimize the torque ripple for SRMs. Fig. 3.3 shows the block diagram of DTC or direct torque and flux control (DTFC) method for SRM. There is no current control loop. The switching states are generated by a voltage vector control, which responds to the regulation of the flux linkage and torque.

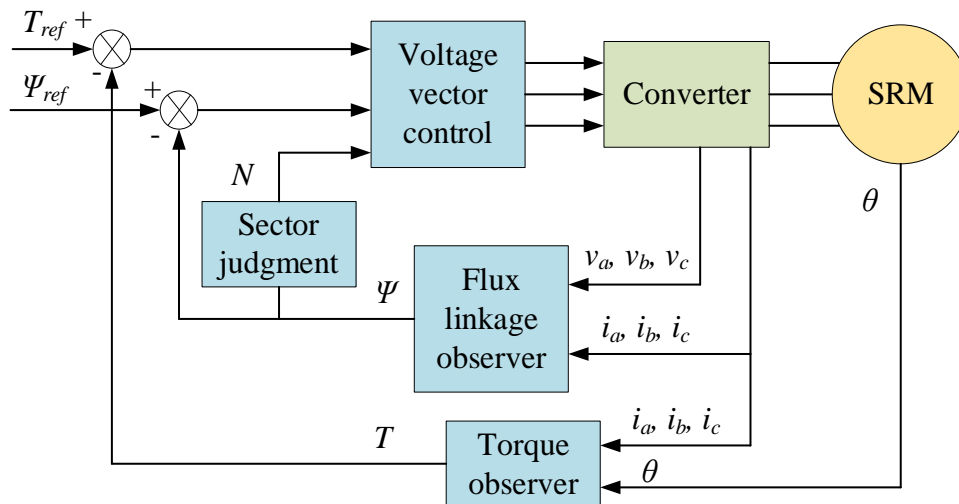


Fig. 3.3. Block diagram of DTC method for 3-phase SRM [81], [82].

In [83], an improved DTC has been proposed to reduce the torque ripple and increase the torque-ampere ratio. A more flexible voltage vector selection strategy is developed. In [84], a new switching sequence has been applied to the DTC method. It is shown that the current ripple and torque ripple are simultaneously minimized.

### 3.4.2 Direct Instantaneous Torque Control

Comparing to the DTC methods, the direct instantaneous torque control (DITC) methods show a simpler structure. The block diagram of the DITC method is shown in Fig. 3.4. Like the DTC method, there is also no current controller. The switching states are generated by the hysteresis torque controller.

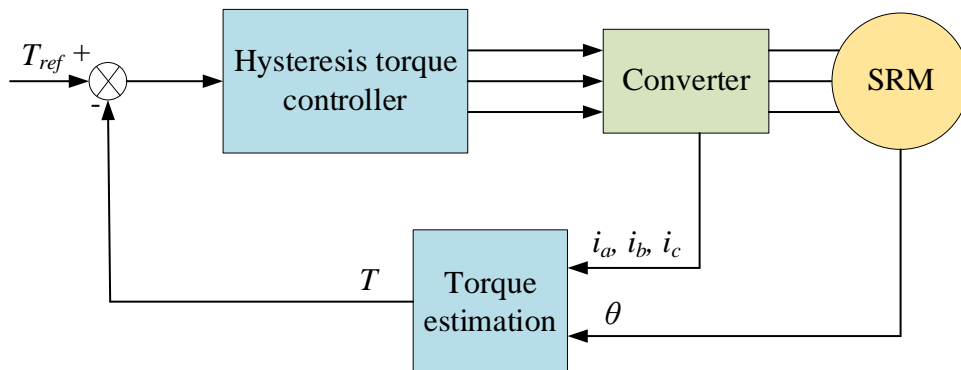


Fig. 3.4. Block diagram of the DITC method [85].

In [86], the optimum switching angles from TSF methods are used to improve the DITC method. The results show a wider torque-speed performance. In

[87], the performance of the conventional DITC method is improved by adding a proportional integral (PI) controller before the hysteresis torque regulator. In [88], a novel PWM-DITC method has been proposed. The hysteresis controller is replaced by a PWM controller.

### 3.4.3 Conduction Angle Control

The turn-on and turn-off angles are important control parameters. In [17], the SRM is characterized in terms of average torque, normalized torque ripple and copper loss over the entire speed range based on the optimized conduction angle control. The turn-on and turn-off angles are usually optimized to improve the performance of the SRMs, including the drive efficiency improvement [90], torque per ampere improvement [91], [92], and torque ripple reduction [93]–[95]. It is a common practice to combine the conduction angle optimization with the other advanced control methods for performance improvements.

### 3.4.4 Average Torque Control

Fig. 3.5 shows the block diagram for the average torque control method. The torque reference is generated by the speed regulator, and it is seen as the average torque over one conduction region. Therefore, the current reference keeps constant over one conduction period [97]. In [98], an online average torque estimation strategy was added to the average torque control method to improve the dynamic

performance, and the conduction angles were optimized to improve the operating efficiency and reduce the torque ripple.

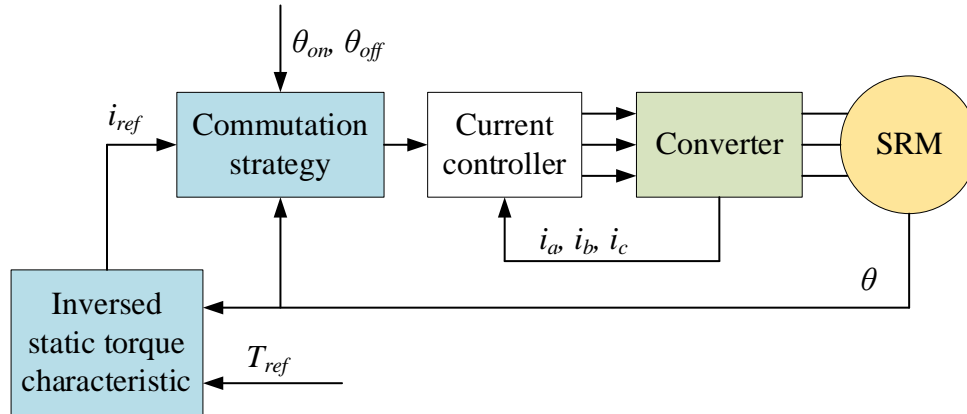


Fig. 3.5. Block diagram of average torque control method [96], [97].

### 3.4.5 Model Predictive Control

Model predictive control (MPC) is a powerful method for nonlinear and multivariable applications [99], [100]. It directly generates switching signals and avoids complex switching rules. Fig. 3.6 shows the block diagram of the model predictive control method. In [101], a novel switching table has been proposed to reduce the computational burden for an improved finite-state predictive torque control. The torque ripple, copper losses and switching frequency are optimized together. In [102], a predictive current control strategy has been proposed. The duty ratio is predicted based on the phase inductance profile. The results have shown improved current tracking performance and reduced torque ripple. The predictive

current controller is compared with the conventional hysteresis current controller in [103]. In [104], the turn-off angle in MPC is optimized to reduce the negative torque and torque ripple.

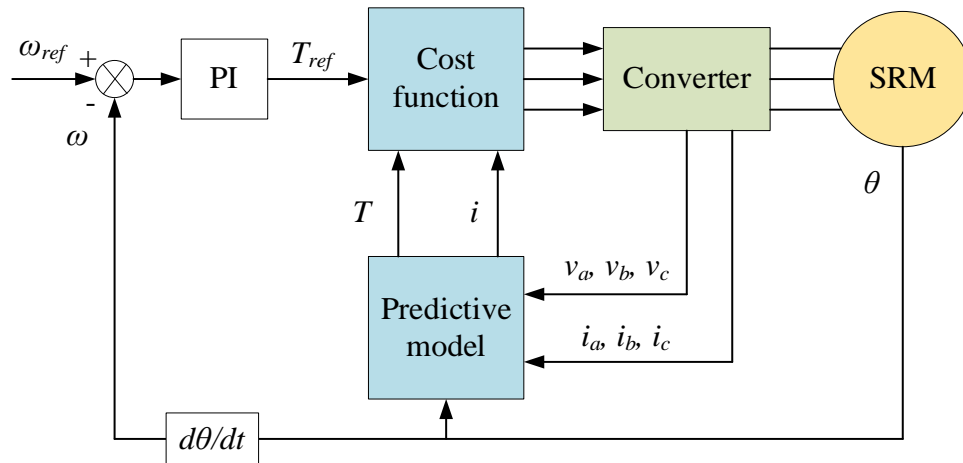


Fig. 3.6. Block diagram of model predictive control [99].

### 3.4.6 Intelligent Control

The intelligent control is a promising method, which uses artificial intelligence techniques like fuzzy logic, neural networks, and genetic algorithms to solve the problem. It can be used to reduce the torque ripple of SRMs. In [105], an adaptive fuzzy system has been used to learn the phase current profiles that reduce torque ripple of a four-phase SRM. The rotor position, torque command and measured torque are employed as inputs of the fuzzy system, and the output is the phase current reference. In [106], an adaptive fuzzy logic controller has been proposed for the torque ripple reduction in SRMs. The block diagram is shown in Fig. 3.7. The

phase current reference is generated based on the torque error and rotor position. This method does not require the characteristics of the SRM, and it is robust to position error. In [107], a self-tuning neuro-fuzzy compensator has been proposed to shape the phase current for torque ripple reduction. The current reference generated by a speed PI controller is compensated by the output of the fuzzy logic controller. In [108], a new adaptive fuzzy control method with segmented harmonic currents injection has been proposed for torque ripple reduction. The block diagram is shown in Fig. 3.8. Three fuzzy logic controllers are employed.  $i_{ref}$  fuzzy controller generates current reference based on the speed error.  $A_{ni}$  fuzzy controller provides a harmonic coefficient based on the torque error.  $\alpha$  fuzzy controller generates an adjustment factor based on the operating speed.

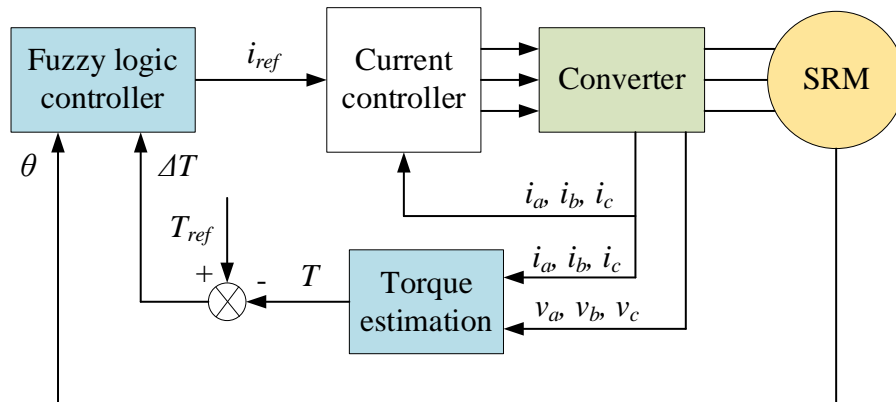


Fig. 3.7. Block diagram of the fuzzy logic control method [106].

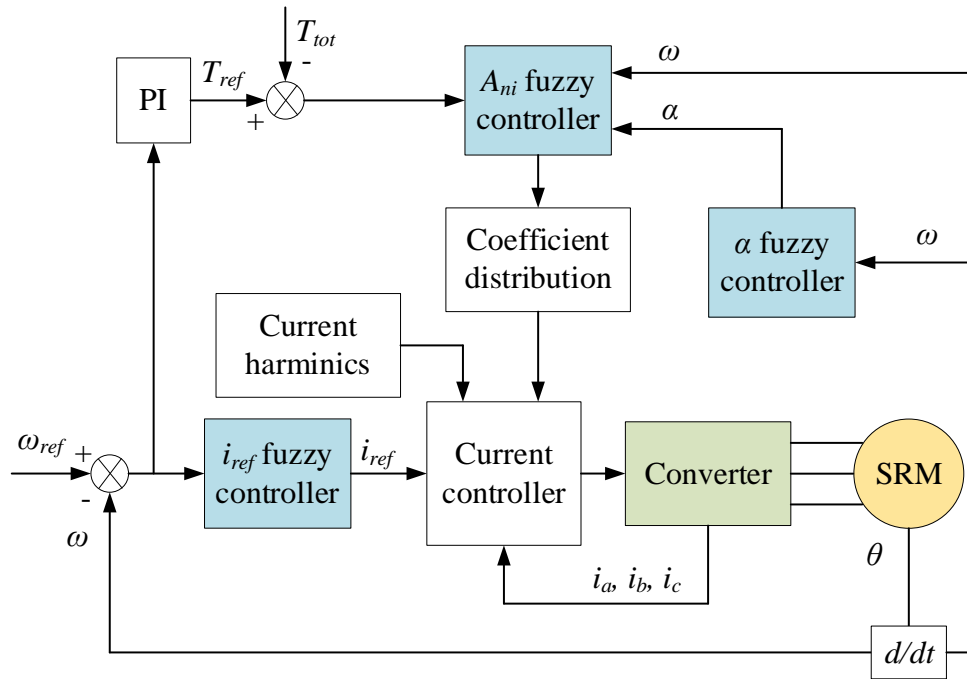


Fig. 3.8. Block diagram of the fuzzy control method in [108].

In [109], a cerebellar model articulation controller neural network has been proposed to reduce the torque ripple of SRMs. This method improves the conventional least-mean-square algorithm and generates effective current references with rapid learning convergence.

### 3.4.7 Iterative Learning Control

In [52], [53], [110], iterative learning control (ILC) methods have been used for torque ripple reduction. Fig. 3.9 shows the block diagram of the ILC-based current controller. The basic mechanism of this kind of methods is to store the control input and output error in each cycle, and then update the input value based on a learning

law. This method requires a high sampling frequency. Thus, it is only suitable for low-speed drives.

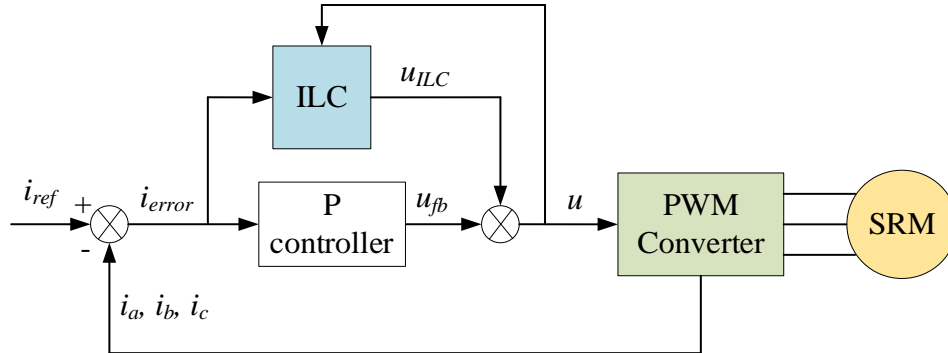


Fig. 3.9. Block diagram of an ILC-based current controller [53].

### 3.4.8 Torque Sharing Function

Torque sharing function method is considered as an effective solution for torque ripple reduction in SRMs. There are offline TSF and online TSF methods. The offline TSFs can be further divided into conventional TSF and optimization-based TSFs. The conventional TSFs use specific functions to approximate the phase torque waveform, and the optimization-based TSFs derive current reference by solving an optimization problem. The online TSF methods are compensation based. The current reference is modified based on the torque error. All the TSF methods have already been discussed in Chapter 1. Taking a wide view of the TSF methods development, the machine dynamics are gradually being recognized and valued.

## 3.5 Conclusion

Switched reluctance machines are gaining attentions in industry and research community, owing to their simple structure, low cost and high reliability. However, SRMs suffer from high torque ripple compared to other ac machines, which limit their applications. In this chapter, the researches in the literature are divided into motor geometry improvements, motor drive developments, and control method developments. A comprehensive review of torque ripple reduction methods for switched reluctance machine drives is presented and summarized.

## **Chapter 4**

# **Design and Implementation of a Switched Reluctance Motor Drive Setup**

### **4.1 Introduction**

In order to experimentally validate the torque ripple reduction methods proposed in this thesis, a SRM experimental setup is designed and built. This chapter presents the design procedure from the view of device selection, mechanical design and electrical design. Then, the static flux linkage and torque characteristics of the reference SRM are experimentally measured. The dynamic model of the SRM used in this thesis is built using these measured characteristics.

## 4.2 Device Selection

The schematic diagram of the experimental setup is shown in Fig. 4.1. The reference SRM is coupled to a dynamometer (dyno), and a torque transducer is connected between them. The dc-link is not shared. The SRM is working in motoring mode, and the dyno is working in generating mode. The generated power is dissipated by a programmable load.

The setup is designed for two off-the-shelf 3-phase 12/8 SRMs. The detailed geometries are unknown, but the design specifications of these two SRMs are shown in Table 4.1 and Table 4.2, respectively.

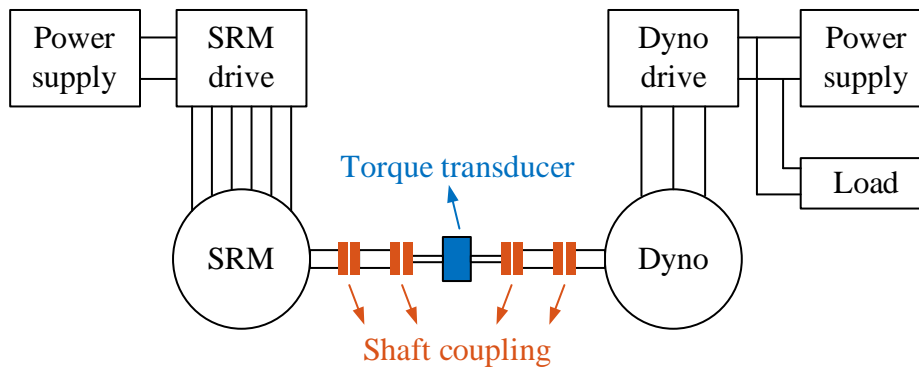


Fig. 4.1. Schematic diagram of the experimental setup.

Table 4.1. Design specifications of SRM-I

Variable	Value	Unit
Outer diameter	274	mm
Axial length	230	mm
Rated power	5.5	kW
Rated speed	1000	r/min
Rated torque	52.53	Nm
Rated current	81.7	A
DC-link voltage	72	V
Maximum speed	2500	r/min
Maximum power	11	kW

Table 4.2. Design specifications of SRM-II

Variable	Value	Unit
Outer diameter	158	mm
Axial length	178	mm
Rated power	5.5	kW
Rated speed	5000	r/min
Rated torque	10.505	Nm
Rated current	81.7	A
DC-link voltage	72	V
Maximum speed	10000	r/min
Maximum power	11	kW

#### 4.2.1 Dynamometer Drive

It can be observed from Table 4.1 and Table 4.2 that both SRM-I and SRM-II are rated at 5.5 kW. However, these two SRMs are designed for different operating conditions. The SRM-I is a low-speed high-torque motor, while the SRM-II is a high-speed low-torque motor.

In order to experimentally test both SRMs in one setup, a trade-off is made. An induction machine (Model GRA0152DS-01) provided by Techtop Canada is selected. The rating parameter is shown in Table 4.3. With this dyno, the rated performance of the SRM-II (5000 r/min, 10.505 Nm) and more than half of the rated performance (1000 r/min, 26.265 Nm) can be tested. A YASKAWA drive (CIMR-AU2A0056FAA) is selected to control the induction machine.

Table 4.3. Rating parameters of the induction dyno.

Variable	Value	Unit
Rated power	15	HP
Rated speed	3530	r/min
Rated torque	30	Nm
Rated current	33	A
Rated voltage	230/460	V/60 Hz
Maximum speed	7060	r/min

#### 4.2.2 Torque Transducer

A torque transducer is used to measure the output torque of the SRM. The measurement frequency of the torque transducer on the market varies from 60 Hz to 6 kHz, and the cost rises as the measurement frequency increases. Nevertheless it is still limited to observe the torque waveform in one electrical cycle of the SRM, especially at high-speed operation.

Based on the rating parameters of SRM-I and SRM-II, a torque transducer NCTE series 3000 is selected for the average torque measurement in this setup. It can measure up to 50 Nm torque, which is closed to the rated torque of the SRM-I. The maximum operating speed is 10000 r/min, which is the maximum speed of the SRM-II. The measurement frequency is 2.5 kHz.

#### 4.2.3 Shaft Couplings

Shaft couplings are not only used to transmit the torque/power between the SRM and dyno, but also used to absorb the misalignment between two rotating shafts. They can be chosen after the dyno and torque transducer are determined. Several parameters need to be considered when selecting the shaft coupling, such as maximum transmitted torque, maximum operating speed, maximum angular and parallel misalignment. For example, the maximum allowable torque and operating speed of the couplings need to be higher than those of the SRMs. The jaw type

couplings are selected for the setup since they can absorb the possible vibrations from the SRM and accommodate the misalignment.

### 4.3 Mechanical and Electrical Design

Each part of the setup is modelled and then assembly together in SolidWorks. The 3D models of SRM-I and SRM-II are shown in Fig. 4.2. Three faceplates are designed for the SRMs and induction machine dyno, as shown in Fig. 4.3. The bottom edges of the SRM faceplates, shown in Fig. 4.3(a) and (b), are designed to rest on the T-slot table. The faceplates are mounted to an angle bracket, as shown in Fig. 4.3 (d). Since two SRMs are driven by one dyno, the center height of these two faceplates are the same. The induction machine dyno has a standard NEMA frame 215T. The faceplate for the induction machine acts as a base, and it is fixed on the T-slot table.

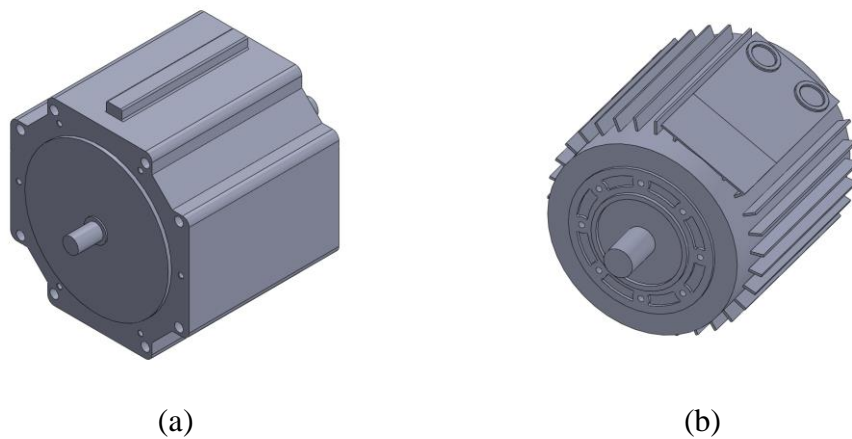


Fig. 4.2. 3D model of SRMs. (a). SRM-I. (b). SRM-II.

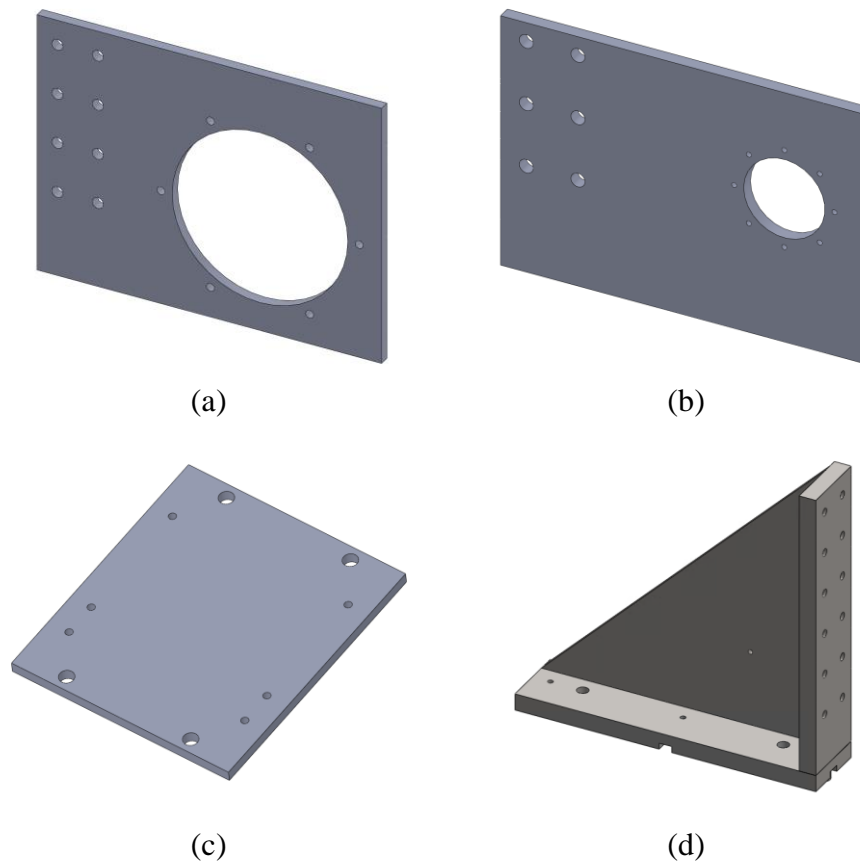


Fig. 4.3. Faceplates for SRMs. (a). For SRM-I. (b). For SRM-II. (c). For dyno. (d). Angle bracket.

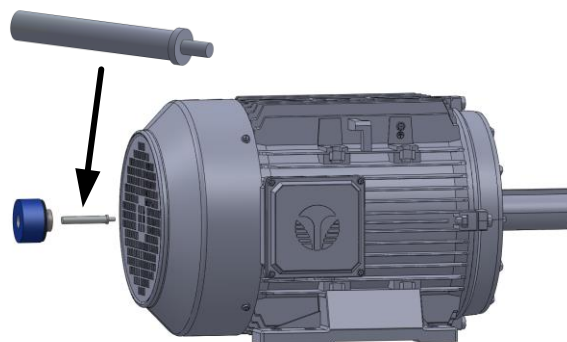


Fig. 4.4. Stepped shaft.

The selected induction machine dyno does not have an encoder. In order to run the dyno with closed-loop speed control. A stepped shaft is designed to fix the encoder to the machine, as shown in Fig. 4.4. Fig. 4.5 shows the 3D model of the torque sensor and its clamping holder.

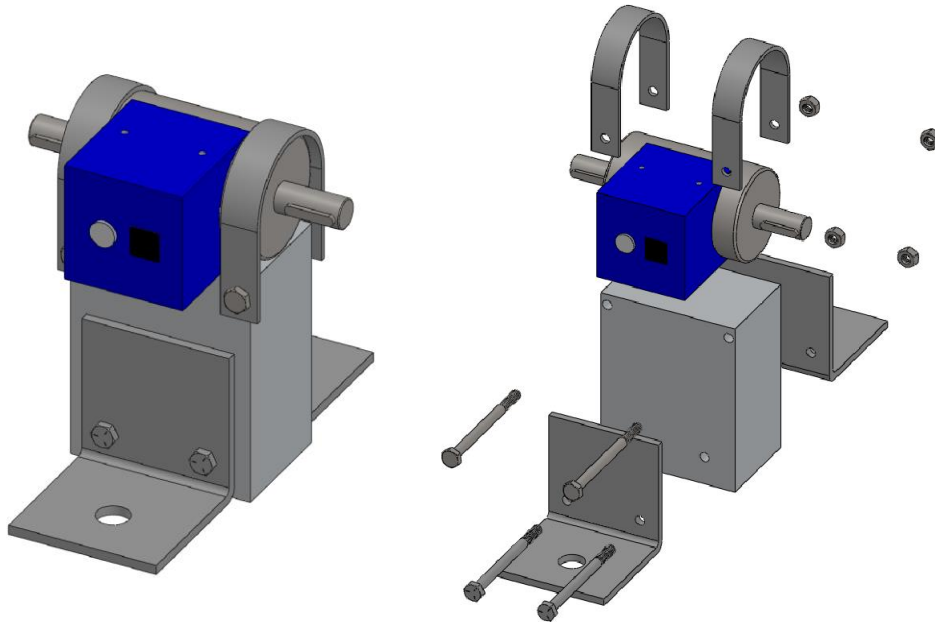


Fig. 4.5. 3D model of the torque sensor and its clamping holder.

The above parts are assembled together in SolidWorks. The overview of the final designed setup is shown in Fig. 4.6. It can be observed that the setup only uses half of the T-slot table. The total length and width of the setup are less than 1219 mm and 900 mm, respectively. Fig. 4.7 shows the picture of the final experimental setup.

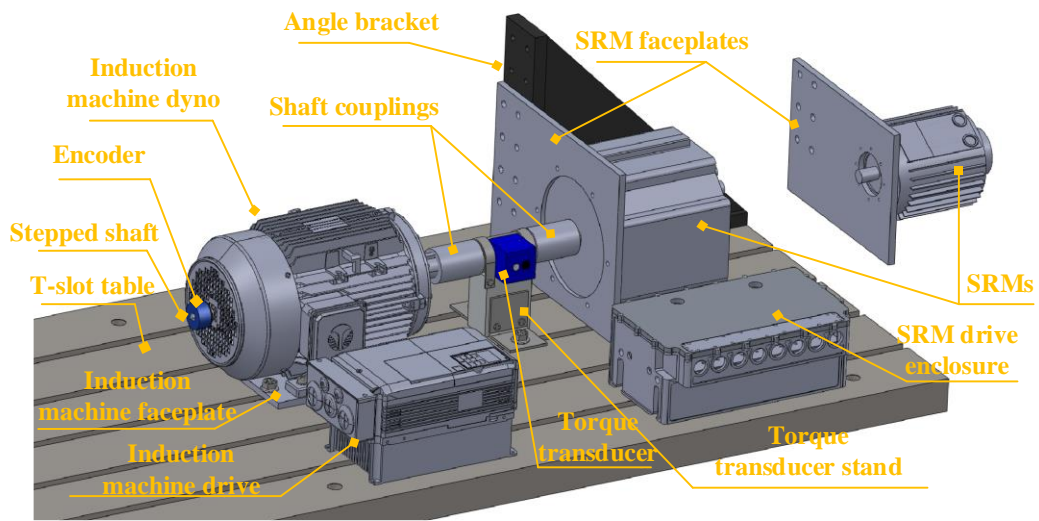


Fig. 4.6. Overview of the SRM experimental setup design.

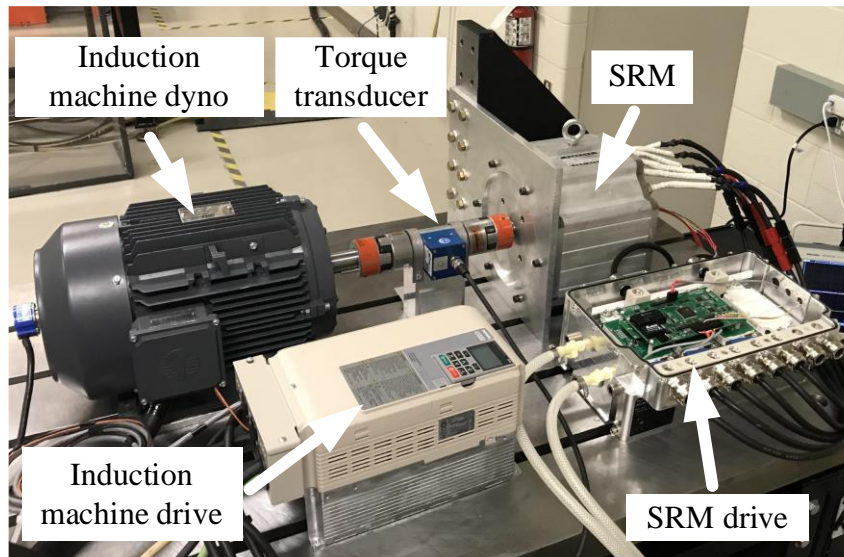


Fig. 4.7. Picture of the final experimental setup.

The detailed design procedure of the high-power inverter for SRM shown in Fig. 4.7 is illustrated in [111]. Asymmetric half-bridge Insulated-Gate Bipolar

Transistor (IGBT) modules F4-400R12ME4\_B29 provided by Infineon in 2013 were used to construct the SRM converter. However, this switch module was shut down by the manufacture a few years later. In this thesis, the same inverter enclosure, bus bar, heat sink, and dc capacitors in [111] are used, as shown in Fig. 4.8. The previous switch module is replaced by F4-250R17MP4\_B11, which is an H-bridge IGBT module. The 2SC0106TA-12 is selected to drive the replaced IGBT module.

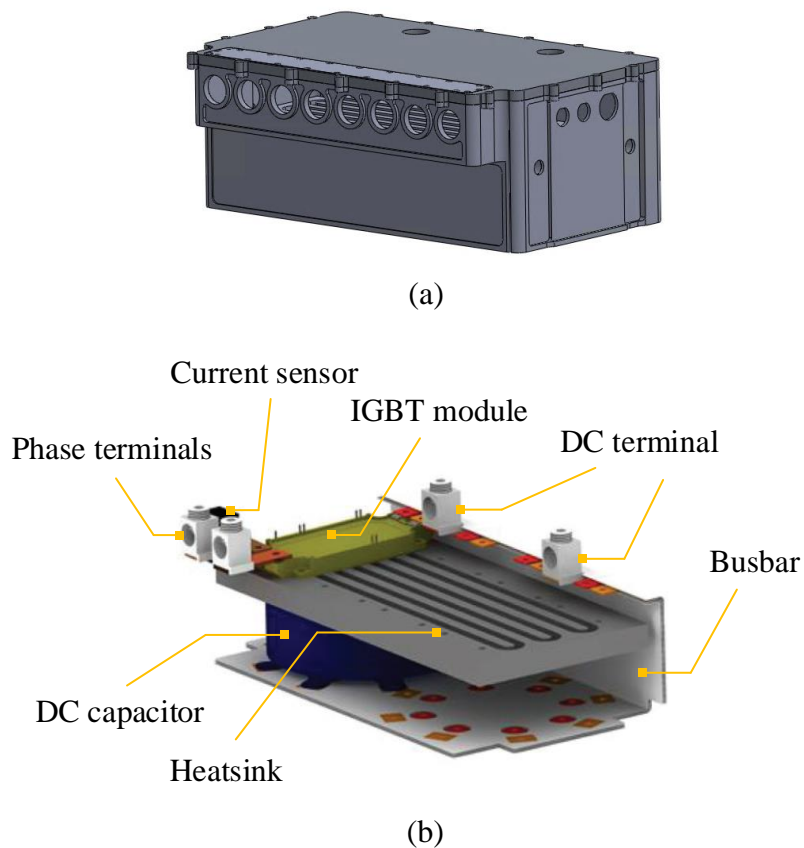


Fig. 4.8. 3D model of inverter design. (a). Enclosure. (b). Inverter model [111].

## 4.4 Measurement of Static Electromagnetic

### Characteristics of SRM

Generally, the dynamic SRM model is built using the static flux linkage and static torque characteristics. These two characteristics can be easily obtained by the finite element method with accurate geometrical dimensions. However, the negligible winding effects and the material properties may affect the accuracy of the characteristics. Since the detailed dimensions of the reference SRM are unknown, in this thesis, the static electromagnetic characteristics of SRM are measured by experiments.

#### 4.4.1 Static Flux Linkage Characteristic

The flux linkage can be derived from the phase voltage equation of SRM. It is expressed as

$$\lambda(\theta, i) = \int_0^t [V(t) - Ri(t)] dt \quad (4.1)$$

where  $V$ ,  $i$ ,  $R$  and  $\theta$  represent the phase voltage, phase current, phase resistance, and rotor position, respectively. It can be observed from (4.1) that the flux linkage can be indirectly calculated by the  $V$ ,  $i$ , and  $R$ .

Fig. 4.9 shows the picture of the flux linkage measurement platform. A horizontal & vertical rotary table diving plate is used to fix the SRM rotor to a

certain position. An oscilloscope is used to record the real-time phase voltage and current. During the test, the rotor position of the SRM is monitored by the resolver to ensure that the position is not changed. This is essential because the flux linkage is the function of the rotor position and current. If the motor shaft is not well clamped, a possible displacement might be observed when a voltage pulse is applied.

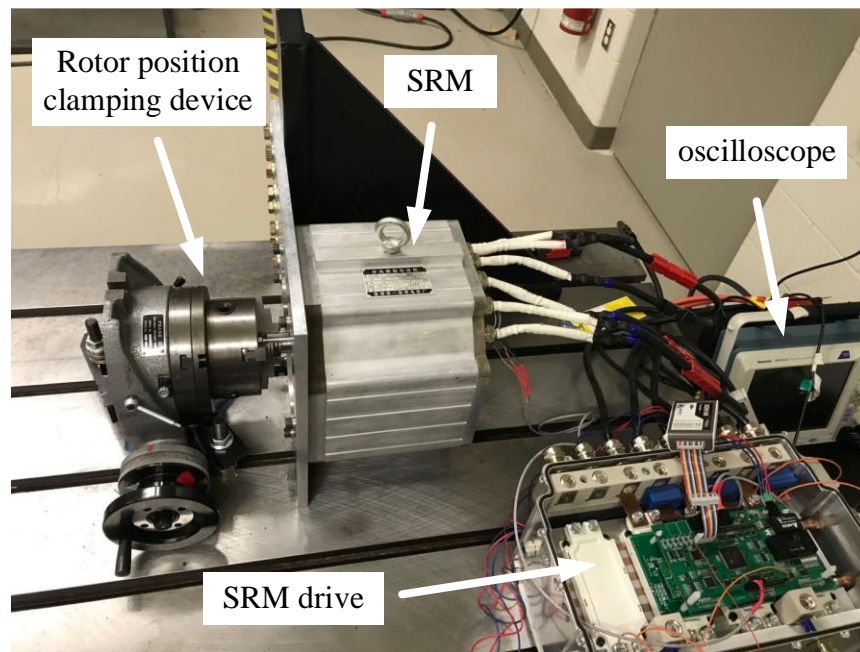


Fig. 4.9. Picture of the flux linkage measurement platform.

The measurement procedure is shown as follows:

- 1) Measure the phase winding resistance using a Micro-Ohmmeter. This is shown in Fig. 4.10.
- 2) Fix the SRM rotor to a certain position using the clamping device, as shown in Fig. 4.9. In this test, the first rotor position is set to  $180^\circ$ , which is the aligned position.
- 3) Apply a low-frequency pulsed dc voltage to the SRM phase winding, and then record the phase voltage and phase current using the oscilloscope.
- 4) Calculate the flux linkage by (4.1). Since the voltage is only applied for a short time, the temperature variation of the phase winding can be neglected. Thus, the phase resistance measured in step 1) is directly used in the calculation.
- 5) Repeat steps 2) and 3) for all the expected current levels and rotor positions.



Fig. 4.10. Measurement of the phase winding resistance.

Fig. 4.11 shows the flux linkage measurement results. Although the rated current of the reference SRM is 81.7A, the maximum measurement current is set to 122 A to make room for the current peaks in practice. Since the rotor and stator of the SRM are symmetric, the rotor position is varied from 180° to 0° in the test. The other half of the flux linkage characteristic can be obtained by mirroring.

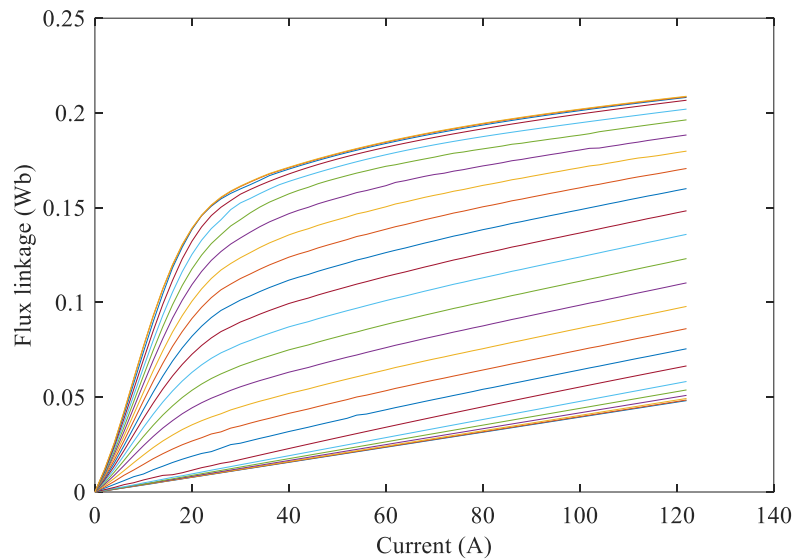


Fig. 4.11. Measurement result of flux linkage.

#### 4.4.2 Static Torque Characteristic

The static torque characteristic can also be experimentally measured. However, this needs static (reaction) torque transducer, not the dynamic one [112]. In this thesis, the electromagnetic torque is derived from the measured flux linkage LUT.

The electromagnetic torque can be calculated from the co-energy, as expressed in (4.2). While the co-energy can be derived from the flux linkage, as expressed in (4.3).

$$T_e = \left. \frac{\partial W_c}{\partial \theta} \right|_{i=\text{constant}} \quad (4.2)$$

$$W_c = \int \lambda di \quad (4.3)$$

By combining (4.2) and (4.3), the static torque characteristic can be obtained. The results are shown in Fig. 4.12.

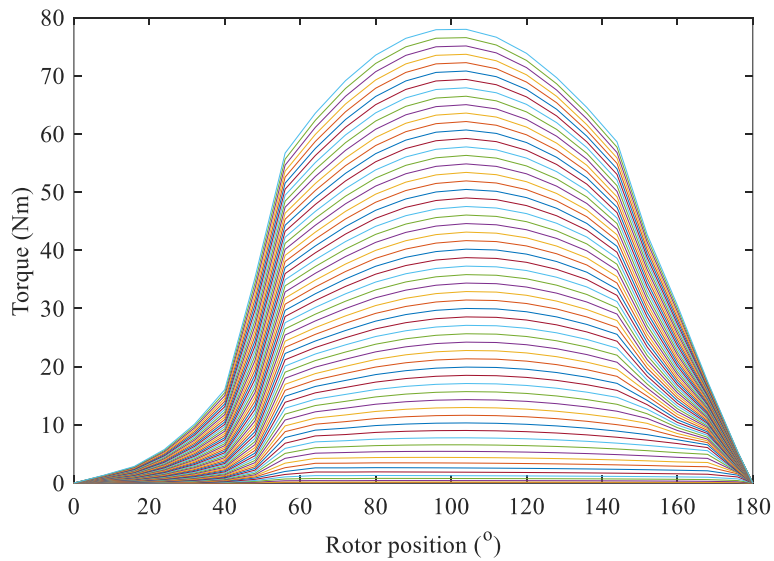


Fig. 4.12. Static torque characteristic.

## 4.5 Conclusion

This chapter describes the design and implementation of a switched reluctance machine drive setup from the view of device selection, mechanical design and electrical design. Then, the static flux linkage characteristic of the reference SRM is experimentally measured. The characterization procedure is presented. The static torque characteristic is derived from the measured flux linkage.

## **Chapter 5**

### **A New Torque Sharing Function**

### **Method For Switched Reluctance**

### **Machines With Lower Current**

### **Tracking Error**

#### **5.1 Introduction**

Torque ripple is one of the main inherent drawbacks of SRM, which can be detrimental to the lifetime of the rotating components. It can also cause drivetrain vibration and acoustic noise. This chapter proposes an offline torque sharing function for torque ripple reduction in switched reluctance machines. The

drawbacks of the existing conventional optimization-based TSFs are firstly analyzed in detail. Then the proposed current reference generation strategy is stated. An optimization problem is formulated to shape the current reference for the objective of minimizing the torque ripple and copper losses, while maintaining the required average output torque at the given operating speed. Finally, the performance of the proposed TSF is compared with the conventional TSFs and existing optimization-based TSFs through both simulations and experiments.

## 5.2 Conventional and Optimization-based TSFs

In the conventional TSFs, the reference torque  $T_{ref}$  is distributed among the phases using specific mathematical expressions. The general expression for a TSF can be written as in (1), where  $\theta$ ,  $\theta_{on}$ ,  $\theta_{off}$ , and  $\theta_{ov}$  represent the rotor position, turn-on, turn-off, and overlapping angles, respectively.  $f_r$  and  $f_f$  denote the rise and fall functions.

$$T_{ref} = \begin{cases} 0, & \theta < \theta_{on} \\ T_{ref} \cdot f_r, & \theta_{on} \leq \theta < \theta_{on} + \theta_{ov} \\ T_{ref}, & \theta_{on} + \theta_{ov} \leq \theta < \theta_{off} \\ T_{ref} \cdot f_f, & \theta_{off} \leq \theta < \theta_{off} + \theta_{ov} \\ 0, & \theta \geq \theta_{off} + \theta_{ov} \end{cases} \quad (5.1)$$

In (5.1), the overlapping angle needs to meet (5.2). Thus, negative phase torque is not allowed in the conventional TSFs.

$$\theta_{ov} + \theta_{off} \leq \frac{\theta_p}{2} \quad (5.2)$$

where  $\theta_p$  represent the pole pitch.

Linear, cubic, sinusoidal/cosine, and exponential functions are commonly used in the conventional TSFs [27].

(1) Linear TSF:

The rise and fall functions of the linear TSF are expressed as in (5.3) and (5.4), respectively. The phase torque profiles are shown in Fig. 5.1.  $\theta_u$  and  $\theta_a$  represent the unaligned and aligned position, respectively.

$$f_{rise}^{lin}(\theta) = \frac{1}{\theta_{ov}}(\theta - \theta_{ov}) \quad (5.3)$$

$$f_{fall}^{lin}(\theta) = 1 - \frac{1}{\theta_{ov}}(\theta - \theta_{off}) \quad (5.4)$$

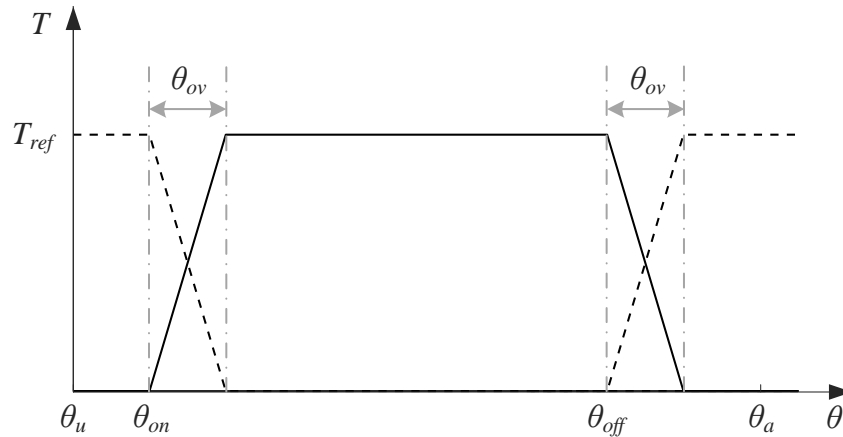


Fig. 5.1. Phase torque profiles of the linear TSF.

(2) Cubic TSF:

The rise and fall functions of the cubic TSF are expressed as in (5.5) and (5.6), respectively. The phase torque profiles are shown in Fig. 5.2.

$$f_{rise}^{cub}(\theta) = \frac{3}{\theta_{ov}^2}(\theta - \theta_{on})^2 - \frac{2}{\theta_{ov}^3}(\theta - \theta_{on})^3 \quad (5.5)$$

$$f_{fall}^{cub}(\theta) = 1 - f_{rise}^{cub}(\theta - \theta_{off} + \theta_{on}) \quad (5.6)$$

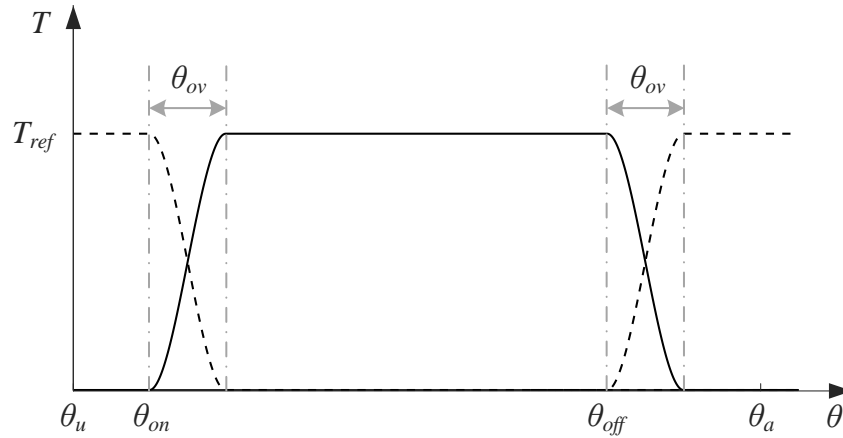


Fig. 5.2. Phase torque profiles of the cubic TSF.

(3) Sinusoidal TSF:

The rise and fall functions of the sinusoidal TSF are expressed as in (5.7) and (5.8), respectively. The phase torque profiles are shown in Fig. 5.3.

$$f_{rise}^{sin}(\theta) = \frac{1}{2} - \frac{1}{2} \cos \frac{\pi}{\theta_{ov}}(\theta - \theta_{on}) \quad (5.7)$$

$$f_{fall}^{sin}(\theta) = \frac{1}{2} + \frac{1}{2} \cos \frac{\pi}{\theta_{ov}}(\theta - \theta_{off}) \quad (5.8)$$

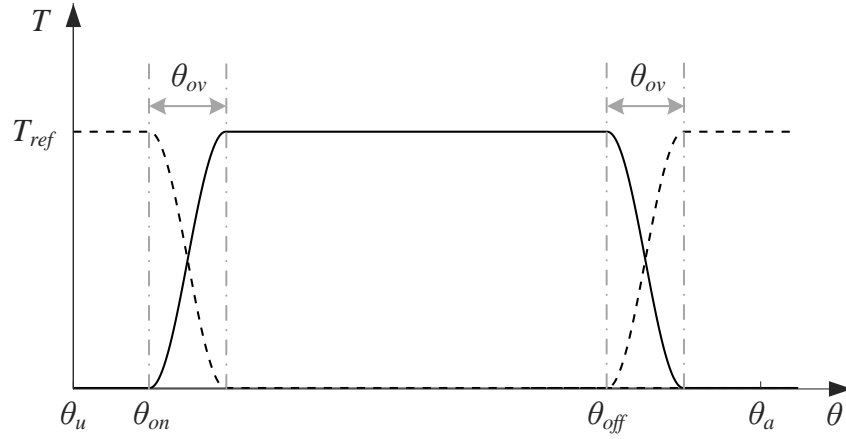


Fig. 5.3. Phase torque profiles of the sinusoidal TSF.

(4) Exponential TSF:

The rise and fall functions of the linear TSF are expressed as in (5.9) and (5.10), respectively. The phase torque profiles are shown in Fig. 5.4.

$$f_{rise}^{expo}(\theta) = 1 - \exp\left(\frac{-(\theta - \theta_{on})^2}{\theta_{ov}}\right) \quad (5.9)$$

$$f_{fall}^{expo}(\theta) = \exp\left(\frac{-(\theta - \theta_{off})^2}{\theta_{ov}}\right) \quad (5.10)$$

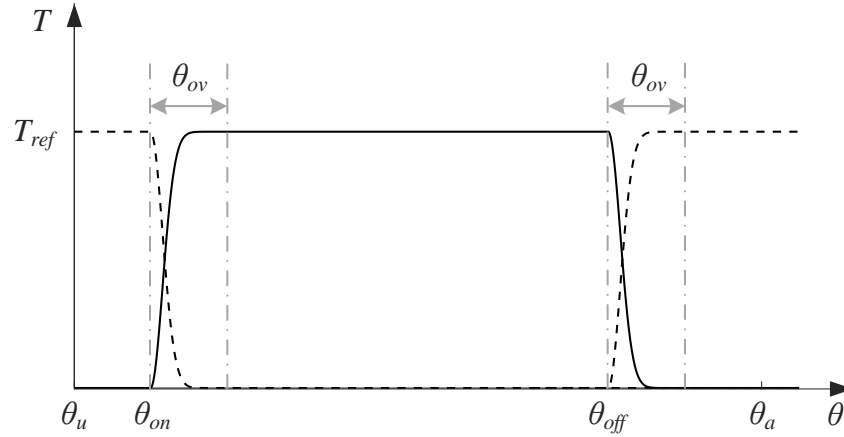


Fig. 5.4. Phase torque profiles of the exponential TSF.

These functions (5.3)-(5.10) simplify the nonlinear problem by parameterizing the torque and current waveforms. However, the precision of the torque waveform approximation is limited because there is no theoretical relationship between these mathematical expressions and motor characteristics. Thus, they have inherent torque and current tracking error.

Unlike the conventional TSFs, which model the shape of the phase torque to reduce the torque ripple, the optimization-based TSFs [39]–[42] derive the current reference by solving an optimization problem. For example, the objective function in [41] was represented as (5.11)

$$J = i_k^2 + \sigma i_{k-1}^2 \quad (5.11)$$

and the constraints of the optimization problem were defined as

$$0 \leq i_k \leq i_{rated}, 0 \leq i_{k-1} \leq i_{rated} \quad (5.12)$$

$$T_{ref} = T(i_k, \theta_k) + T(i_{k-1}, \theta_{k-1}) \quad (5.13)$$

$$\left| \frac{\Delta \lambda_k(i, \theta)}{\Delta t} \right| \leq V_{dc} - i_k R, \left| \frac{\Delta \lambda_{k-1}(i, \theta)}{\Delta t} \right| \leq V_{dc} - i_{k-1} R \quad (5.14)$$

In (5.11)-(5.14),  $i_k$ ,  $i_{k-1}$ , and  $i_{rated}$  represent the incoming phase current, outgoing phase current, and rated phase current, respectively.  $\lambda_k$  and  $\lambda_{k-1}$  denote the flux linkage of the incoming phase and outgoing phase.  $\Delta t$ ,  $V_{dc}$ ,  $R$ , and  $\sigma$  indicate the sampling period, DC-link voltage, phase resistance, and the weight parameter, respectively.

For a given weight parameter  $\sigma$ , the incoming and outgoing phase currents can be derived by solving the optimization problem with respect to the rotor position. Genetic Algorithm (GA) is used to optimize the weight parameter  $\sigma$  based on the torque and speed references. Compared to the conventional TSFs, no specific mathematical expressions are used, which provides more flexibility when defining the current reference. However, the objective function in [41] includes only the phase current. Thus, the turn-on and turn-off angles cannot be optimized directly. Furthermore, the negative torque is not allowed for the TSF in [41], which means that the turn-on angle cannot be advanced beyond the unaligned position, and the demagnetization current decays to zero before the aligned position. Thus, the phase current dynamics are not sufficiently considered when using the constraints in (5.14). Insufficient rise time for the incoming phase current and insufficient fall time for the outgoing phase might be obtained. The above drawbacks might cause current tracking error and poor torque-speed performance, especially at high-speed conditions.

A detailed explanation on the drawbacks of the TSF in [41] is provided as follow:

In [41], the root-mean-square (RMS) values of the torque ripple and phase current are minimized by GA. Fig. 5.5 shows the flowchart for the TSF in [41]. In each iteration of the optimization, GA assigns a value to the weight parameter  $\sigma$ , and then the current reference is derived by solving (5.11)-(5.14). After that, the dynamic simulation of the SRM model is carried out, and the RMS values of torque ripple  $T_{Rms}$  and phase current  $I_{rms}$  are calculated from the simulation results. If the results are not satisfied, another iteration will start with a new weight parameter  $\sigma$  provided by GA. The optimization will stop until  $T_{Rms}$  and  $I_{rms}$  are minimized.

It can be observed from the cost function and constraints that the turn-on and turn-off angles cannot be directly optimized for the TSF in [41]. The information for these two angles is not directly included in the (5.11)-(5.14). For analysis purposes, the turn-on angle for the TSF in [41] represents the rotor angle where the phase current starts rising from zero.

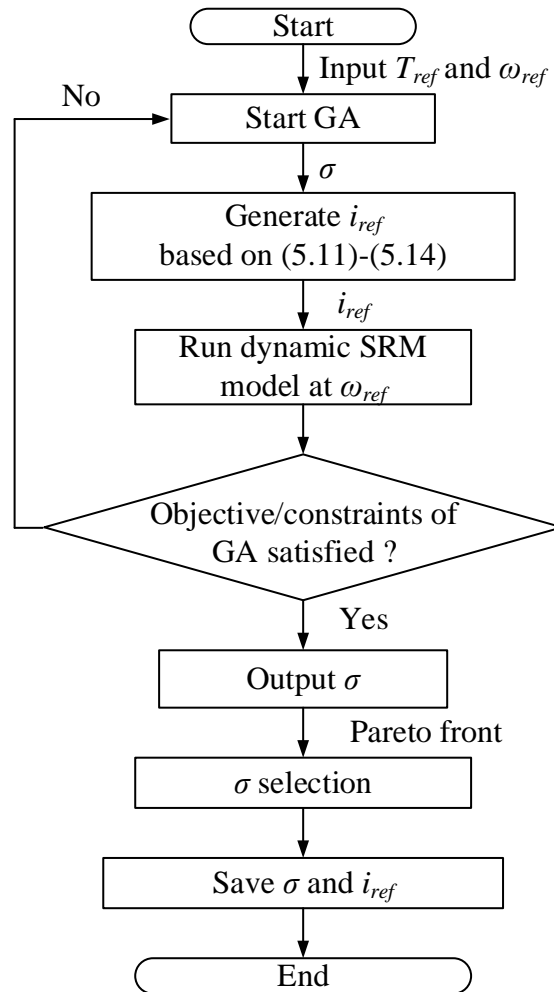
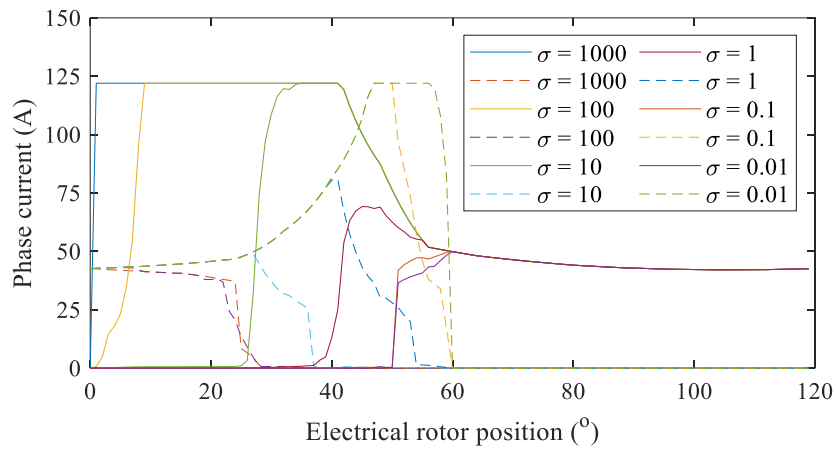


Fig. 5.5. Flowchart for the TSF in [41].

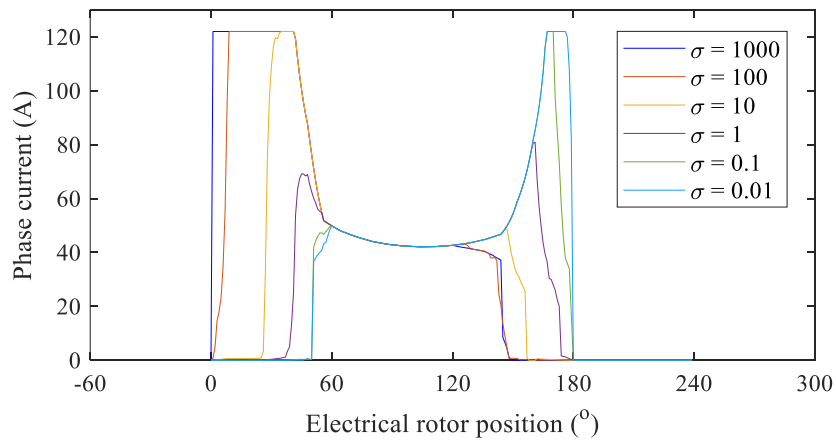
Theoretically, if the turn-on angle  $\theta_{on}$  of the incoming phase is before the unaligned position  $\theta_u$ , the incoming phase current  $i_k$  will be larger than zero in the  $[\theta_{on}, \theta_u]$  interval. It means that the generated torque of the incoming phase  $T(i_k, \theta_k)$  is negative (or almost equal to zero) when the rotor position  $\theta_k$  is in the  $[\theta_{on}, \theta_u]$  interval. In order to meet the constraint (5.13) in this interval, the torque of the outgoing phase needs to be increased to compensate for the negative torque

generated by the incoming phase. Thus, the outgoing phase current  $i_{k-1}$  needs to increase, which increases the value of the cost function  $J$  in (5.11). To summarize, the negative turn-on angle for the TSF in [41] will result in negative phase torque (or zero torque), thereby, increase the value of the phase current, and finally increases the value of the cost function. Therefore, the optimizer will not allow phase current before the unaligned position.

Simulations are carried out to validate the above analysis. In the simulation, the operating speed and torque commands are 500 r/min and 20 Nm, respectively. The weight parameter  $\sigma$  in the cost function (5.11) is varied from 0.01 to 1000. Fig. 5.6 below shows the waveforms of the generated current reference for the TSF in [41]. The  $x$ -axis is the electrical rotor position of the incoming phase. The unaligned position is defined as  $0^\circ$ , and the aligned position is  $180^\circ$ . For a given  $\sigma$ , the incoming and outgoing phase current references can be derived by solving (5.11)-(5.14). Since the phase currents of SRM are symmetric, only the current in the range of  $120^\circ$  (for 3-phase SRM) needs to be calculated. Fig. 5.6(a) shows the calculation results. The solid lines represent the current reference of the incoming phase, and the dash lines represent the current reference of the outgoing phase. Fig. 5.6(b) shows the complete phase current reference in one electrical cycle, which is derived by combining the incoming and outgoing phase currents.



(a)



(b)

Fig. 5.6. Phase current references for the TSF in [41] with varying weight parameters. (a). Incoming and outgoing phase current references. (b). Phase current references in one electrical cycle.

From Fig. 5.6, it can be observed that by increasing  $\sigma$ , the outgoing phase current is penalized, and the incoming phase current is advanced. However, the turn-on angle will approach to the unaligned position, because the negative turn-on

angle results in negative phase torque, thereby, increases the value of the cost function. Thus, the optimizer will not provide phase current beyond the unaligned position. Similarly, by decreasing  $\sigma$ , the incoming phase current is penalized, and the outgoing phase current moves towards the aligned position ( $60^\circ$  in Fig. 5.6(a) or  $180^\circ$  in Fig. 5.6(b)). However, the demagnetization current has to decay to zero before the aligned position to avoid negative phase torque.

Therefore, the TSF in [41] is not constructed to allow negative torque for the current reference. If one phase generates negative (or zero) torque, the other phase current reference needs to be increased to compensate for it, which increases the value of the cost function  $J$ . Thus, the turn-on angle is not allowed to be advanced beyond the unaligned position, and  $\theta_{zero}$  (the rotor position where the demagnetization phase current decays to zero after  $\theta_{off}$ ) is not allowed to be beyond the aligned position.

### 5.3 Proposed Offline TSF

Fig. 5.7 shows the flowchart of the proposed TSF. A multi-objective Genetic Algorithm (GA) is used to establish an optimization loop that determines suitable turn-on and turn-off angles. In each iteration of the optimization, the proposed four-step current reference generation strategy in Fig. 5.8 is applied to obtain the current reference ( $i_{ref4}$  in Fig. 5.7). Then, a dynamic simulation is carried out to track this current reference, and the torque ripple and copper losses are evaluated. The

optimization loop repeats until the turn-on and turn-off angles that generates the current reference with the minimum RMS value and the minimum torque ripple are achieved.

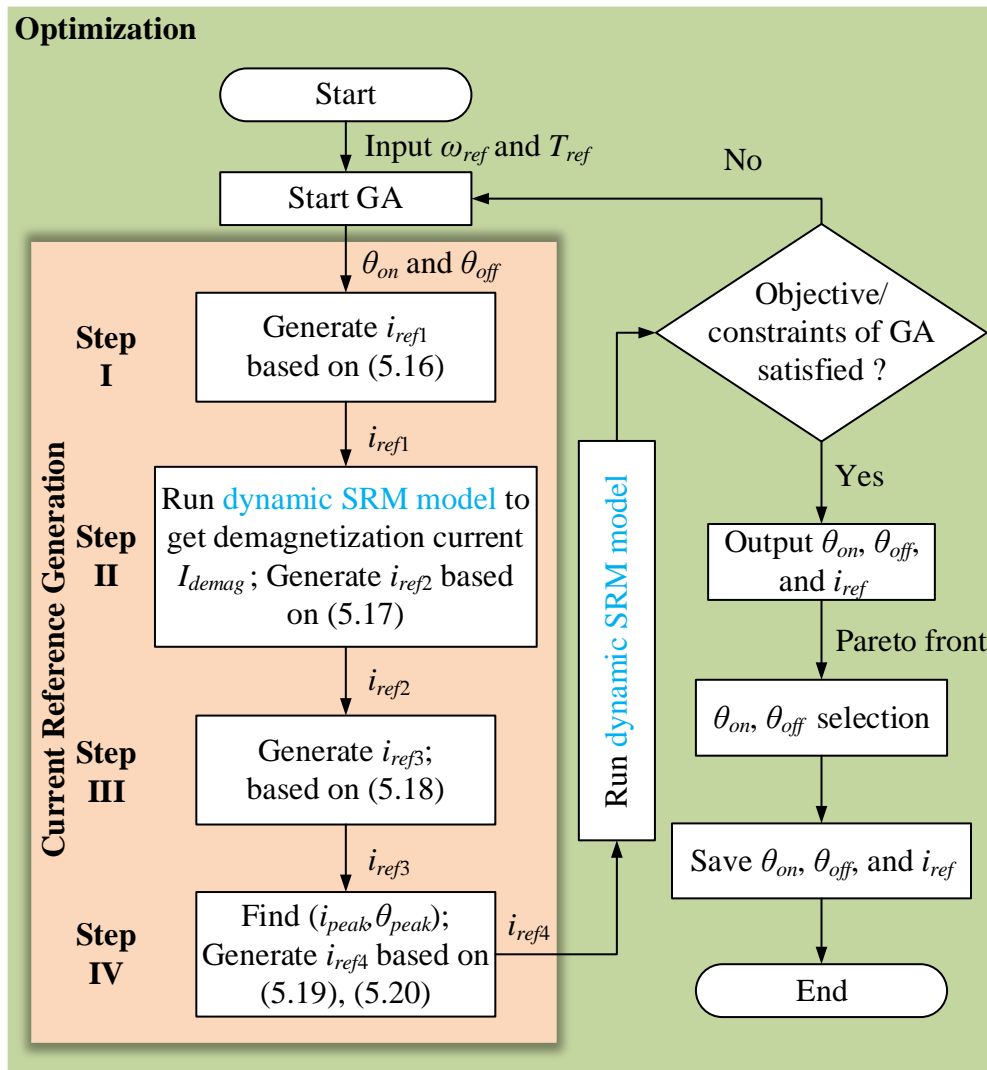


Fig. 5.7. Flowchart for the proposed offline TSF.

Fig. 5.8 shows the current waveforms generated in each step of the current reference generation strategy in Fig. 5.7. The solid lines in Fig. 5.8 represent the adopted current reference in each step. The dash lines denote the current reference from the previous steps, which are replaced in the present step. Current references generated in each step are shown in different colors. The dynamic model of SRM, which is used in Step II and optimization as shown in Fig. 5.7, is built using the measured torque-current-position ( $T-i-\theta$ ) and flux linkage-current-position ( $\lambda-i-\theta$ ) characteristics of the SRM. These characteristics can be obtained by measurements or finite element analysis [43], [113]. An example for building the dynamic model of an SRM in Matlab/Simulink has been provided in [111].

The current reference generation is implemented in four steps. As shown in Fig. 5.7, the current reference generation strategy is applied in each iteration of the optimization. In Step I, the turn-on angle,  $\theta_{on}$  and turn-off angle,  $\theta_{off}$  are provided by GA, which could also be arbitrarily selected in the first iteration of the optimization. Considering no negative torque and no overlapping conduction at this step, it can be assumed that the reference torque  $T_{ref}$  is provided only by one of the phases within the conduction interval  $[180^\circ - \theta_{fi}, \theta_{off}]$ , as shown in Fig. 5.8(a).  $\theta_{fi}$  is the electrical phase shift between the phases of SRM and it is defined as

$$\theta_{fi} = \frac{360^\circ}{m} \quad (5.15)$$

where  $m$  denotes the number of phases.

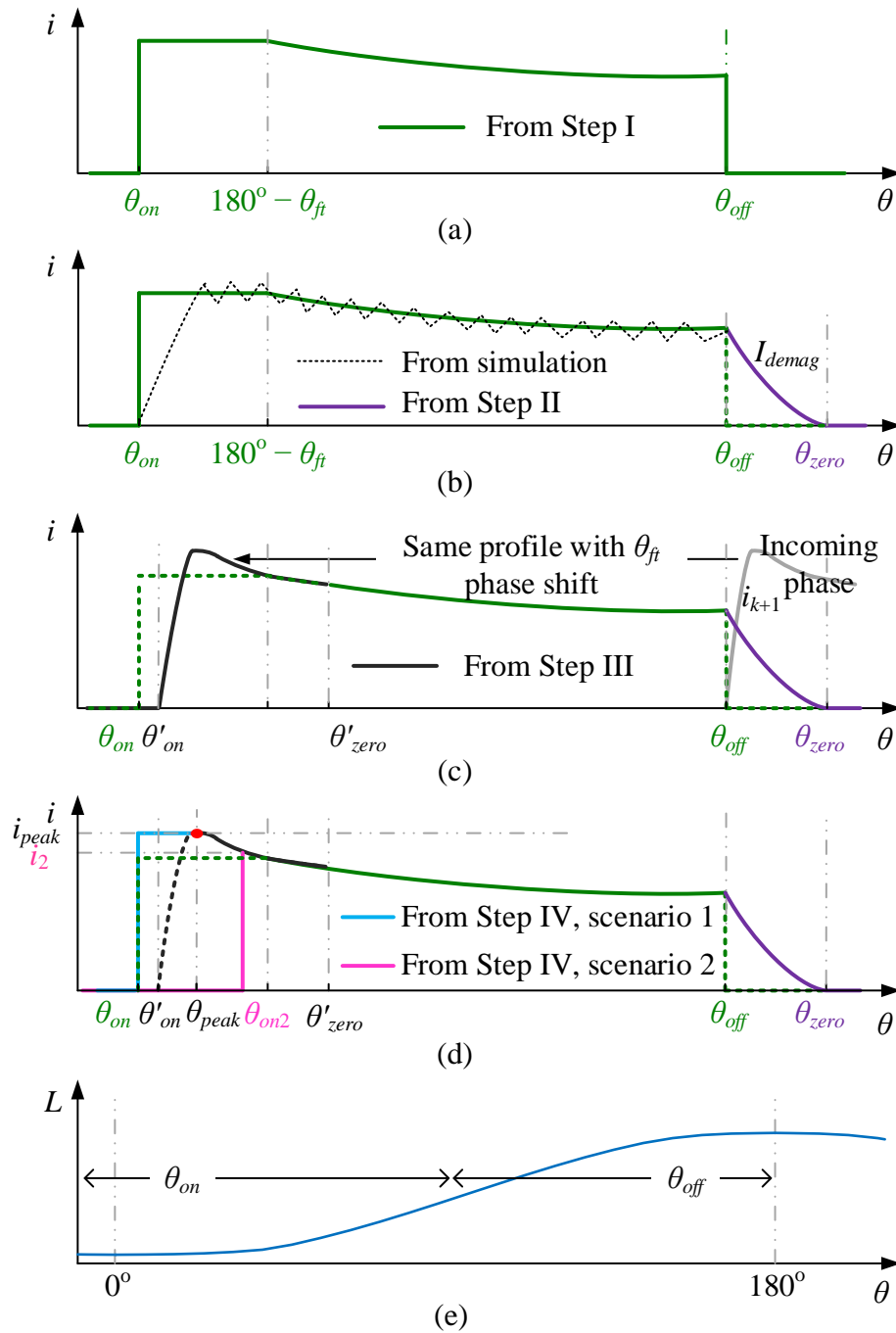


Fig. 5.8. Reference current profile from each step. (a) Step I. (b) Step II. (c) Step III. (d) Step IV. (e) Inductance profile.

Thus, in the  $[180^\circ - \theta_{ft}, \theta_{off}]$  interval, the reference phase current in Step I is derived using the inverse  $T$ - $i$ - $\theta$  lookup table (LuT)  $I_{T,\theta}^{inv}$ , by applying the reference torque as an input. From  $\theta_{on}$  to  $180^\circ - \theta_{ft}$  in Fig. 5.8(a), the reference current remains unchanged. Hence, the current profile in Step I,  $i_{ref1}$  is expressed as

$$i_{ref1} = \begin{cases} 0, & \theta < \theta_{on} \\ I_{T,\theta}^{inv}(T_{ref}, 180^\circ - \theta_{ft}), & \theta_{on} \leq \theta < 180^\circ - \theta_{ft} \\ I_{T,\theta}^{inv}(T_{ref}, \theta), & 180^\circ - \theta_{ft} \leq \theta < \theta_{off} \\ 0, & \theta \geq \theta_{off} \end{cases}. \quad (5.16)$$

It should be noted that the assumptions made above are only used in Step I.  $\theta_{on}$  and  $\theta_{off}$ , arbitrarily selected in Step I, will be tuned later in the optimization process, and the final current reference will allow negative torque and phase overlapping.

In Step II, the dynamic simulation of the SRM model is carried out for one electrical cycle using hysteresis current control at the given operating speed  $\omega_{ref}$ .  $i_{ref1}$  obtained from Step I is used as the current reference. As shown in Fig. 5.8(b), the black dash line represents the actual phase current from the simulation results, while the green line denotes the current reference  $i_{ref1}$  from Step I. By monitoring the actual phase current in the simulation, the phase current waveform within  $[\theta_{off}, \theta_{zero}]$  can be obtained.  $\theta_{zero}$  is found from the phase current waveform from the dynamic simulation, which is the angle when the phase current reaches to zero after  $\theta_{off}$ . The phase current waveform within  $[\theta_{off}, \theta_{zero}]$  is defined as  $I_{demag}$ . By adding  $I_{demag}$  into  $i_{ref1}$  expression in (5.16), the current reference for Step II can be derived as

$$i_{ref2} = \begin{cases} 0, & \theta < \theta_{on} \\ I_{T,\theta}^{inv}(T_{ref}, 180^\circ - \theta_{ft}), & \theta_{on} \leq \theta < 180^\circ - \theta_{ft} \\ I_{T,\theta}^{inv}(T_{ref}, \theta), & 180^\circ - \theta_{ft} \leq \theta < \theta_{off} \\ I_{demag}, & \theta_{off} \leq \theta < \theta_{zero} \\ 0, & \theta \geq \theta_{zero} \end{cases} \quad (5.17)$$

In the  $[\theta_{off}, \theta_{zero}]$  interval in Fig. 5.8(b), the outgoing phase current is  $I_{demag}$ . Therefore, the outgoing phase torque is  $T_{i,\theta}(I_{demag}, \theta)$ . In a TSF, since the sum of the torques generated by the adjacent phases should be equal to the reference torque,  $T_{ref}$ , the torque of the incoming phase  $T_{k+1}$  within  $[\theta_{off}, \theta_{zero}]$  can be expressed as

$$T_{k+1} = T_{ref} - T_{i,\theta}(I_{demag}, \theta), \quad \theta_{off} \leq \theta \leq \theta_{zero}. \quad (5.18)$$

Then, the required current for the incoming phase,  $i_{k+1}$  can be calculated as in (5.19) by using the inverse  $T$ - $i$ - $\theta$  LuT:

$$i_{k+1} = I_{T,\theta}^{inv}(T_{k+1}, \theta - \theta_{ft}), \quad \theta_{off} \leq \theta \leq \theta_{zero}. \quad (5.19)$$

Here,  $i_{k+1}$  is calculated by considering the phase shift  $\theta_{ft}$ , because  $T_{k+1}$  is generated at the beginning of the conduction period of the incoming phase. Fig. 5.8(c) shows the incoming phase current,  $i_{k+1}$  within  $[\theta_{off}, \theta_{zero}]$  with the gray line. Since the phase currents are symmetric, the outgoing phase current should have the same shape at  $[\theta_{off} - \theta_{ft}, \theta_{zero} - \theta_{ft}]$  interval. Please note from Fig. 5.8(c), that this creates an ideal turn-on angle,  $\theta'_{on}$  which equals to  $\theta_{off} - \theta_{ft}$ .  $\theta_{on}$ , which was arbitrarily selected in Step I, might be larger or smaller than  $\theta'_{on}$ . These two scenarios are addressed in Step IV. Therefore, the ideal current reference in Step III,  $i_{ref3}$ , is expressed as in (5.20) and it is shown in Fig. 5.8(c) with three solid lines

in green ( $[\theta'_{zero}, \theta_{off}]$  from Step I), purple ( $[\theta_{off}, \theta_{zero}]$  from Step II), and dark ( $[\theta'_{on}, \theta'_{zero}]$  from Step III):

$$i_{ref3} = \begin{cases} 0, & \theta < \theta'_{on} \\ I_{T,\theta}^{inv} \left( T_{ref} - T_{i,\theta} \left( I_{demag}, \theta + \theta_{ft} \right), \theta \right), & \theta'_{on} \leq \theta < \theta'_{zero} \\ I_{T,\theta}^{inv} \left( T_{ref}, \theta \right), & \theta'_{zero} \leq \theta < \theta_{off} \\ I_{demag}, & \theta_{off} \leq \theta < \theta_{zero} \\ 0, & \theta \geq \theta_{zero} \end{cases} \quad (5.20)$$

where  $\theta'_{zero}$  is  $\theta_{zero} - \theta_{ft}$ . The new current profile in Step III (the dark waveform in Fig. 5.8(c)) replaces the previous one in the  $[\theta_{on}, \theta'_{zero}]$  interval (the green dashed line in Fig. 5.8(c)).

The current reference,  $i_{ref3}$  is the ideal current reference for the given torque reference. If  $i_{ref3}$  could be perfectly tracked, there would be zero torque ripple. However,  $i_{ref3}$  in the  $[\theta'_{on}, \theta'_{zero}]$  interval was calculated from the  $T$ - $i$ - $\theta$  LuT. Hence, the current dynamics have not been taken into account. It cannot be known at this point whether  $i_{ref3}$  in Fig. 5.8(c) can be tracked by the inverter considering the rate of change of flux linkage at the given speed. Thus, the average torque and torque ripple in this interval cannot be guaranteed.

Besides, in  $i_{ref3}$  in Fig. 5.8(c), the turn-on angle  $\theta'_{on}$  equals to  $\theta_{off} - \theta_{ft}$ . Therefore, the conduction angle  $\theta_{off} - \theta'_{on}$  equals to  $\theta_{ft}$ , which is the phase shift between the phases of SRM. However, it is a common practice to have overlapping conduction in SRMs by advancing the turn-on angle. A negative turn-on angle is generally used at the high-speed operation to achieve higher average torque [58].

In order to address these issues, the current dynamics in  $i_{ref3}$  in the  $[\theta'_{on}, \theta'_{zero}]$  interval should be replaced with the dynamics that is calculated from the dynamic model of the SRM. This is accomplished through the optimization shown in Fig. 5.7. The current reference generation strategy is applied in each iteration to find the  $\theta_{on}$  and  $\theta_{off}$  that achieve the minimum torque ripple and RMS current. Before that, the current dynamics calculated in Step III from the  $T$ - $i$ - $\theta$  LuT should be removed. However, a current reference should still be provided to the optimization model to achieve the required average torque. This is accomplished in Step IV.

Step IV finds the peak value of  $i_{ref3}$  within  $[\theta'_{on}, \theta'_{zero}]$  interval. This point is designated as  $(\theta_{peak}, i_{peak})$  in Fig. 5.8(d), which should be achieved to deliver the reference torque. If  $\theta_{on}$ , which was arbitrarily selected in Step I, is smaller than  $\theta_{peak}$ , the current reference within  $[\theta_{on}, \theta_{peak}]$  is directly set to  $i_{peak}$  as shown in Fig. 5.8(d). In the optimization step, the conduction angles will be determined to achieve  $i_{peak}$  at  $\theta_{peak}$  with the minimum torque ripple and the minimum RMS current. Hence, for the case where  $\theta_{on}$  is smaller than  $\theta_{peak}$ , the current reference in Step IV is expressed as in (5.21). It is shown by four solid lines in Fig. 5.8(d) in green ( $[\theta'_{zero}, \theta_{off}]$  from Step I), purple ( $[\theta_{off}, \theta_{zero}]$  from Step II), dark ( $[\theta_{peak}, \theta'_{zero}]$  from Step III), and blue ( $[\theta_{on}, \theta_{peak}]$  from Step IV).

$$i_{ref4} = \begin{cases} 0, & \theta < \theta_{on} \\ i_{peak}, & \theta_{on} \leq \theta < \theta_{peak} \\ I_{T,\theta}^{inv} \left( T_{ref} - T_{i,\theta} \left( I_{demag}, \theta' \right), \theta \right), & \theta_{peak} \leq \theta < \theta'_{zero} \\ I_{T,\theta}^{inv} \left( T_{ref}, \theta \right), & \theta'_{zero} \leq \theta < \theta_{off} \\ I_{demag}, & \theta_{off} \leq \theta < \theta_{zero} \\ 0, & \theta \geq \theta_{zero} \end{cases}. \quad (5.21)$$

Since  $i_{ref3}$  was calculated from the inverted  $T$ - $i$ - $\theta$  LuT to achieve the given torque reference, the turn-on angle arbitrarily selected in Step I does not directly affect  $i_{ref3}$ . Therefore, it is possible that  $\theta_{on}$  could be selected larger than  $\theta_{peak}$  as shown with  $\theta_{on2}$  in Fig. 5.8(d). In this case, the peak value of  $i_{ref3}$  would be  $i_2$ . Then, the current reference within  $[\theta'_{on}, \theta_{on2}]$  is set to zero, while the current reference after  $\theta_{on2}$  remains the same. In this scenario,  $i_{ref4}$  is expressed as (5.22). It is shown by three solid lines in Fig. 5.8(d) in green ( $[\theta'_{zero}, \theta_{off}]$  from Step I), purple ( $[\theta_{off}, \theta_{zero}]$  from Step II), dark ( $[\theta_{on2}; \theta'_{zero}]$  from Step III). In Step IV,  $i_{ref4}$  is selected based on the relationship between  $\theta_{on}$  from Step I and  $\theta_{peak}$  from Step III and applied to the optimization model.

$$i_{ref4} = \begin{cases} 0, & \theta < \theta_{on2} \\ I_{T,\theta}^{inv} \left( T_{ref} - T_{i,\theta} \left( I_{demag}, \theta' \right), \theta \right), & \theta_{on2} \leq \theta < \theta'_{zero} \\ I_{T,\theta}^{inv} \left( T_{ref}, \theta \right), & \theta'_{zero} \leq \theta < \theta_{off} \\ I_{demag}, & \theta_{off} \leq \theta < \theta_{zero} \\ 0, & \theta \geq \theta_{zero} \end{cases}. \quad (5.22)$$

The current reference,  $i_{ref4}$  constitutes important details for the given torque reference: (i) the current reference shape to achieve the torque reference during the

single phase conduction, (ii) demagnetization current dynamics after  $\theta_{off}$ , and (iii) the peak current to achieve the required average torque.

In each iteration of the optimization, the dynamic simulation of the SRM model is carried out for one electrical cycle using hysteresis current control at the given speed.  $i_{ref4}$  obtained from Step IV is used as the current reference, as shown in Fig. 5.7. Operational parameters such as current sampling frequency and hysteresis current control bandwidth are all defined in the simulation so that their influences can be considered. From the simulation results, RMS value of the torque ripple  $T_{Rrms}$ , RMS value of the current  $I_{rms}$ , and the average torque  $T_{ave}$  are calculated. A multi-objective GA is implemented for the optimization. As depicted in Fig. 5.7, new  $\theta_{on}$  and  $\theta_{off}$  are provided by GA and then a new current reference is generated through Steps I to IV until  $T_{Rrms}$  and  $I_{rms}$  are minimized.  $T_{Rrms}$  and  $I_{rms}$  in one electrical cycle are defined as follows:

$$T_{Rrms} = \sqrt{\frac{1}{360^\circ} \int_{0^\circ}^{360^\circ} (T - T_{ave})^2 d\theta} \quad (5.23)$$

$$I_{rms} = \sqrt{\frac{1}{360^\circ} \int_{0^\circ}^{360^\circ} I^2 d\theta}. \quad (5.24)$$

$T_{ave}$  works as a constraint to maintain the required output torque in the optimization:

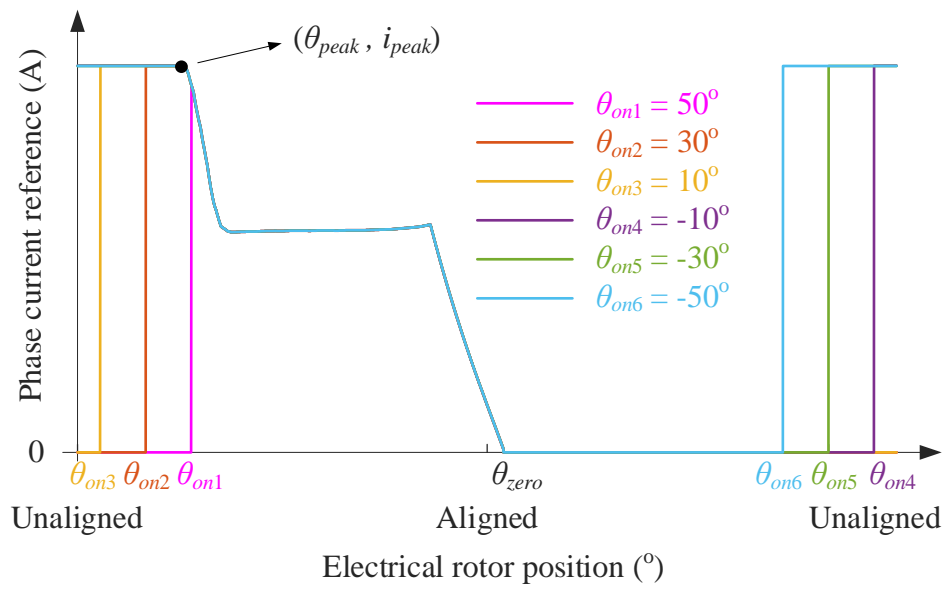
$$\left| \frac{T_{ave} - T_{ref}}{T_{ref}} \right| < \varepsilon \quad (5.25)$$

where  $\varepsilon$  is the tolerance. For example,  $\varepsilon = 0.1$  means the average torque needs to be larger than 90% of the reference torque.

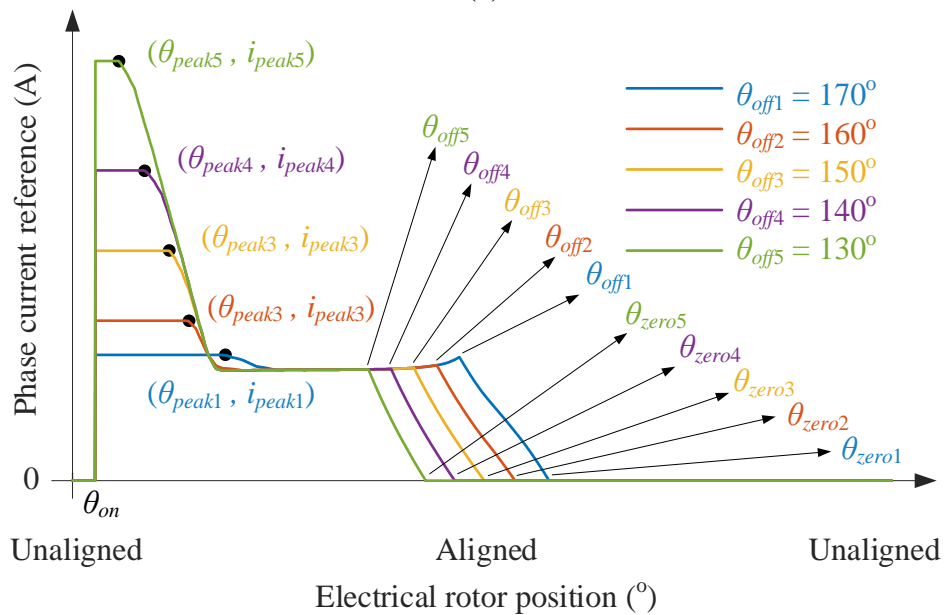
In each iteration,  $\theta_{on}$  and  $\theta_{off}$  are optimized by the multi-objective optimization, and then current reference is generated. Fig. 5.9 shows how  $\theta_{on}$  and  $\theta_{off}$  affect the current reference waveform with the proposed current reference generation strategy. As shown in Fig. 5.9(a), when  $\theta_{on}$  changes for a given  $\theta_{off}$ , only the current reference before  $\theta_{peak}$  changes. Different current dynamics can be obtained in the  $[\theta_{on}, \theta_{peak}]$  interval. This provides flexibility in the current rise time to achieve the peak current in each iteration. The average torque, torque ripple and RMS current before  $\theta_{peak}$  also vary with  $\theta_{on}$ , while they remain the same after  $\theta_{peak}$ . With an appropriate  $\theta_{on}$  and a given  $\theta_{off}$ ,  $i_{peak}$  can be achieved to deliver the reference torque while minimizing the torque ripple and RMS current. As shown in Fig. 5.9(b), when  $\theta_{off}$  changes for a given  $\theta_{on}$ , both  $I_{demag}$  and  $(\theta_{peak}, i_{peak})$  change. Various current references and dynamics within both  $[\theta_{on}, \theta'_{zero}]$  and  $[\theta_{off}, \theta_{zero}]$  intervals can be obtained, resulting in different  $T_{ave}$ ,  $T_{Rrms}$ , and  $I_{rms}$ . The current reference within the  $[\theta'_{zero}, \theta_{off}]$  interval is mainly due to single phase conduction, which is calculated from the torque reference. Therefore, except in the  $[\theta'_{zero}, \theta_{off}]$  interval, the current reference and, hence, the current dynamics are varied during the optimization process by changing  $\theta_{on}$  and  $\theta_{off}$ . After each iteration, the new conduction angles are used in the current reference generation strategy in Fig. 5.7. Since the optimization uses the dynamic model of the SRM, the current dynamics are optimized to guarantee the current tracking performance.

After the multi-objective optimization, a Pareto front is obtained, showing the tradeoff between  $T_{Rrms}$  reduction and  $I_{rms}$  reduction. Due to the constraint in

(5.25), the average torque for all the points on the Pareto front should satisfy the torque reference within the given tolerance. The final solution is selected as the one which provides an output torque closest to the reference torque. Fig. 5.10 shows an example of the final current reference.  $\theta_{on*}$  and  $\theta_{off*}$  represent the final chosen turn-on and turn-off angles.  $\theta_{peak*}$  and  $i_{peak*}$  denote the peak value and position of the peak current.



(a)



(b)

Fig. 5.9. Effect of the conduction angle. (a) Varying  $\theta_{on}$  when  $\theta_{off} = 160^\circ$ . (b) Varying  $\theta_{off}$  when  $\theta_{on} = 10^\circ$ .

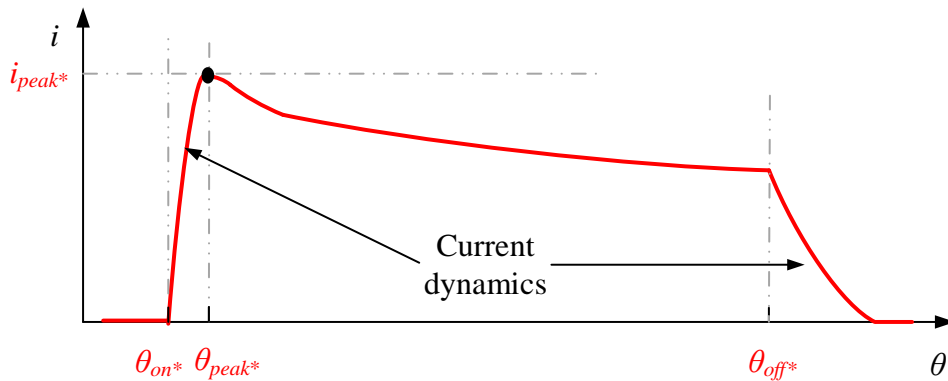


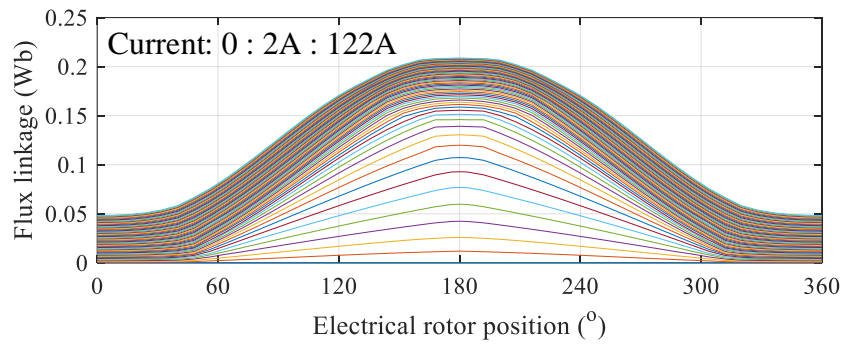
Fig. 5.10. An example of the final current reference.

## 5.4 Simulation Evaluation

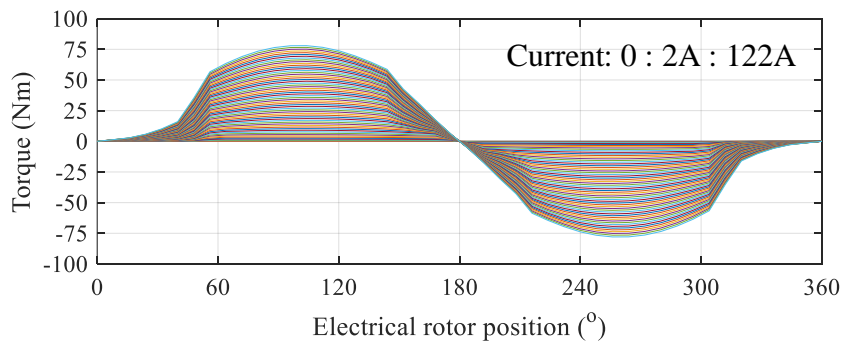
The performance of the proposed TSF is evaluated and compared with the conventional linear and cubic TSFs, and also the optimization-based TSF in [41]. A 3-phase 12/8 SRM has been used for this analysis. The design specifications of the 12/8 SRM are shown in Table 4.1. The outer diameter and the axial length of the motor are 274 mm and 230 mm, respectively. The dynamic model of the SRM is built using the experimentally-measured flux linkage and torque characteristics. These two LUTs are shown in Fig. 5.11. The rated current of the adopted SRM from the datasheet is 81.7A. In the characterization, the maximum current is set to 122 A. Both low- and high-speed operations are investigated. In all simulations, the current sampling frequency is 40 kHz, and the hysteresis current control band is 6 A. The dc-link voltage is set as 72 V.

Table 5.1. Design specifications of the 3-phase 12/8 SRM

Variable	Value	Unit
Rated power	5.5	kW
Rated speed	1000	r/min
Rated torque	52.53	Nm
DC-link voltage	72	V
Maximum speed	2500	r/min
Rated current	81.7	A



(a)



(b)

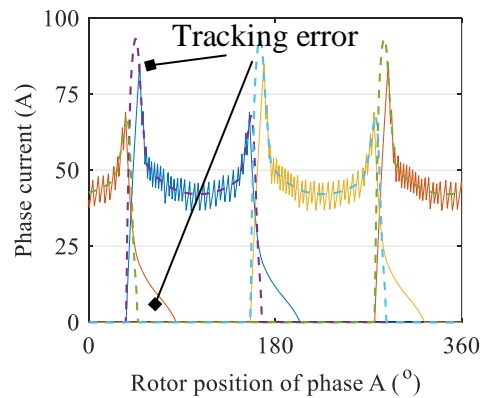
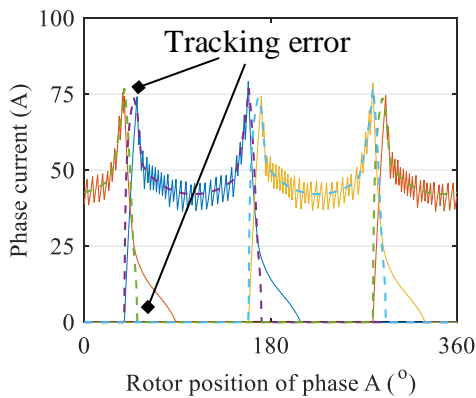
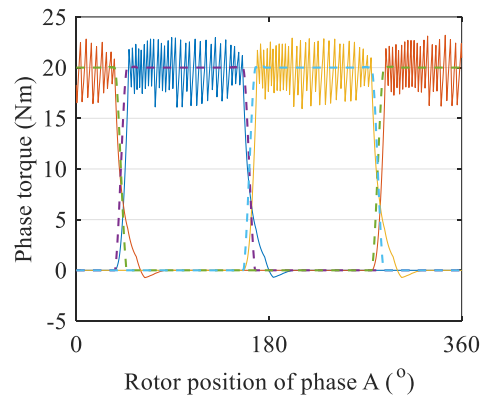
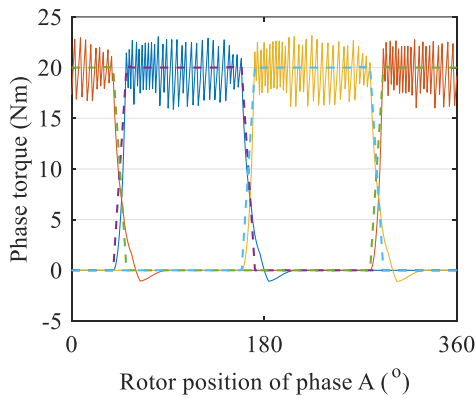
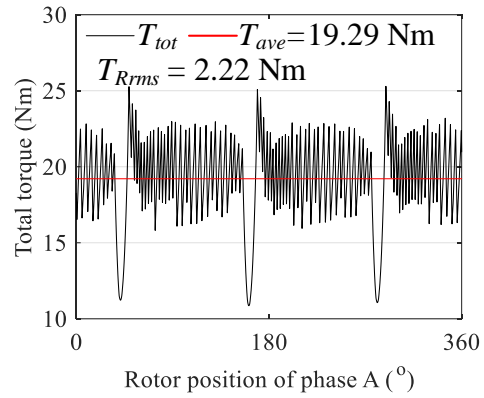
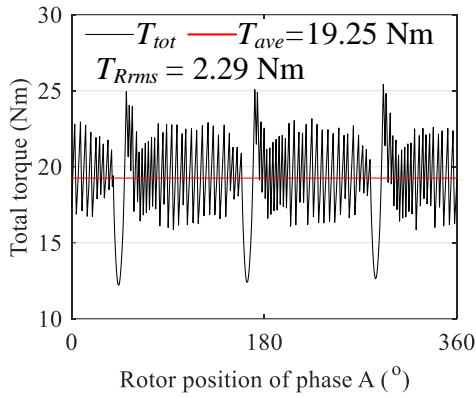
Fig. 5.11. Measured characteristics of the adopted SRM.

In order to provide a fair comparison, a multi-objective GA is used to minimize  $T_{Rrms}$  and  $I_{rms}$  for all the TSFs:

- (i)  $\theta_{on}$  and overlapping angle  $\theta_{ov}$  are optimized for the conventional TSFs.
- (ii) The weight parameter  $\sigma$  is optimized for the TSF in [41].
- (iii)  $\theta_{on}$  and  $\theta_{off}$  angles are optimized for the proposed TSF.

Fig. 5.12 shows the dynamic simulation results at 400 r/min and 20 Nm torque command. It can be observed that the TSF in [41] exhibits better performance ( $T_{ave} = 19.44$  Nm,  $T_{Rrms} = 1.75$  Nm) compared to the conventional TSFs ( $T_{ave} = 19.25$  Nm to 19.29 Nm,  $T_{Rrms} = 2.29$  Nm to 2.22 Nm). The proposed TSF exhibits the smallest torque ripple ( $T_{Rrms} = 1.52$  Nm) and the largest average torque ( $T_{ave} = 19.73$  Nm) compared to all other TSFs. As shown in Fig. 5.12(d), the proposed TSF shows almost no current tracking error. This is because the proposed TSF takes the current dynamics into account. Some current tracking error can be observed in Fig. 5.12(a) and Fig. 5.12(b) for the linear and cubic TSFs, and in Fig. 5.12(c) for the TSF in [41]. The error is relatively small because the induced voltage is low at 400 r/min. This enables a faster rate-of-change-of current and, hence, the lack of consideration of current dynamics does not have a significant impact.

— Phase A response    — Phase B response    — Phase C response  
- - - Phase A reference    - - - Phase B reference    - - - Phase C reference



(a)

(b)

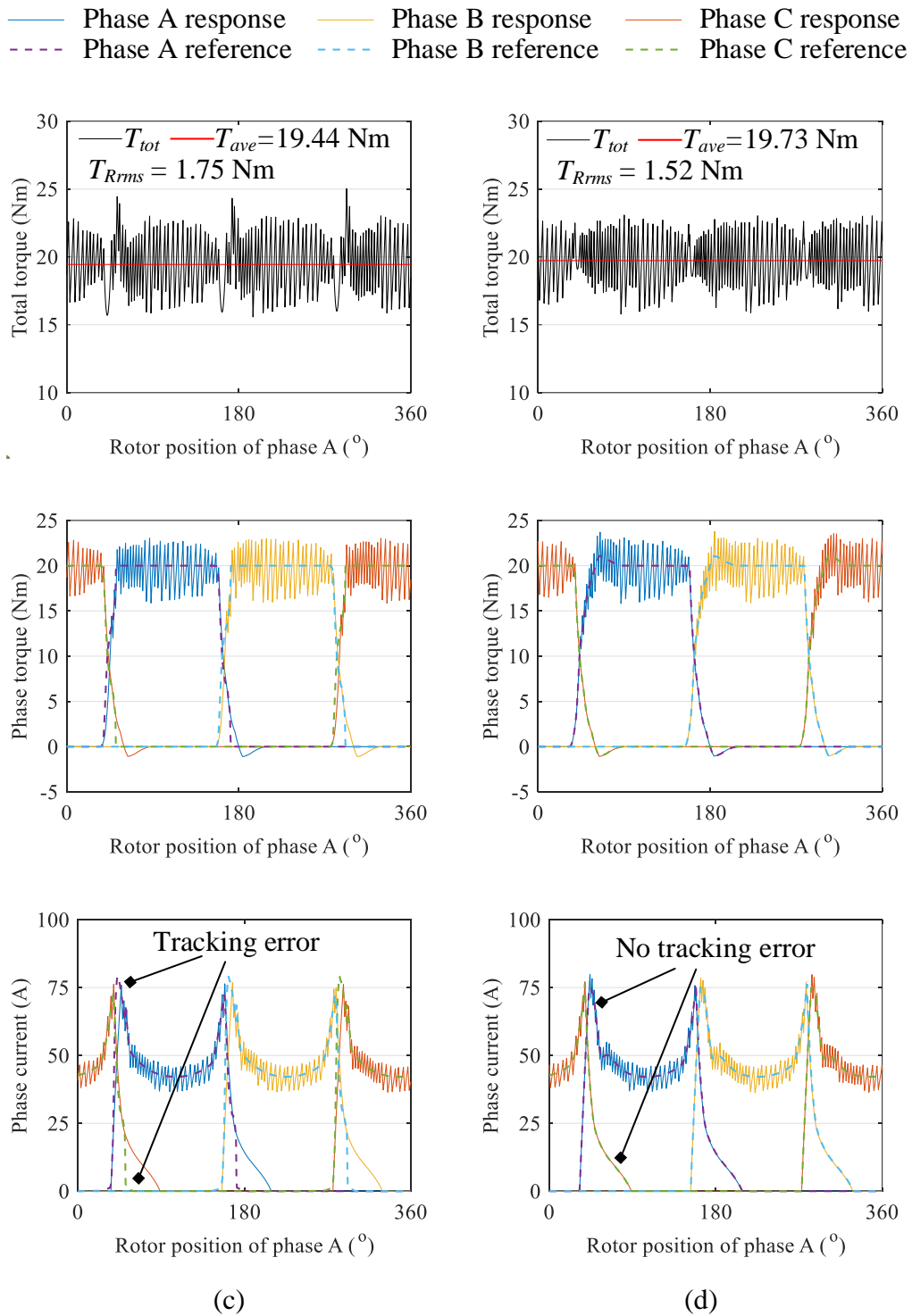
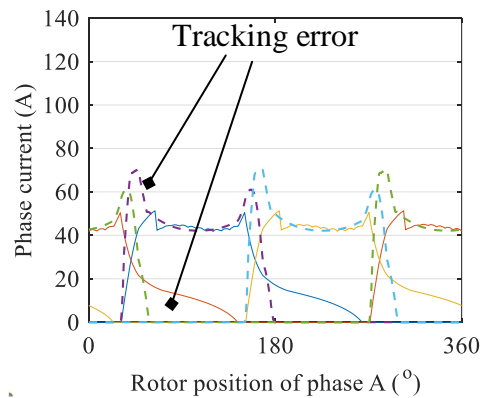
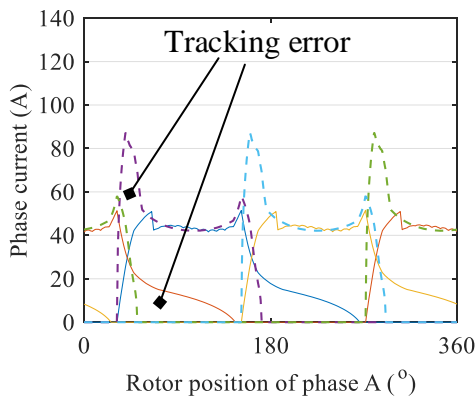
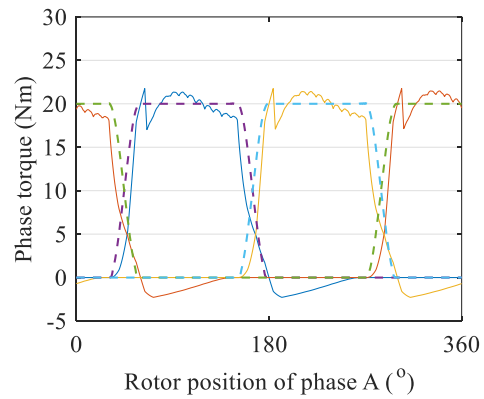
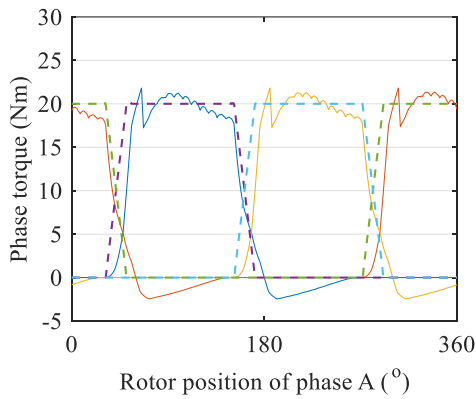
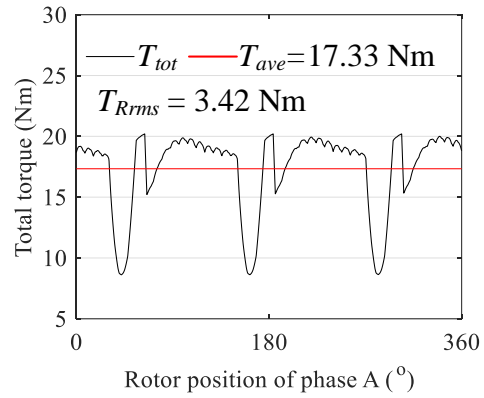
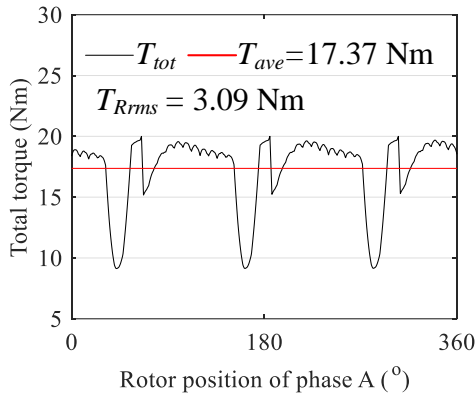


Fig. 5.12. Dynamic simulation results (Speed = 400 r/min,  $T_{ref} = 20$  Nm). (a). Linear TSF. (b) Cubic TSF. (c). TSF in [41]. (d). Proposed TSF.

The advantage of the proposed TSF becomes more obvious at the higher speed operation. Fig. 5.13 shows the dynamic simulation results at 1000 r/min and 20 Nm torque command. It can be observed that larger average torque and smaller torque ripple is achieved with the proposed TSF ( $T_{ave} = 20.02$  Nm,  $T_{Rms} = 1.00$  Nm), compared to the conventional TSFs ( $T_{ave} = 17.33$  Nm to 17.37 Nm,  $T_{Rms} = 3.09$  Nm to 3.42 Nm) and the TSF in [41] ( $T_{ave} = 19.15$  Nm,  $T_{Rms} = 3.02$  Nm). For the conventional TSFs, although  $\theta_{on}$  and  $\theta_{ov}$  are optimized, the precision of these functions, which approximate the torque waveform, is still limited because there is no theoretical relationship between these mathematical expressions and the motor characteristics. For the TSF in [41], although  $\sigma$  is used to penalize the outgoing phase current reference and increase the incoming phase current reference, the current dynamics are not considered. Thus, rise time for the incoming phase current and fall time for the outgoing phase current are insufficient. This leads to higher current tracking errors both in the incoming and outgoing phases. The proposed TSF still shows almost no current tracking error, because it considers the current dynamics.

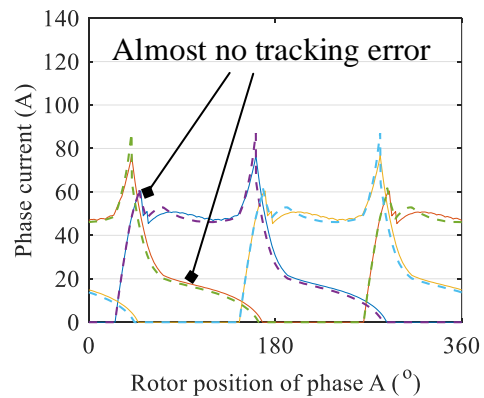
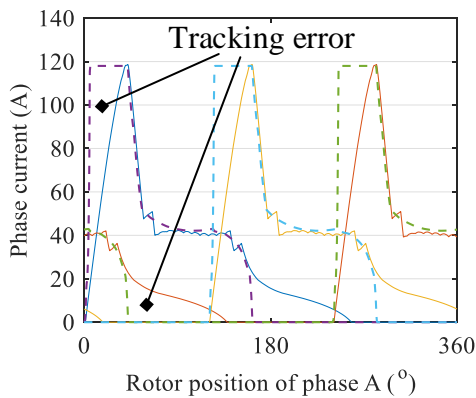
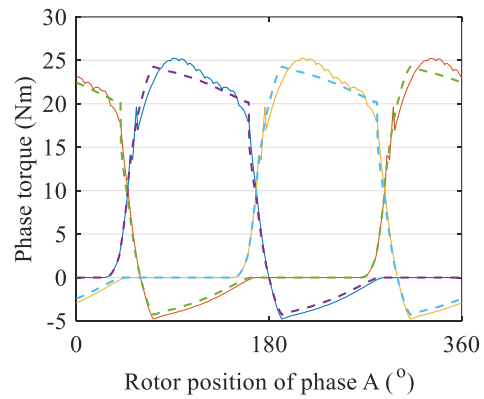
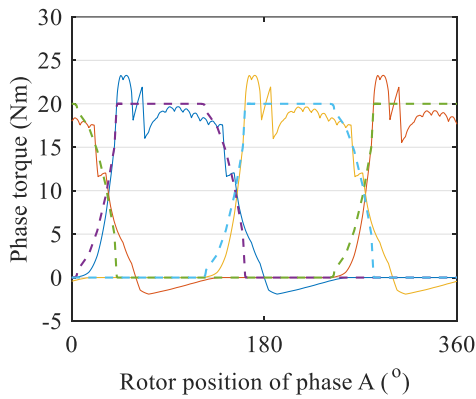
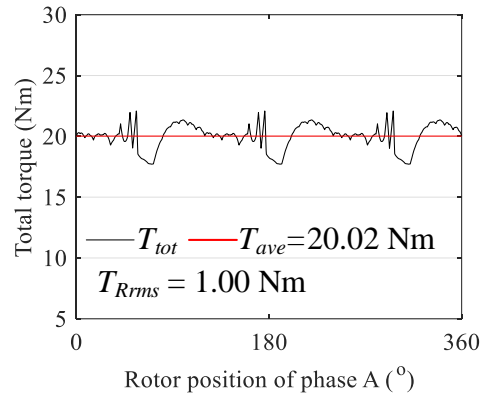
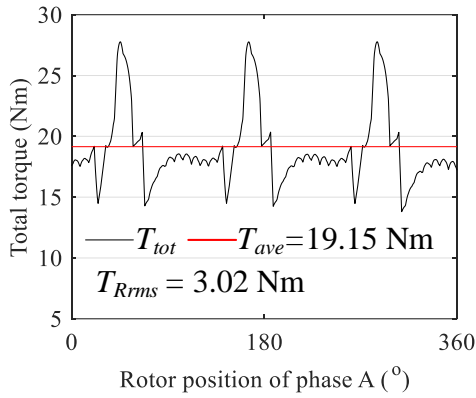
— Phase A response    — Phase B response    — Phase C response  
- - - Phase A reference    - - - Phase B reference    - - - Phase C reference



(a)

(b)

— Phase A response    — Phase B response    — Phase C response  
- - - Phase A reference    - - - Phase B reference    - - - Phase C reference



(c)

(d)

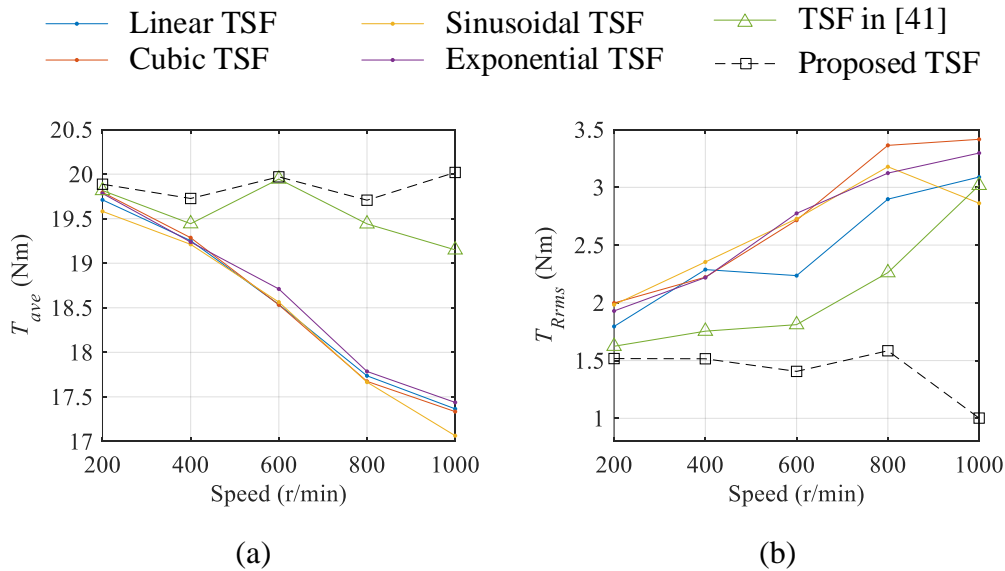
Fig. 5.13. Dynamic simulation results (Speed = 1000 r/min,  $T_{ref} = 20$  Nm). (a).

Linear TSF. (b) Cubic TSF. (c). TSF in [41]. (d). Proposed TSF.

Fig. 5.14 shows a quantitative comparison among the analyzed conventional TSFs, TSF in [41] and the proposed TSF in terms of  $T_{ave}$ ,  $T_{Rrms}$ ,  $I_{rms}$ , and torque ripple percentage  $T_{coe}$ . For the conventional TSFs, in addition to the linear and cubic TSFs, the performance of the sinusoidal and exponential TSFs are also shown in Fig. 5.14. The torque ripple percentage is defined as

$$T_{coe} = \frac{T_{max} - T_{min}}{T_{ave}} \times 100\% \quad (5.26)$$

where  $T_{max}$  and  $T_{min}$  are the maximum and minimum torque values, respectively. The torque command is 20 Nm, and the operating speed is varied from a low speed (200 r/min) to the rated speed (1000 r/min). It can be observed from Fig. 5.14 that the proposed TSF provides the highest  $T_{ave}$ , and lowest  $T_{Rrms}$  and  $T_{coe}$  from 200 r/min to 1000 r/min.



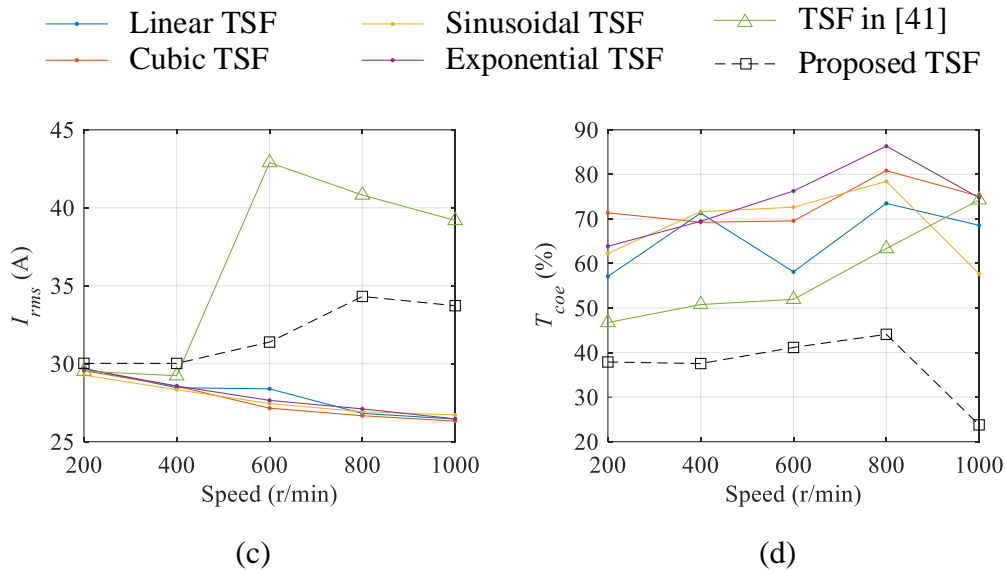
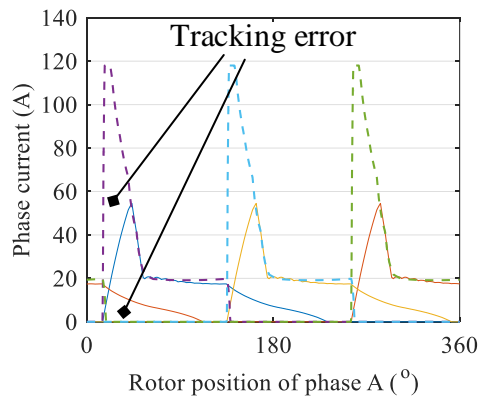
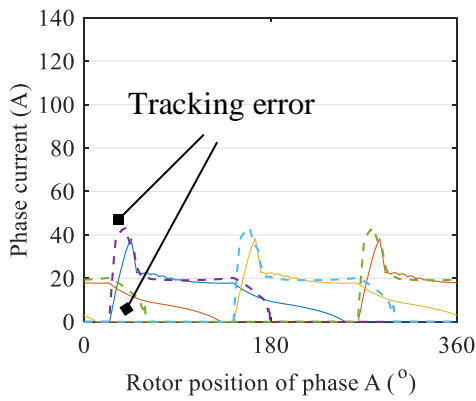
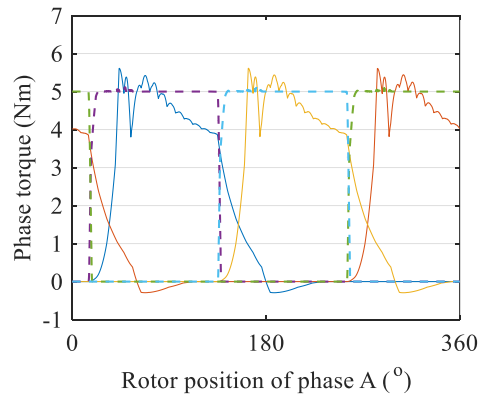
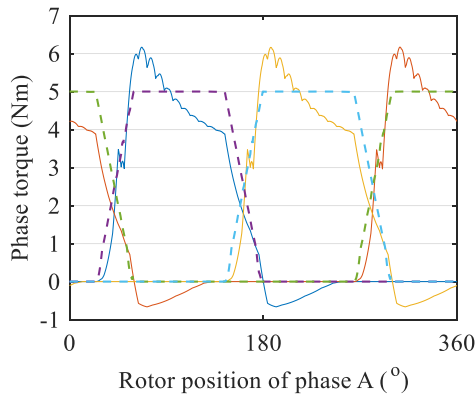
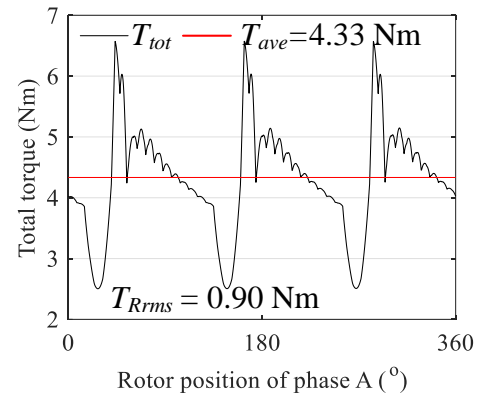
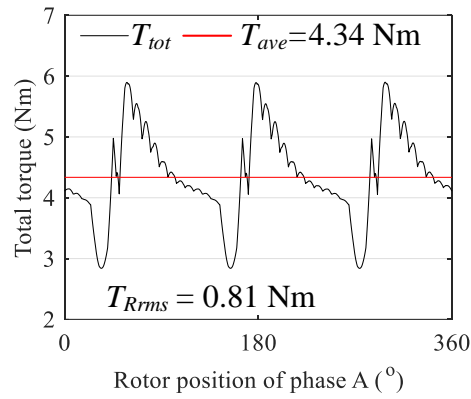


Fig. 5.14. Quantitative comparison among the conventional TSFs, TSF in [41] and the proposed TSF. (a) Average torque. (b). RMS torque ripple. (c). RMS phase current. (d). Torque ripple percentage.

Fig. 5.15 show the dynamic simulation results at 1500 r/min and 5 Nm torque command. It can be observed that larger average torque is achieved by the proposed TSF with smaller torque ripple ( $T_{ave} = 4.86$  Nm,  $T_{Rrms} = 0.51$  Nm), compared to the conventional TSFs ( $T_{ave} = 4.33$  Nm to 4.34 Nm,  $T_{Rrms} = 0.81$  Nm to 0.90 Nm) and the TSF in [41] ( $T_{ave} = 4.70$  Nm,  $T_{Rrms} = 0.77$  Nm). It should be noted that 1500 r/min is beyond the base speed of this SRM (1000 r/min), and it becomes harder to control the phase current at this speed with the rated DC link voltage due to the higher induced voltage. Because the proposed TSF considers the current dynamics in the optimization, it still shows better current tracking capability and torque performance.

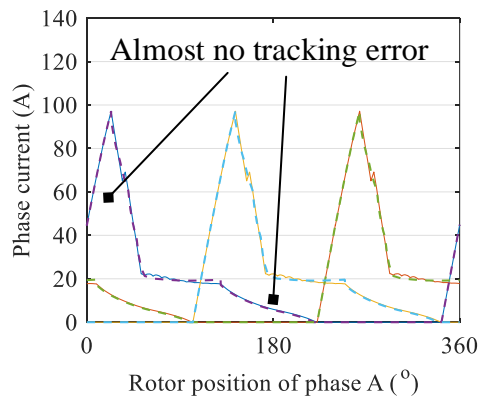
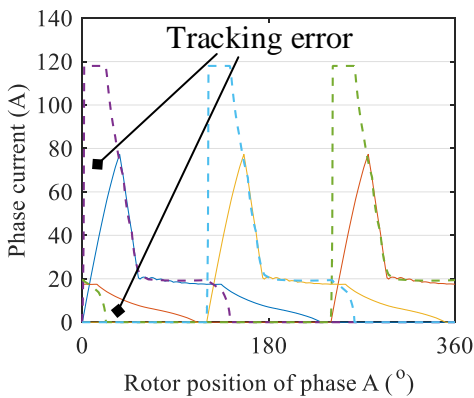
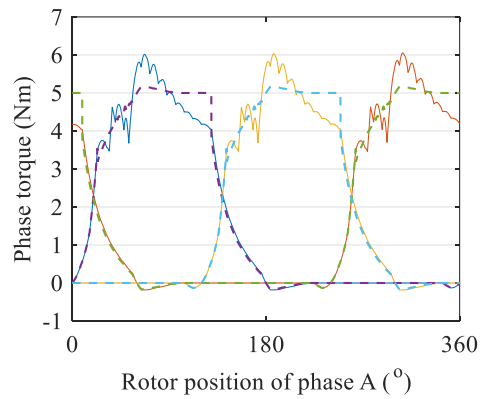
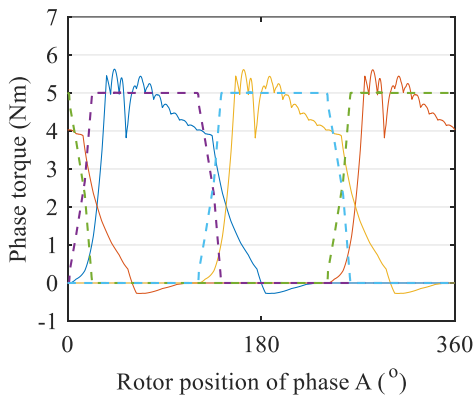
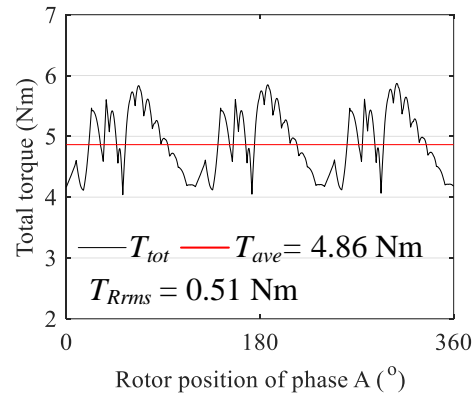
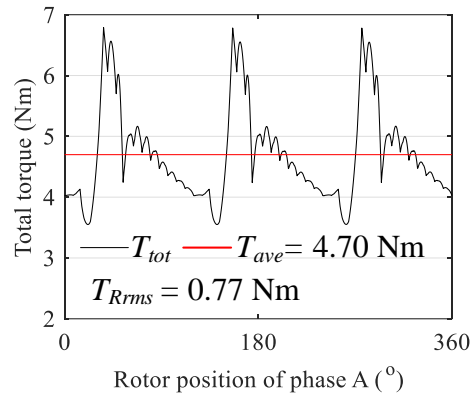
— Phase A response    — Phase B response    — Phase C response  
- - - Phase A reference    - - - Phase B reference    - - - Phase C reference



(a)

(b)

— Phase A response    — Phase B response    — Phase C response  
 - - - Phase A reference    - - - Phase B reference    - - - Phase C reference



(c)

(d)

Fig. 5.15. Dynamic simulation results (Speed = 1500 r/min,  $T_{ref} = 5$  Nm). (a). Linear TSF. (b) Cubic TSF. (c). TSF in [41]. (d). Proposed TSF.

It should be also noted that the proposed TSF considers the torque produced in all portions of the phase inductance characteristics. As shown in Fig. 5.8(e),  $\theta_{on}$  can be advanced beyond the  $0^\circ$ .  $\theta_{off}$  is smaller than  $180^\circ$ , but  $\theta_{zero}$  can be larger than  $180^\circ$ . Phase overlap is also allowed in the proposed TSF. The measured SRM characteristics are used to generate the current references and to build the dynamic SRM model. Thus, the nonlinearity of the SRM is considered in the proposed TSF.

## 5.5 Experimental Validation

In order to validate the proposed TSF, experiments were performed on the same 3-phase 12/8 SRM. Fig. 5.16 shows a picture of the experimental setup. The SRM is connected to an induction machine (IM) dynamometer. A closed-loop speed control is applied to the IM. The SRM drive is built with a Texas Instrument digital signal processor (DSP) TMS320F28335 and IGBT module F4-250R17MP4 from Infineon. The current references are stored as LUTs in the controller. The current sampling frequency and the current control hysteresis band are 40 kHz and 6 A, respectively, which were also the parameters defined in the simulations. The dc-link voltage is set as 72 V. Due to the lower bandwidth of the torque transducer (NCTE Series 3000), it was limited to observe the torque waveform in each electrical cycle. Thus, the phase torque waveforms shown are estimated using the measured phase current and rotor position in the  $T-i-\theta$  LuT, and the total torque is the sum of the estimated phase torque waveforms.

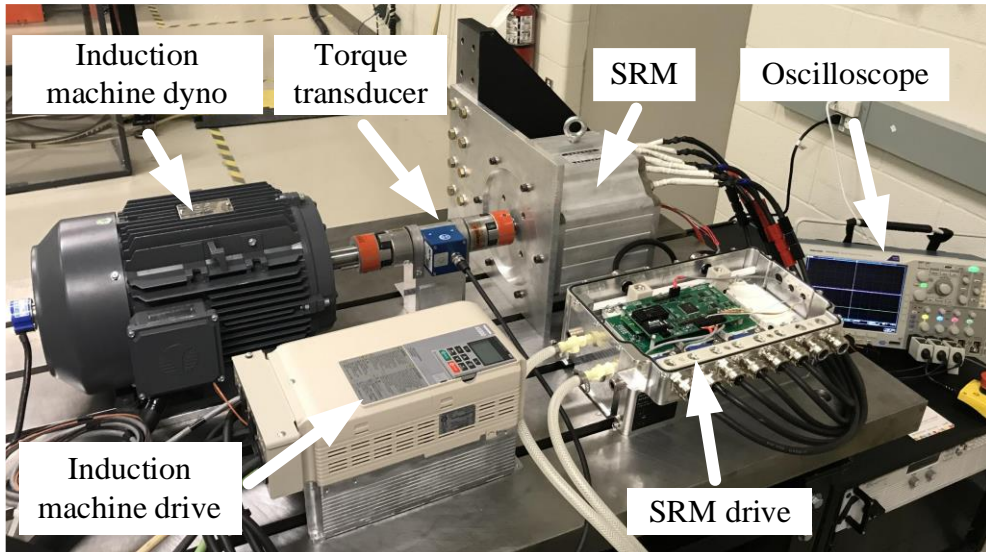
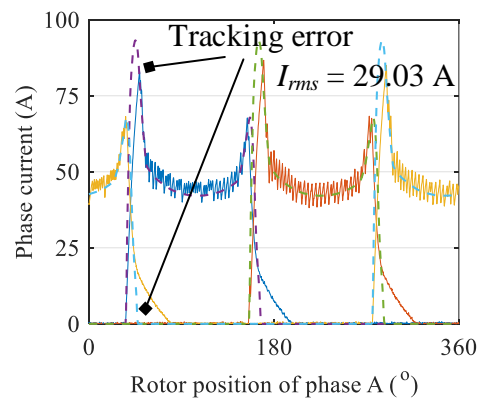
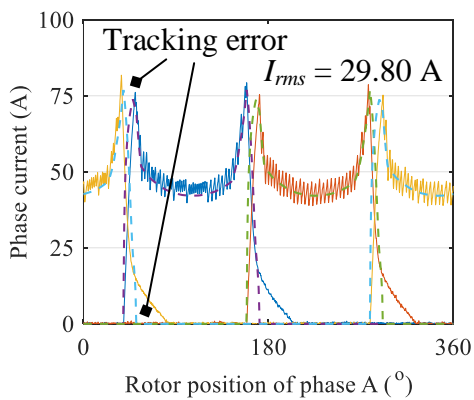
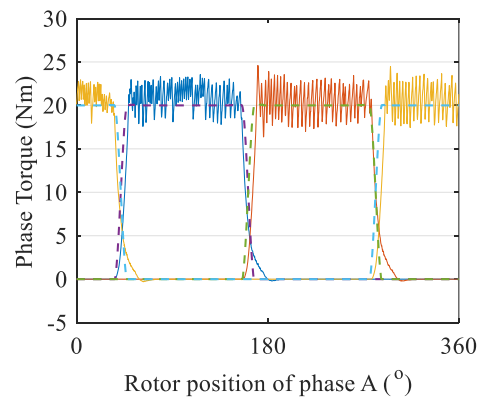
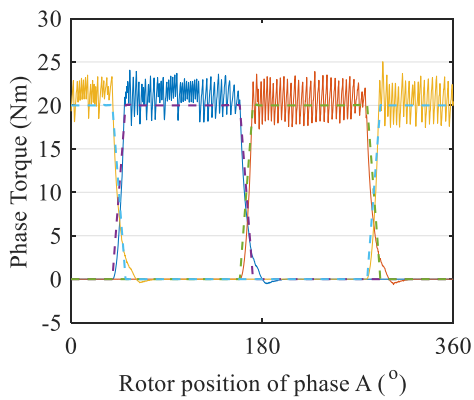
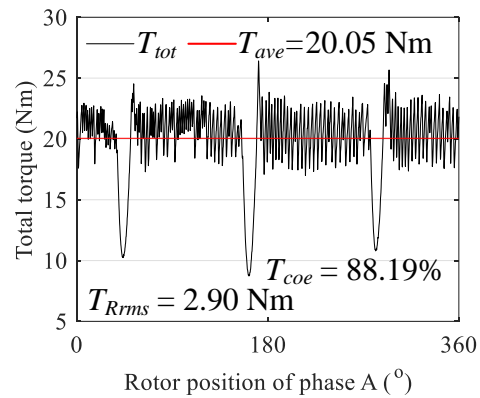
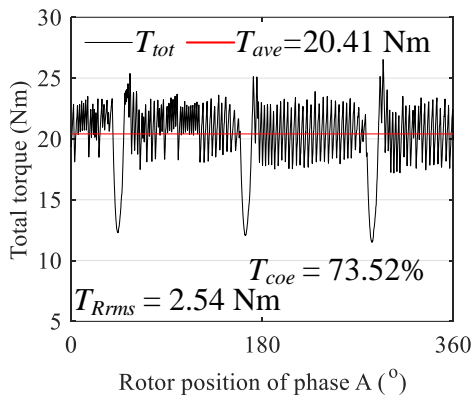


Fig. 5.16. The picture of the experimental setup.

The experimental results at 400 r/min and 20 Nm torque reference are shown in Fig. 5.17. For the conventional TSFs and the TSF in [41], similar to the simulation results in Fig. 5.12, some current tracking error can be observed in Fig. 5.17(a), (b), and (c), which increases torque ripple, especially in the overlapping region. The proposed TSF in Fig. 5.17(d) shows better current tracking performance and less torque ripple. This is because the proposed TSF takes the current dynamics into account. In Fig. 5.17(d), a small current tracking error exists with the proposed TSF. The proposed method generates the current reference based on the dynamic model of the SRM, which is built using the measured SRM characteristics. The error in the experimental characterization of the reference SRM might be the reason of the small tracking error.

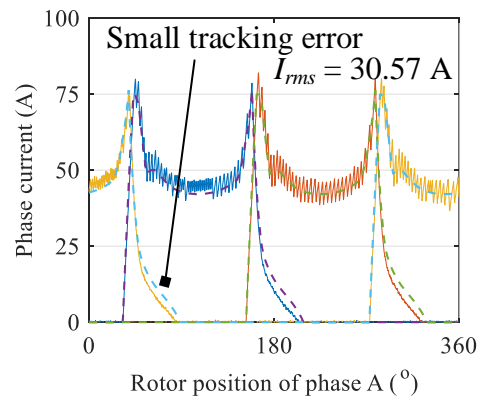
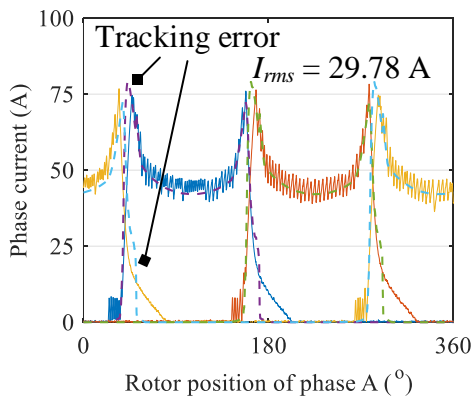
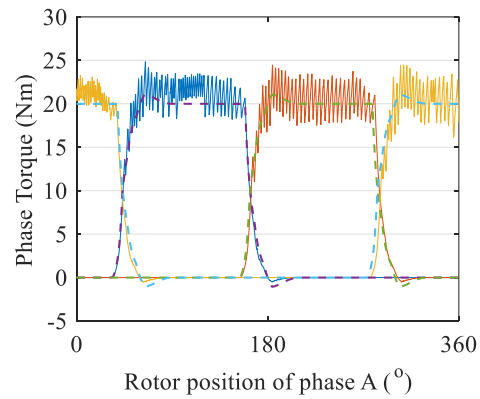
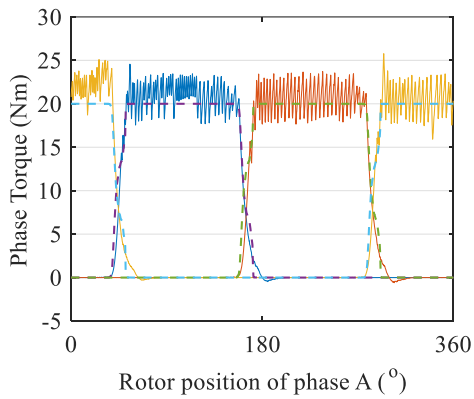
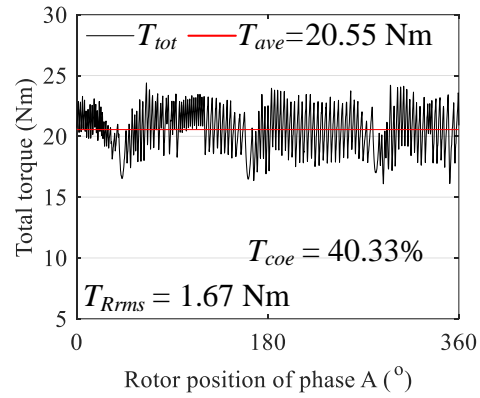
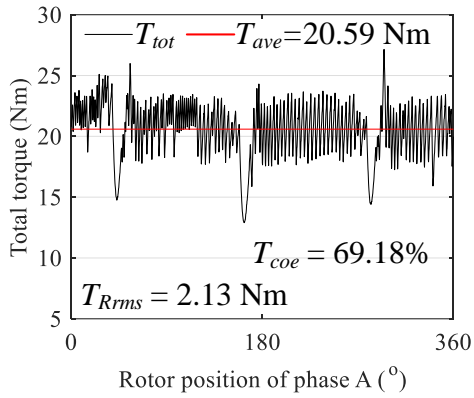
— Phase A response    — Phase B response    — Phase C response  
- - - Phase A reference    - - - Phase B reference    - - - Phase C reference



(a)

(b)

— Phase A response    — Phase B response    — Phase C response  
 - - - Phase A reference    - - - Phase B reference    - - - Phase C reference



(c)

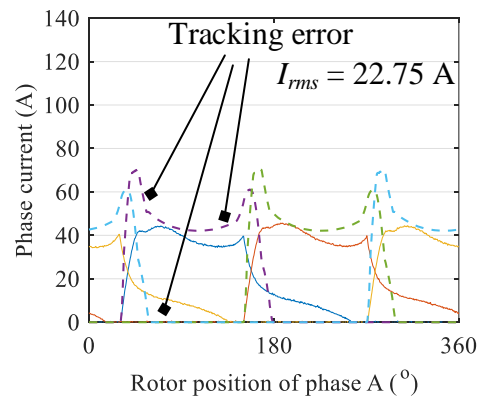
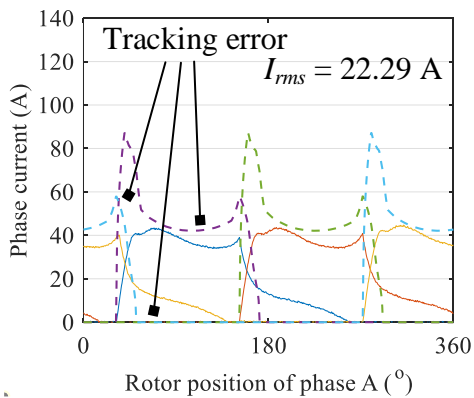
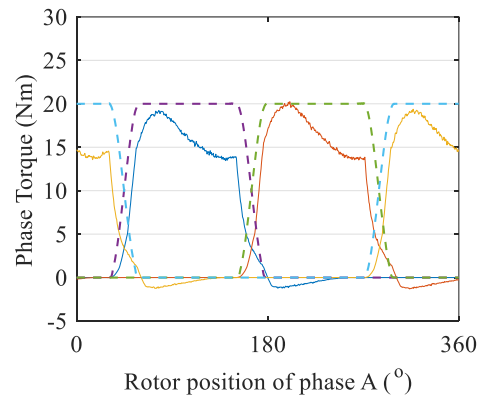
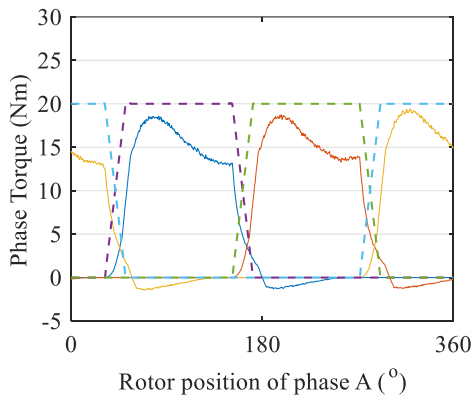
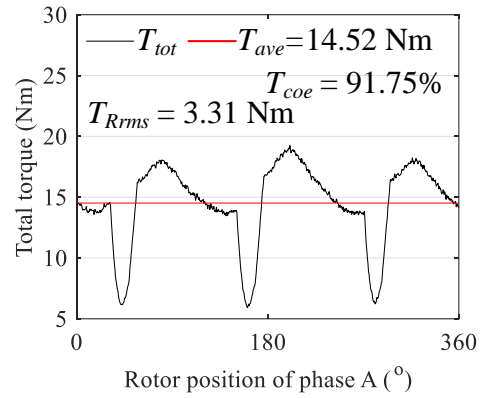
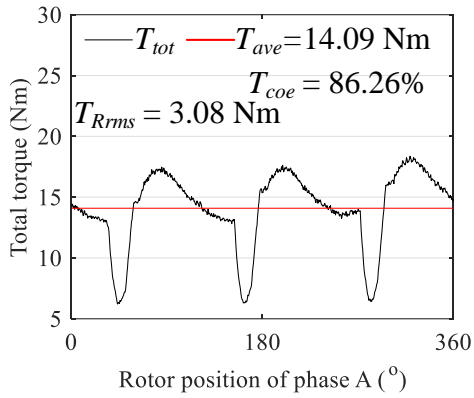
(d)

Fig. 5.17. Experimental results (Speed = 400 r/min,  $T_{ref} = 20$  Nm). (a). Linear TSF.

(b) Cubic TSF. (c). TSF in [41]. (d). Proposed TSF.

The experimental results at 1000 r/min and 20 Nm torque reference, and 1500 r/min and 5 Nm are shown in Fig. 5.18 and Fig. 5.19, respectively. The conventional TSFs provide low average torque and high torque ripple, due to the lack of consideration of machine dynamics. The TSF in [41] shows better performance compared to the conventional TSFs, which is due to its induced EMF constraint expressed in (5.14). However, because of the insufficient rise time for the incoming phase current and insufficient fall time for the outgoing phase current, the conventional TSFs and the TSF in [41] still shows larger current tracking error and higher torque ripple compared to the results of the proposed TSF. The minor current tracking error in Fig. 5.18(d) and Fig. 5.19(d) for the proposed TSF is also due to the possible error in the experimental characterization of the SRM.

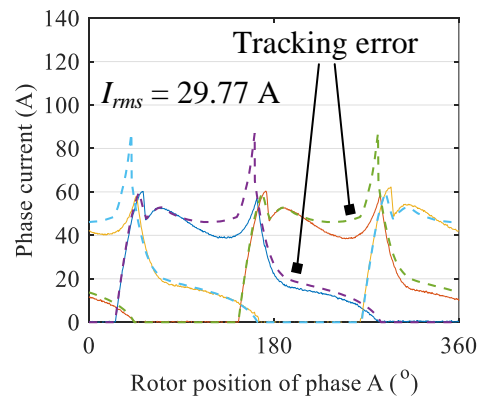
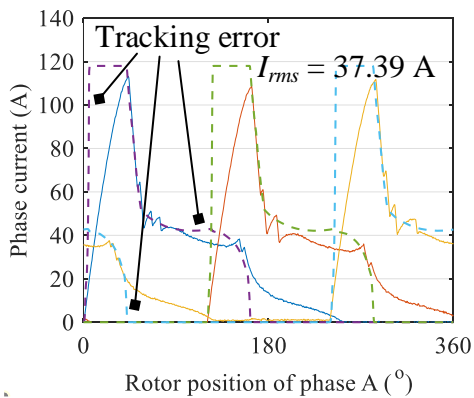
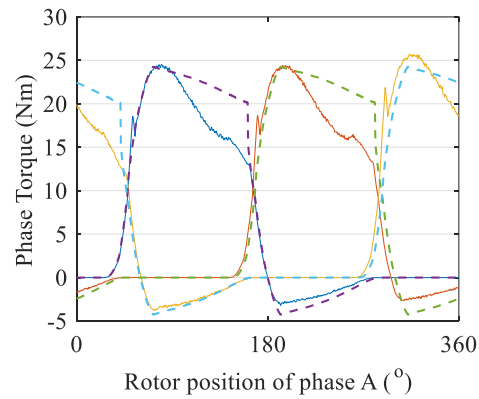
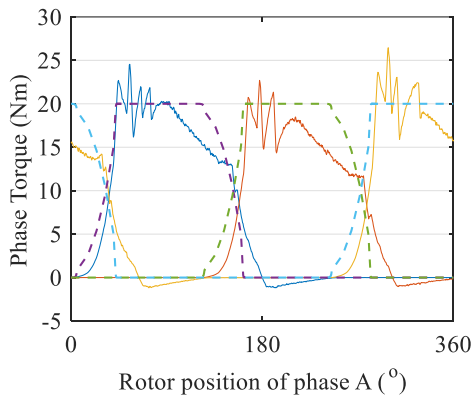
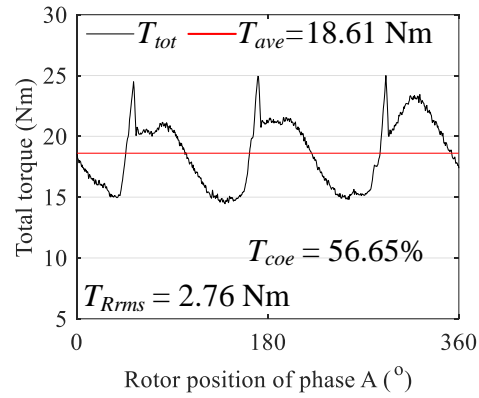
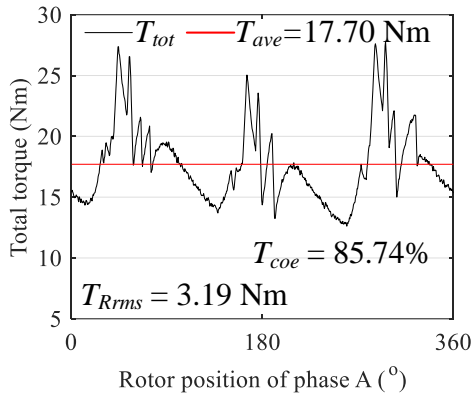
— Phase A response    — Phase B response    — Phase C response  
- - - Phase A reference    - - - Phase B reference    - - - Phase C reference



(a)

(b)

— Phase A response    — Phase B response    — Phase C response  
 - - - Phase A reference    - - - Phase B reference    - - - Phase C reference



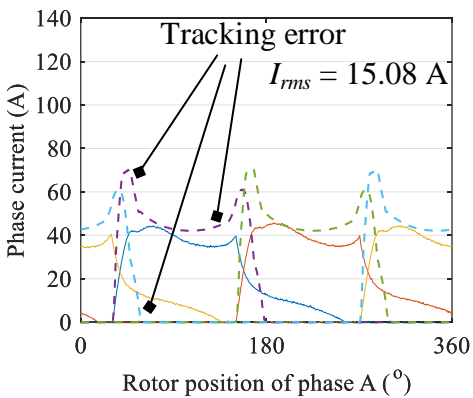
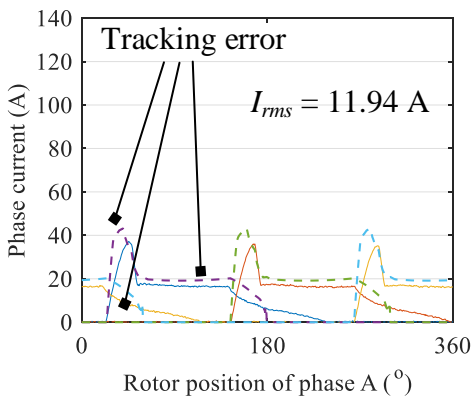
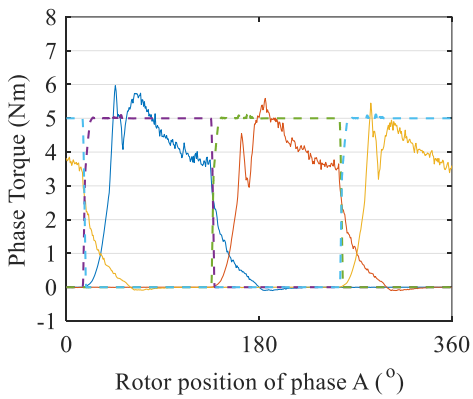
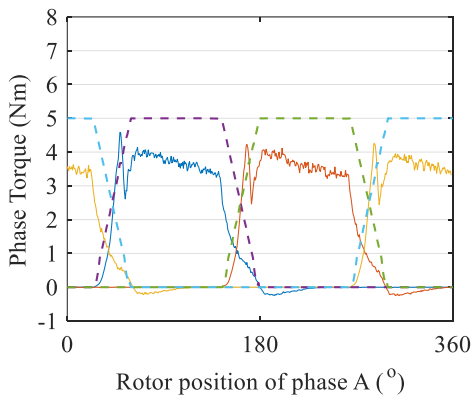
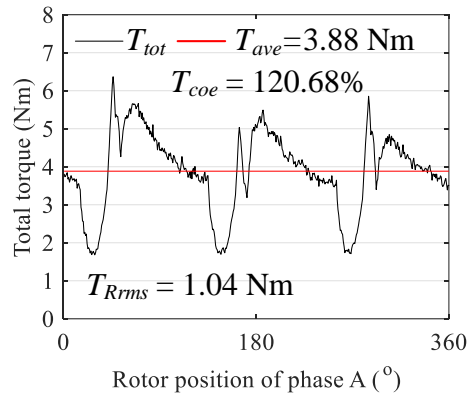
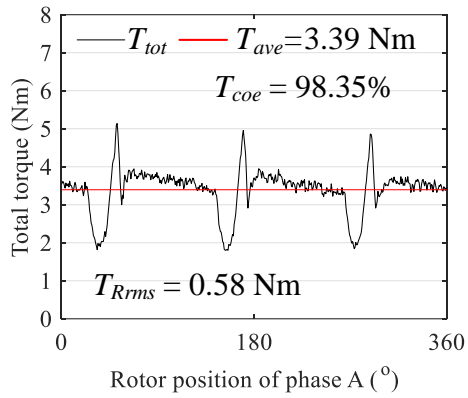
(c)

(d)

Fig. 5.18. Experimental results (Speed = 1000 r/min,  $T_{ref} = 20$  Nm). (a). Linear TSF.

(b) Cubic TSF. (c). TSF in [41]. (d). Proposed TSF.

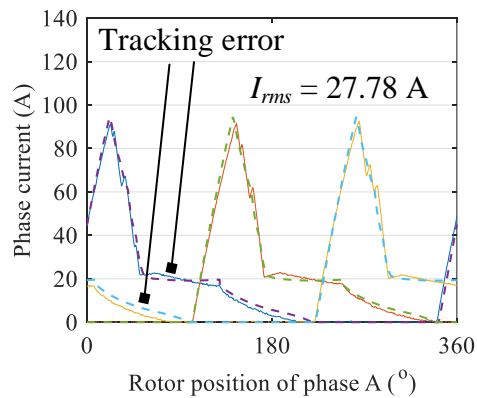
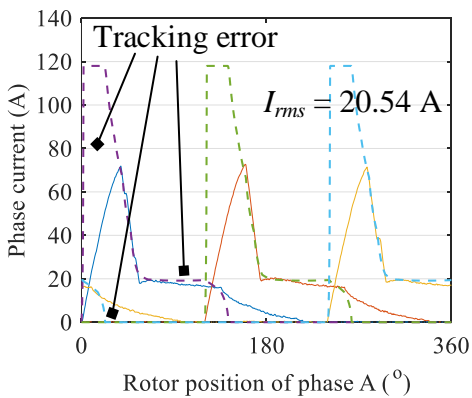
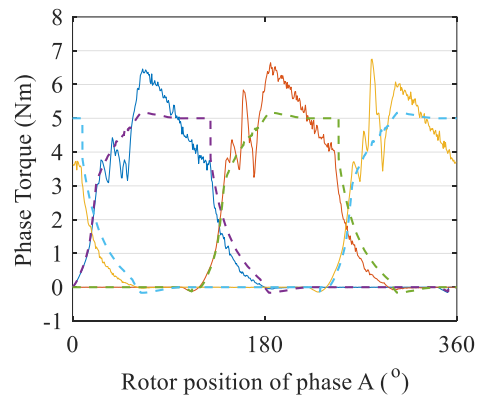
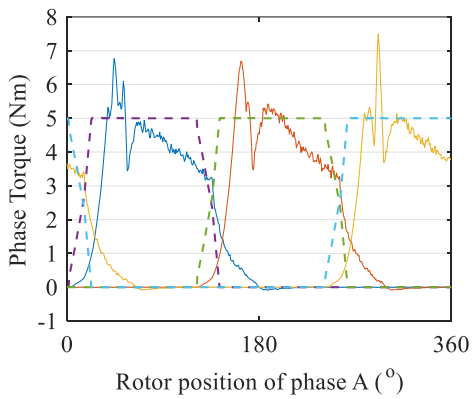
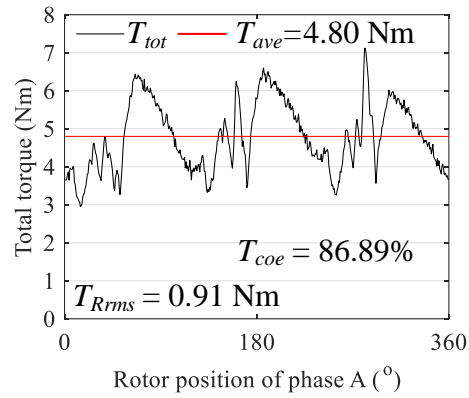
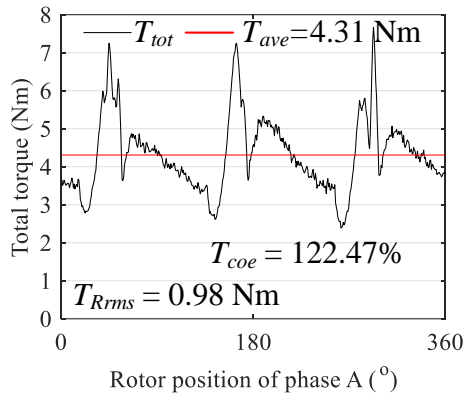
— Phase A response    — Phase B response    — Phase C response  
 - - - Phase A reference    - - - Phase B reference    - - - Phase C reference



(a)

(b)

— Phase A response    — Phase B response    — Phase C response  
 - - - Phase A reference    - - - Phase B reference    - - - Phase C reference



(c)

(d)

Fig. 5.19. Experimental results (Speed = 1500 r/min,  $T_{ref} = 5$  Nm). (a). Linear TSF.

(b) Cubic TSF. (c). TSF in [41]. (d). Proposed TSF.

## 5.6 Conclusion

In this chapter, a new offline TSF for torque ripple reduction in switched reluctance machines is proposed. Lower current tracking error is achieved by a new current reference generation strategy and optimization, which takes the current dynamics into account. In the proposed TSF, the phase current reference is first derived from the torque command using offline calculations and also from the phase current response. Then, an optimization problem is formulated to shape the current reference to minimize the torque ripple and copper losses, while maintaining the required average output torque. The simulation results and experimental validation show that the proposed TSF shows better performance with higher average torque and lower torque ripple.

## **Chapter 6**

# **An Online Torque Sharing Function Involving Current Dynamics for Switched Reluctance Motor Drives**

### **6.1 Introduction**

Switched reluctance machine is a promising alternative to other conventional dc or ac machines in a wide variety of applications. However, high torque ripple is one of the major drawbacks of SRM that limits its widespread use in these applications. This chapter proposes a novel online torque sharing function for torque ripple reduction in switched reluctance machines. The induced voltage and phase current dynamics of SRM are first analyzed. Then the proposed online current reference

generation strategy and adaptive turn-on angle adjustment strategy are stated. The optimization process is decoupled to independently minimize the torque ripple by optimizing the turn-on angle and minimizing copper losses by optimizing the turn-off angle. Finally, the performance of the proposed TSF is compared with the conventional TSFs and existing optimization-based TSFs through both simulations and experiments. The impact of the parameter variations is also discussed.

## 6.2 Induced EMF and Current Dynamics

The doubly salient structure of SRMs results in high saliency, which can increase the complexity of the current control. If the mutual coupling is neglected, the phase voltage equation of an SRM is expressed as

$$V = Ri + \frac{d\lambda(\theta, i)}{dt} = Ri + L(\theta) \frac{\partial i}{\partial t} + \varepsilon(i, \theta, \omega) \quad (6.1)$$

$$\varepsilon(i, \theta, \omega) = i \frac{\partial L(\theta)}{\partial \theta} \omega \quad (6.2)$$

where  $V$ ,  $i$ , and  $R$  represent the phase voltage, phase current, and phase resistance, respectively.  $\lambda$ ,  $L$ ,  $\theta$ ,  $t$ , and  $\omega$  denote the flux linkage, inductance, rotor position, time interval, and angular speed, respectively.  $\varepsilon$  is the induced EMF, as expressed in (6.2). By rearranging (6.1), the rate-of-change-of the phase current of an SRM can be derived as

$$\frac{\partial i}{\partial t} = \frac{V - \varepsilon(i, \theta, \omega) - Ri}{L(\theta)}. \quad (6.3)$$

From (6.3), it can be concluded that the phase current dynamics are highly nonlinear as they are related to the voltage, inductance, induced EMF, resistance, rotor position, and the current itself.

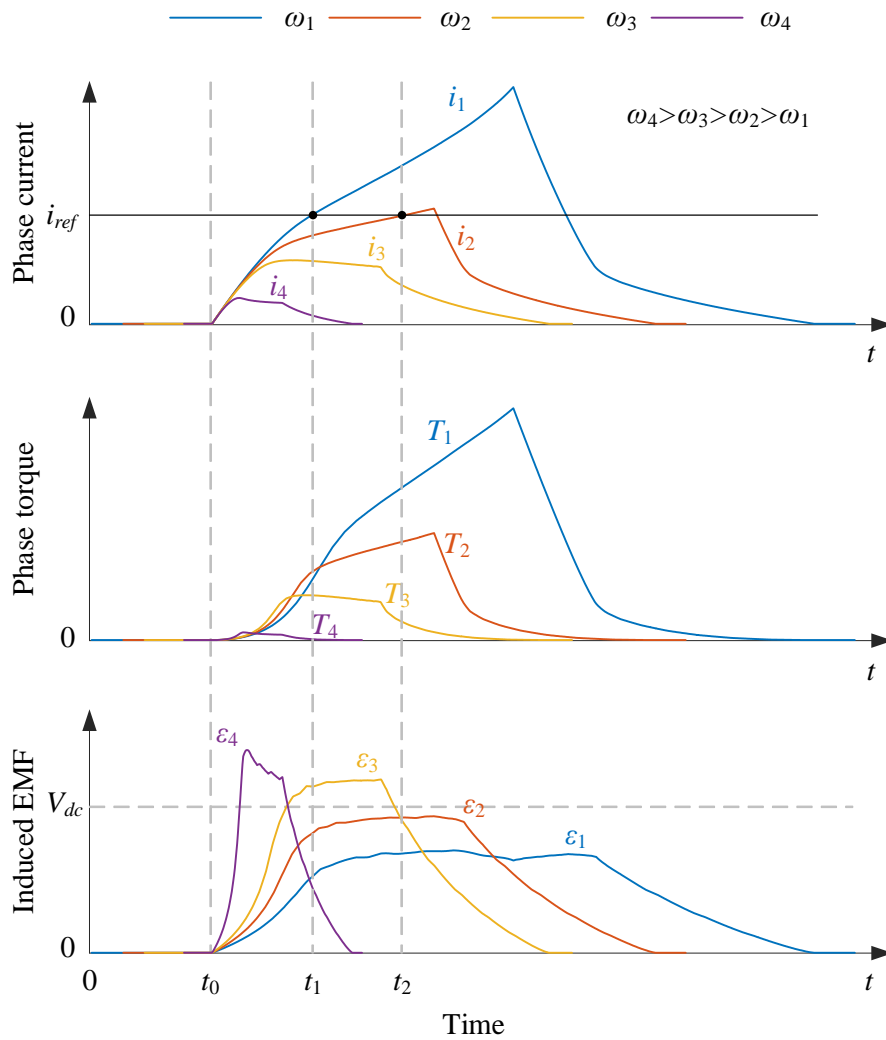


Fig. 6.1. Dynamic profiles of the phase current, torque, and induced EMF under different operating speeds and the same conduction angles.

Fig. 6.1 shows the dynamic current, torque, and induced EMF profiles using (6.3) for single-pulse voltage control. The phase resistance is neglected in (6.3) for simplification. The same turn-on and turn-off angles are applied under four different speeds, where  $\omega_4 > \omega_3 > \omega_2 > \omega_1$ . It can be observed that the induced EMF increases with speed, and it prevents the current from rising when it is higher than the dc-link voltage,  $V_{dc}$ . Thus, lower peak current is obtained at  $\omega_3$  and  $\omega_4$ . This reduces the output torque, compared to the other two cases at  $\omega_1$  and  $\omega_2$ . If the induced EMF is considered, the torque-speed capability of the motor drive could be improved as compared to conventional TSFs [41], [54], [55]. For example, in [41], the induced EMF was used as a constraint in the optimization. As long as the induced EMF was less than the dc-link voltage, the current reference was deemed trackable. However, this is true only when the rate of change of current is ignored and enough tracking time for the phase current is provided. Otherwise, current tracking error may still occur due to the insufficient rise or fall time for the phase current, which may increase the torque ripple. For example, as shown in Fig. 6.1, induced EMFs both at  $\omega_1$  and  $\omega_2$  are lower than  $V_{dc}$ . However, it takes  $t_1$  for  $i_1$  and  $t_2$  for  $i_2$  to reach to the current reference,  $i_{ref}$ . If only  $t_1$  is provided as the rise time for the phase current, some current tracking error will be observed for  $i_2$ . Similarly, the assumption in [54] and [55] that the tracking error of the phase with the lower absolute values of the rate of change of flux linkage (ARCFL) being zero is based on the assumption that the current dynamics are ignored.

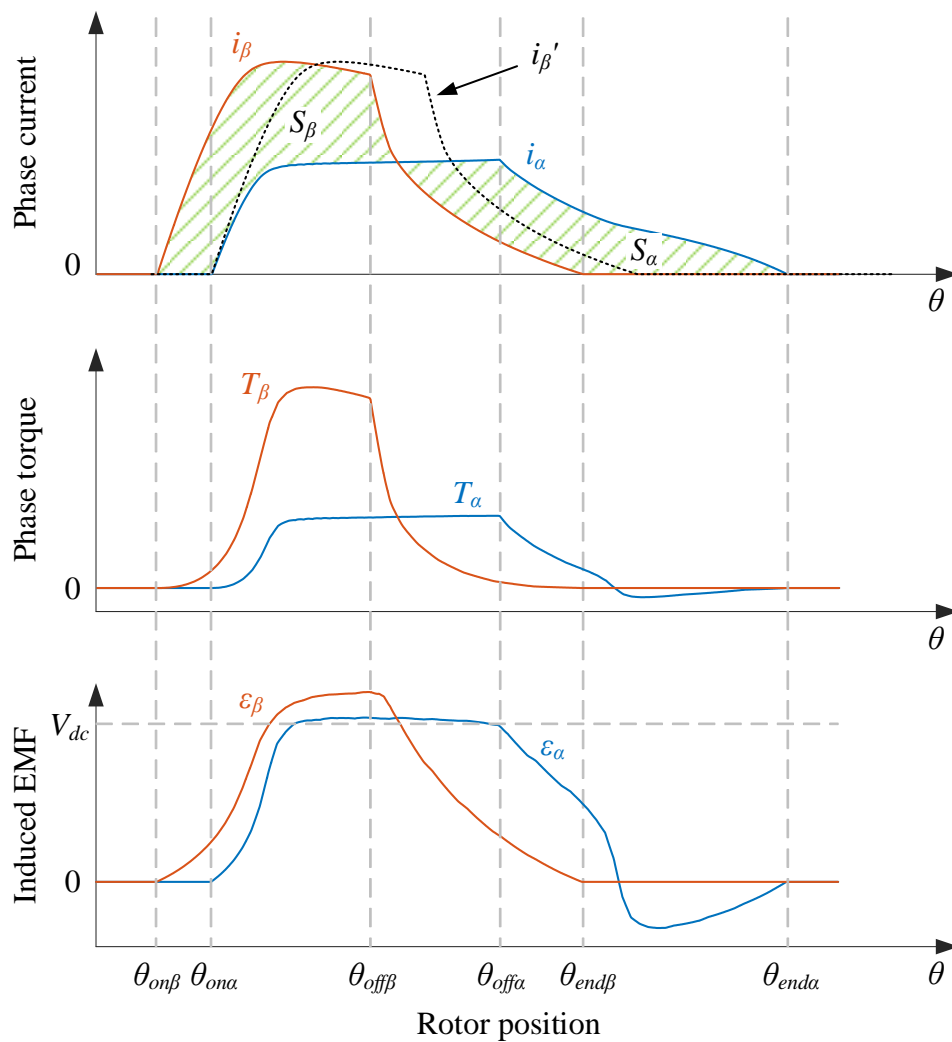


Fig. 6.2. Dynamic profiles of the phase current, torque, and induced EMF with different firing angles at the same operating speed.

Fig. 6.2 shows the dynamic profiles of the phase current, torque, and induced EMF with different firing angles at the same operating speed. Although the values of induced EMF for both cases exceed the dc-link voltage, the phase current  $i_\beta$  achieves higher peak value compared to phase current  $i_\alpha$ . This is because an

advanced turn-on angle  $\theta_{on\beta}$  is applied and the phase current increases before  $\varepsilon_\beta$  reaches to  $V_{dc}$ . This may improve the output torque. In Fig. 6.2, the shaded area  $S_\beta$  could well be less than or equal to the shaded area  $S_\alpha$ . These areas represent a portion of copper losses each current waveform would generate. This would imply that with  $i_\beta$ , the same or a lower copper loss might be achieved. Hence, the higher peak current might not always mean a higher copper loss.

At the beginning of the excitation, the values of both  $\varepsilon_\alpha$  and  $\varepsilon_\beta$  are low. However,  $i_\alpha$  and  $i_\beta$  still exhibit different current dynamics. In order to show that more clearly, the waveform for  $i_\beta$  is shifted to the same turn-on angle as  $i_\alpha$  in Fig. 6.2, which is designated as  $i_\beta'$ . The different current dynamics between  $i_\alpha$  and  $i_\beta$  at the beginning of the excitation is due to the nonlinear inductance characteristics at different rotor positions, which should also be considered in current control.

### 6.3 Proposed Online TSF

The proposed online TSF takes the current dynamics into account when generating the current reference. The flowchart for the proposed online TSF method is shown in Fig. 6.3. There are two optimization loops. A line search algorithm [114] is used to form the outer loop that determines the turn-off angle candidates for the copper loss reduction. For each turn-off angle, the inner optimization loop is executed. In the inner loop, the current reference is generated by the proposed online current profile generation technique. Then, it is updated by the proposed adaptive turn-on

angle adjustment algorithm. For each current reference, the average torque is evaluated. The inner optimization loop repeats until the turn-on angle is obtained that provides the current reference with a satisfied average torque. Then, the root-mean-square (rms) value of the phase current is calculated and returned to the outer optimization loop. The outer optimization loop repeats until the rms value of the phase current is minimized.

### 6.3.1 Outer Optimization Loop: Copper Loss Reduction

The golden section method is applied in the line search method in the outer optimization loop. As shown in Fig. 6.3, the line search method finds the optimal turn-off angle in the outer optimization loop based on the rms value of the phase current. A description for how golden section method functions is presented in [115]. In the proposed method, the golden section method is adapted to the calculation of the optimal turn-off angle.

The golden section method starts with an initial range of the turn-off angles, which contains the minimum turn-off angle,  $\theta_{offmin}$  and the maximum turn-off angle,  $\theta_{offmax}$ . At the initial step,  $[\theta_{offmin}, \theta_{offmax}]$  is defined manually, but it is updated by the golden section method in each iteration. Then, two intermediate turn-off angle candidates  $\theta_{off1}$  and  $\theta_{off2}$  are calculated using (6.4):

$$\begin{cases} \theta_{off1} = \theta_{offmin} + (1 - \rho)(\theta_{offmax} - \theta_{offmin}) \\ \theta_{off2} = \theta_{offmin} + \rho(\theta_{offmax} - \theta_{offmin}) \end{cases} \quad (6.4)$$

where  $\rho$  is the golden section ratio,  $\rho \approx 0.618$  [115]. The optimization process in the outer loop intends to shrink the range of  $[\theta_{offmin}, \theta_{offmax}]$  by comparing  $\theta_{off1}$  and  $\theta_{off2}$ , until the difference between  $\theta_{offmin}$  and  $\theta_{offmax}$  is small enough.

Once  $\theta_{off1}$  and  $\theta_{off2}$  are calculated from (6.4), they are applied to the inner optimization loop shown in Fig. 6.3, in turns. The inner optimization loop will be presented in the next section. For each candidate, the inner optimization loop repeats until the torque requirement is satisfied. Then, the rms current values  $i_{rms1}$  for  $\theta_{off1}$ , and  $i_{rms2}$  for  $\theta_{off2}$ , are calculated and compared. Based on the principle of the golden section method, if  $i_{rms2} > i_{rms1}$ , then  $\theta_{offmax}$ ,  $\theta_{off2}$ ,  $\theta_{off1}$  are updated as in (6.5). If  $i_{rms1} > i_{rms2}$ ,  $\theta_{offmin}$ ,  $\theta_{off1}$ ,  $\theta_{off2}$  are updated as in (6.6). Similarly, (6.5) and (6.6) are adapted from the golden section method [115].

$$\begin{cases} \theta_{offmax} = \theta_{off2} \\ \theta_{off2} = \theta_{off1} \\ \theta_{off1} = \theta_{offmin} + (1 - \rho)(\theta_{offmax} - \theta_{offmin}) \end{cases} \quad (6.5)$$

$$\begin{cases} \theta_{offmin} = \theta_{off1} \\ \theta_{off1} = \theta_{off2} \\ \theta_{off2} = \theta_{offmin} + \rho(\theta_{offmax} - \theta_{offmin}) \end{cases} \quad (6.6)$$

Equations (6.5) and (6.6) update the interval  $[\theta_{offmin}, \theta_{offmax}]$  and the intermediate  $\theta_{off}$  candidates. The outer optimization loop repeats until the difference between the intermediate  $\theta_{off}$  candidates ( $\theta_{off1}$  and  $\theta_{off2}$ ) is smaller than the turn-off angle tolerance  $\delta_{\theta min}$ , expressed in (6.7).

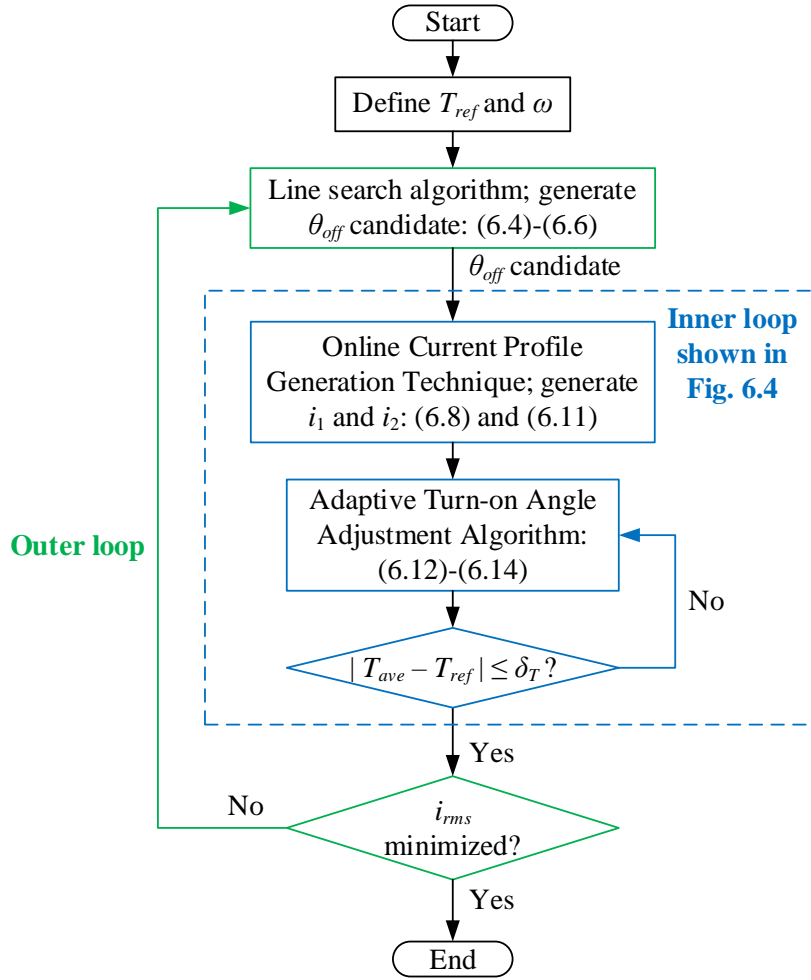


Fig. 6.3. Flowchart for the proposed online TSF.

$$\delta_{\theta_{\min}} = \omega N_r \frac{360^\circ}{2\pi f_{\text{sample}}} \quad (6.7)$$

where  $\omega$  is the rotor speed in rad/s,  $N_r$  is the number of the rotor poles, and  $f_{\text{sample}}$  is the sample frequency of the digital controller. Equation (6.7) represents the change in the electrical angle in each sampling period. A smaller tolerance might not have

an influence on the current reference due to the limited position sampling rate of the controller.

### 6.3.2 Inner Optimization Loop: Torque Ripple Reduction

Fig. 6.4 shows the block diagram of the inner optimization loop in the proposed TSF. The current reference is first generated by the proposed two-step Online Current Profile Generation Technique. Then, it is updated by the proposed Adaptive Turn-on Angle Adjustment Algorithm. The inner optimization loop repeats until the turn-on angle is obtained that provides the current reference with satisfying average torque. As shown in Fig. 6.4,  $i_1$ ,  $i_2$ , and  $i_3$  are generated in Step A, Step B, and the proposed Adaptive Turn-on Angle Adjustment Algorithm, respectively. The SRM operates using the hysteresis current control. The current reference to be tracked,  $i_{ref}$  equals to  $i_1$ ,  $i_2$ , or  $i_3$  at different stages of the inner optimization loop.

The online current profile generation of the inner optimization loop is implemented in two steps as shown in Fig. 6.4. In Step A, a primary phase current reference,  $i_1$  is derived based on the torque command,  $T_{ref}$  and the  $\theta_{off}$  candidate provided by the outer optimization loop.  $i_1$  is expressed as in (6.8), and its profile is shown in Fig. 6.5(a). Then,  $i_1$  is applied to the hysteresis current control of the SRM as  $i_{ref}$ .

$$i_1 = \begin{cases} 0, & \theta < \theta_{oni} \\ i_{LUT}(T_{ref}, \theta), & \theta_{oni} \leq \theta \leq \theta_{off} \\ 0, & \theta > \theta_{off} \end{cases} \quad (6.8)$$

where  $i_{LUT}$  is the inverse static torque characteristic ( $T-i-\theta$ ), which is stored in the digital controller as a lookup table (LUT). In  $i_{LUT}$ , the reference torque and rotor position are inputs, the phase current is the output. The initial turn-on angle,  $\theta_{oni}$  is expressed as  $\theta_{off} - \theta_{sft}$ , where  $\theta_{sft}$  is the electrical phase shift angle between the phases of SRM.  $\theta_{sft}$  is defined as in (6.9), where  $n$  is the number of phases.

$$\theta_{sft} = \frac{360^\circ}{n}. \quad (6.9)$$

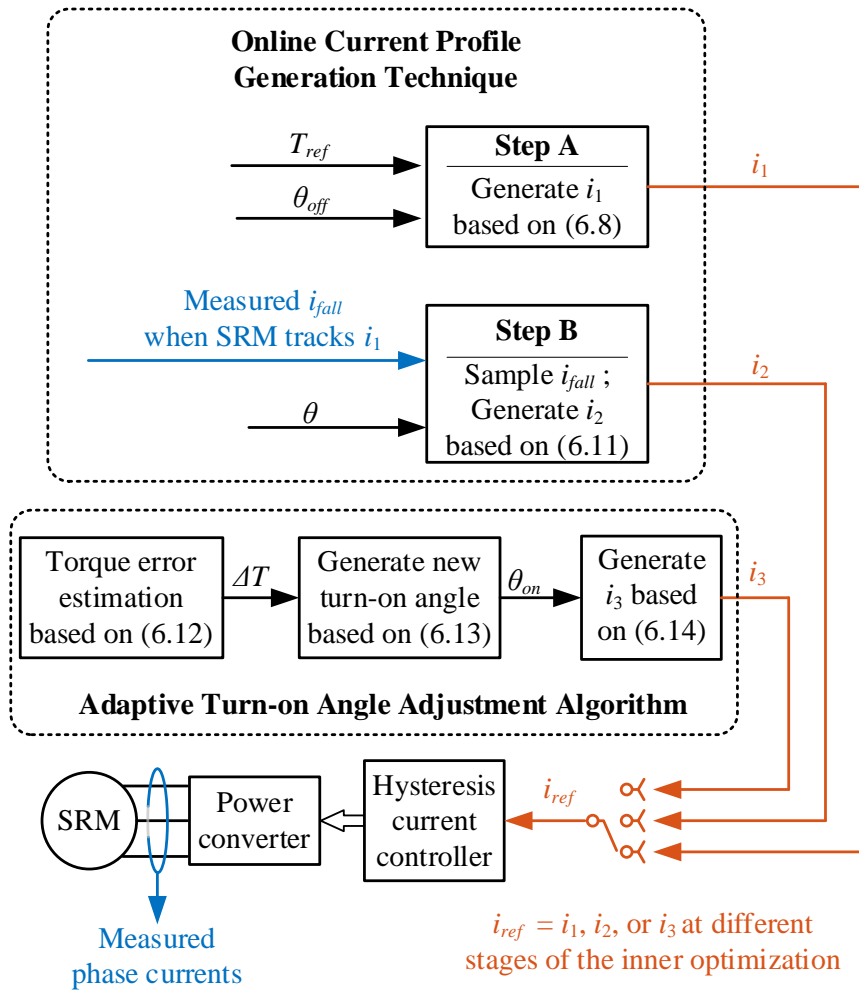


Fig. 6.4. Block diagram for the inner loop optimization.

In Step B of the online current profile generation in Fig. 6.4, the SRM is tracking  $i_1$ . Then, the demagnetization phase current after the turn-off angle (shown in Fig. 6.5(b) with a solid line in red) is measured. The rotor position  $\theta_{end}$ , which designates the angle when the phase current reaches zero after  $\theta_{off}$ , is found from the measured phase current. The sampled phase current in the  $[\theta_{off}, \theta_{end}]$  interval is defined as  $i_{fall}$ , as shown in Fig. 6.5(b). In a TSF, the sum of the adjacent phase torques should be equal to the reference torque. Thus, in  $[\theta_{off}, \theta_{end}]$  interval, by knowing one phase current (solid line in red in Fig. 6.5(b)), the current for the upcoming phase,  $i_{next}$  can be derived (shown in Fig. 6.5(b) with a solid line in grey).  $i_{next}$  within  $[\theta_{off}, \theta_{end}]$  interval is expressed as

$$i_{next}(\theta_{next}) = i_{LUT}(T_{ref} - T_{LUT}(i_{fall}, \theta), \theta_{next}), \theta_{off} \leq \theta \leq \theta_{end} \quad (6.10)$$

where  $\theta_{next}$  is the electrical position of the upcoming phase.  $\theta_{next}$  equals to  $\theta - \theta_{sft}$ .  $T_{LUT}$  represents the static torque characteristic, which is stored in the digital controller. In  $T_{LUT}$ , the phase torque is the output, and the phase current and rotor position are inputs. Due to the symmetry between the phases of an SRM, the current reference in  $[\theta_{off} - \theta_{sft}, \theta_{end} - \theta_{sft}]$  interval is same as  $i_{next}$  in  $[\theta_{off}, \theta_{end}]$  interval. Then, the current reference  $i_2$  can be expressed as in (6.11). It is worth noting that the calculation process in (6.10) is carried out at the same sampling cycle when  $i_{fall}$  is measured. Fig. 6.5(b) shows the profile of  $i_2$  with three solid lines in red (demagnetization region), black (single-phase conduction region), and green (overlapping region).

$$i_2 = \begin{cases} 0, & \theta < \theta_{oni} \\ i_{LUT}(T_{ref} - T_{LUT}(i_{fall}, \theta + \theta_{sft}), \theta), & \theta_{oni} \leq \theta < \theta'_{end} \\ i_{LUT}(T_{ref}, \theta), & \theta'_{end} \leq \theta < \theta_{off} \\ i_{fall}, & \theta_{off} \leq \theta < \theta_{end} \\ 0, & \theta \geq \theta_{end} \end{cases} \quad (6.11)$$

Once  $i_2$  is derived, it is applied to the hysteresis current control of SRM as  $i_{ref}$ , as shown in Fig. 6.4. Then, the average torque,  $T_{ave}$  is estimated when SRM tracks  $i_2$ .  $T_{ave}$  is the average value of the output torque, which is the sum of the phase torques calculated in the digital controller using the measured phase currents and rotor position. Then, the torque error can be calculated as expressed in (6.12). Theoretically, due to the symmetry between the phases of an SRM, it is adequate to measure the phase currents in one electrical phase shift angle as expressed in (6.9), to estimate the total output torque.

$$\Delta T = T_{ref} - T_{ave}. \quad (6.12)$$

The current reference  $i_2$  could be perfectly tracked, if the rate of change of the current was high enough. Then, the torque reference would be achieved without torque ripple ( $\Delta T = 0$ ) and the inner optimization loop would stop. The rms value of the phase current would be calculated and returned to the outer optimization loop. However, if the rate of change of the current is not high enough, then the current tracking error would occur. This further leads to a lower average output torque and higher torque ripple, especially within the  $[\theta_{oni}, \theta'_{end}]$  interval in Fig. 6.5(b). In that case, the proposed Adaptive Turn-on Angle Adjustment Algorithm is applied as shown in Fig. 6.4 and a new current reference  $i_3$  is generated based on the torque

error. It should be noted that  $i_2$  in the  $[\theta_{oni}, \theta'_{end}]$  interval in Fig. 6.5(b) is derived from the static torque characteristic. Thus, to satisfy the average torque in the  $[\theta_{oni}, \theta'_{end}]$  interval, the peak value of  $i_2$  within this interval should be achieved. As shown in Fig. 6.5(b), the rotor position, where the phase current in  $[\theta_{oni}, \theta'_{end}]$  interval reaches to its peak value  $i_p$ , is designated as  $\theta_p$ . In order to ensure that the current tracking is achieved in the  $[\theta_{oni}, \theta'_{end}]$  interval, the proposed Adaptive Turn-on Angle Adjustment Algorithm is used to replace  $i_2$  in this interval with a new current reference. The new reference takes the current dynamics into consideration while ensuring  $i_p$  is achievable to deliver the reference torque.

The approach is similar to the example provided in Fig. 6.2. The applied turn-on angle  $\theta_{on\beta}$  is advanced so that the phase current increases before  $\varepsilon_\beta$  reaches to  $V_{dc}$ . This increases the rise time of the phase current and improves the output torque. Thus, in the proposed Adaptive Turn-on Angle Adjustment Algorithm, the turn-on angle is iteratively modified to adjust the rise time of the phase current. A new turn-on angle is derived in each iteration based on the torque error, as expressed in (6.13):

$$\theta_{on} = \theta_{on} - r\Delta T \quad (6.13)$$

where  $r$  is the proportional gain, which can be tuned according to the operational characteristics of the SRM. A high proportional gain provides a large change in  $\theta_{on}$  for a given torque error. The control system may become unstable if  $r$  is too high. In contrast, a low gain results in a small change in  $\theta_{on}$ . The control system may become less sensitive to the change in torque error  $\Delta T$ , if  $r$  is too low. Notable, there

should be limitations for how much  $\theta_{on}$  can be advanced. The boundary is related to the phase inductance of the SRM. In this thesis, the minimum  $\theta_{on}$  is set as  $-60^\circ$  for a 3-phase SRM.

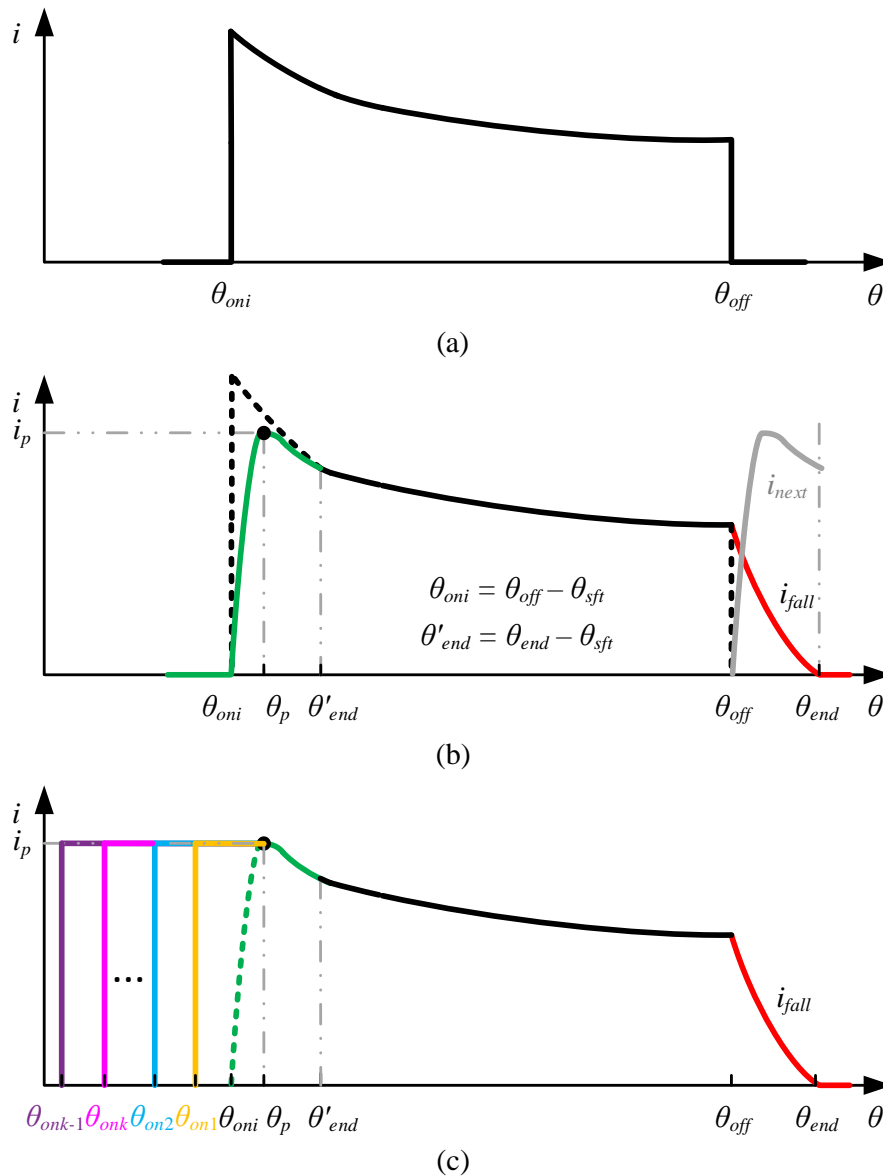


Fig. 6.5. Current reference generated in the inner optimization loop. (a) Step A. (b) Step B. (c). Adaptive turn-on angle adjustment.

The Adaptive Turn-on Angle Adjustment Algorithm shown in Fig. 6.4, operates iteratively. In each iteration, the torque error is estimated based on (6.12). If the torque error is not satisfied, a new turn-on angle is calculated using (6.13). A new current reference  $i_3$  is generated based on (6.14) and it is applied to the hysteresis current control of the SRM as  $i_{ref}$ . A new torque error in the next iteration is obtained when SRM tracks  $i_3$ .

$$i_3 = \begin{cases} 0, & \theta < \theta_{on} \\ i_p, & \theta_{on} \leq \theta < \theta_p \\ i_{LUT} \left( T_{ref} - T_{LUT} \left( i_{fall}, \theta + \theta_{sft} \right), \theta \right), & \theta_p \leq \theta < \theta'_{end} \\ i_{LUT} \left( T_{ref}, \theta \right), & \theta'_{end} \leq \theta < \theta_{off} \\ i_{fall}, & \theta_{off} \leq \theta < \theta_{end} \\ 0 & \theta \geq \theta_{end} \end{cases} \quad (6.14)$$

The Adaptive Turn-on Angle Adjustment Algorithm repeats until the torque error is small enough. It is worth noting that the above mentioned iterations repeats for a given turn-off angle from the outer optimization loop. As shown in Fig. 6.3, in each iteration of the outer loop optimization, a turn-off angle candidate is applied to the inner loop optimization, and the inner loop optimization repeats until the torque error is satisfied. If none of the turn-on angles achieve the required torque with the given turn-off angle, the current iteration of the outer loop optimization would stop when the highest torque is achieved. By iteratively adjusting the turn-on angle, different  $i_3$  is obtained. Therefore, a flexible rise time for the phase current is achieved. Fig. 6.5(c) shows examples of  $i_3$  in the first, second,  $(k-1)^{th}$ , and  $k^{th}$  iterations. Compared to  $i_2$ , only the current reference before  $\theta_p$  changes in  $i_3$ , which

means that only the current rise time is adjusted in the proposed Adaptive Turn-on Angle Adjustment Algorithm.

The proposed method takes the current dynamics into consideration in an iterative process. The current reference waveform  $i_1$  (shown in Fig. 6.5(a)) was derived only using the inverse static torque characteristic LUT. Compared to  $i_1$ , the current reference after  $\theta_{off}$  changes in  $i_2$  (shown in Fig. 6.5(b)), which is the measured demagnetization phase current  $i_{fall}$ . Thus, the current dynamics for the outgoing phase during commutation is fully taken into account. There will be no current tracking error after the turn-off angle. However, for  $i_2$ , the current reference in the  $[\theta_{oni}, \theta'_{end}]$  was derived only using the inverse static torque characteristic. Thus, the current tracking performance for the incoming phase during commutation could not be guaranteed. Compared to  $i_2$ , only the current reference before  $\theta_p$  changes in  $i_3$  (shown in Fig. 6.5(c)) to provide the appropriate current rising time to achieve  $i_p$  for the given operating speed and the turn-off angle. The current reference after  $\theta_p$  remains the same for different turn-on angle adjustment iterations. The current reference before  $\theta_p$  is used to provide more rise time for the incoming phase current. It is important to emphasize that, the proposed TSF does not require the phase current to track the rectangular current reference in  $[\theta_{onk}, \theta_p]$  interval in Fig. 6.5(c).

As shown in Fig. 6.3, for a given turn-off angle candidate in an outer loop optimization, the inner loop optimization repeats until an appropriate  $i_3$  is obtained that provides a satisfactory torque error. Then, the rms current is calculated when

SRM tracks this  $i_3$ , and it is compared to the rms current obtained from the previous  $\theta_{off}$  candidate in the previous outer loop optimization. Critical angles like  $\theta_{offmax}$ ,  $\theta_{offmin}$ ,  $\theta_{off1}$ , and  $\theta_{off2}$  are updated as in (6.5) or (6.6) based on the comparison. A new  $\theta_{off}$  candidate is generated, and then the two-step Online Current Profile Generation Technique and the Adaptive Turn-on Angle Adjustment Algorithm in Fig. 6.4 are executed again for this new turn-off angle candidate. The outer optimization loop continues until the difference between  $\theta_{off2}$  and  $\theta_{off1}$  is sufficiently small, and the latest current reference will be the optimal current reference for the given torque reference and operating speed.

## 6.4 Simulation Evaluation

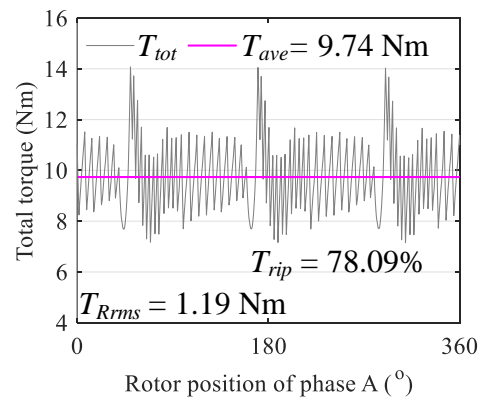
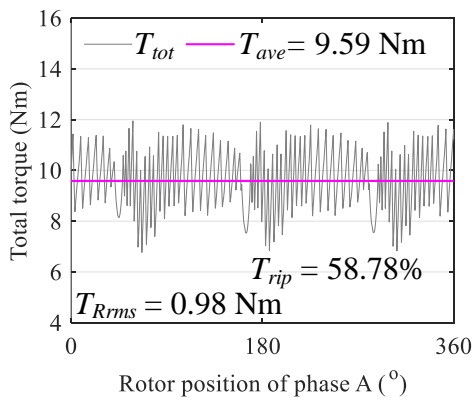
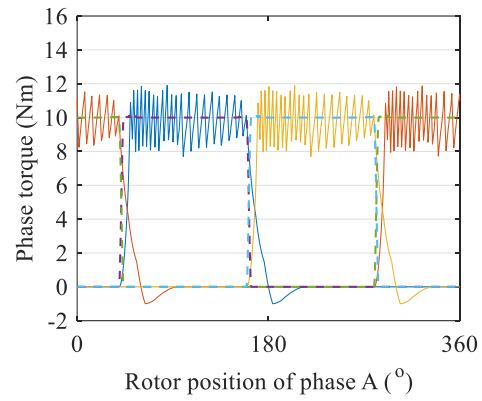
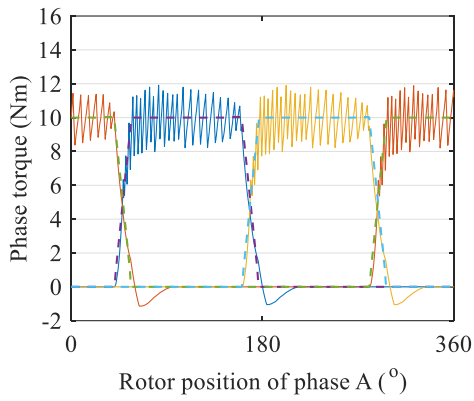
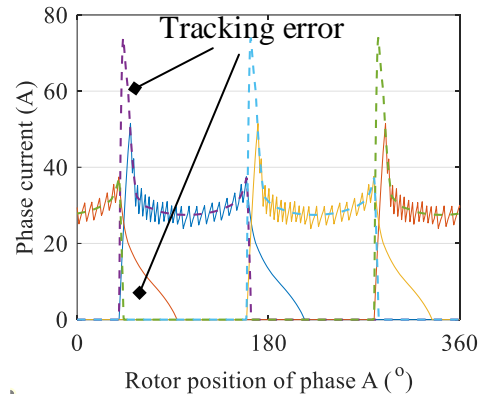
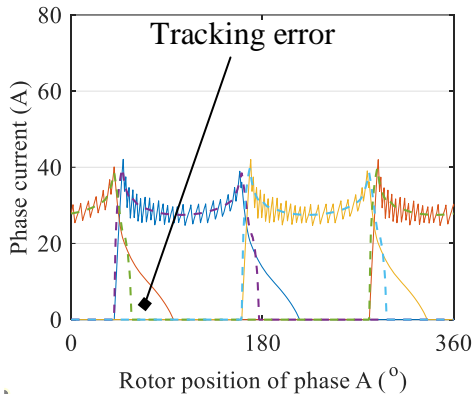
In this section, the evaluation of the proposed online TSF is performed by simulation on a 5.5 kW, 1000 r/min, 3-phase, 12/8 SRM. The design specifications of the SRM are shown in Table 4.1. The SRM model is built in MATLAB/Simulink using the measured static characteristics. The current sampling frequency is 40 kHz, and the dc-link voltage is 72 V. Performance at low-speed (500 r/min), rated-speed (1000 r/min), and high-speed (1500 r/min) are evaluated.

Four typical conventional TSFs [27] and a typical optimization-based TSF [41] are implemented for the performance comparison. The rise and fall functions of adopted conventional TSFs are expressed as in (5.3)-(5.10), respectively. The objective function and constraints for the TSF [41] in are expressed as (5.11)-(5.14).

A multi-objective GA is used to optimize the turn-on and overlapping angles for the conventional TSFs, and the weight parameter for the TSF in [41], to minimize the rms current  $i_{rms}$  and rms torque ripple  $T_{Rrms}$ .

Dynamic simulation results at 500 r/min and 10 Nm torque reference are shown in Fig. 6.6. The optimized conventional TSFs provide 9.59 Nm to 9.74 Nm with some torque ripple ( $T_{Rrms} = 0.98$  Nm to 1.19 Nm,  $T_{rip} = 58.78\%$  to 81.80%) as shown in Fig. 6.6(a) to (d), and the TSF in [41] provides 9.72 Nm with some torque ripple ( $T_{Rrms} = 1.06$  Nm,  $T_{rip} = 75.84\%$ ), as shown in Fig. 6.6(e). Owing to the current dynamics consideration, almost no current tracking error is observed in Fig. 6.6(f) for the proposed TSF. Higher average torque ( $T_{ave} = 9.81$  Nm) and lower torque ripple ( $T_{Rrms} = 0.93$  Nm,  $T_{rip} = 50.10\%$ ) is obtained. Some current tracking error can be observed for the conventional TSF and TSF in [41], as shown in Fig. 6.6(a) to Fig. 6.6(e). However, the error is not large enough to cause big torque ripple. This is because the rate of change of current is high at low speed (500 r/min). Hence, it is insignificant to consider the current dynamics.

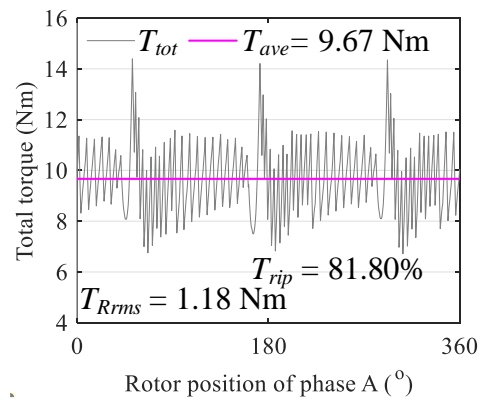
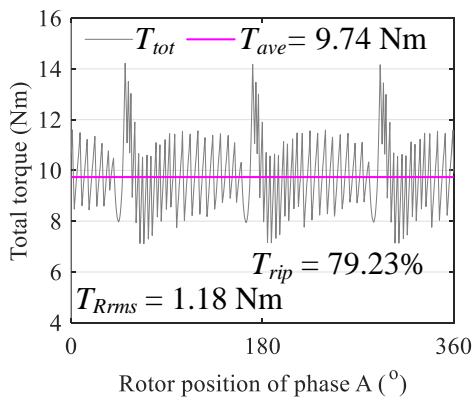
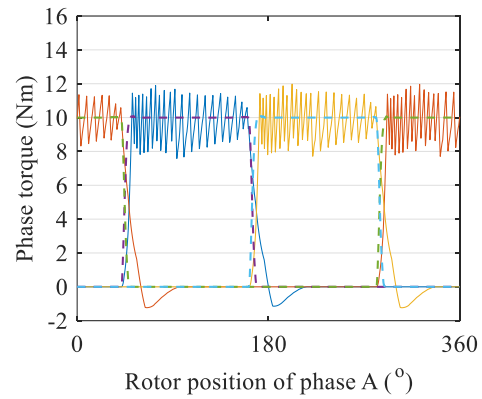
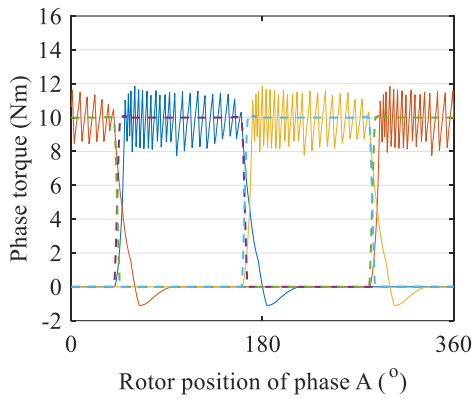
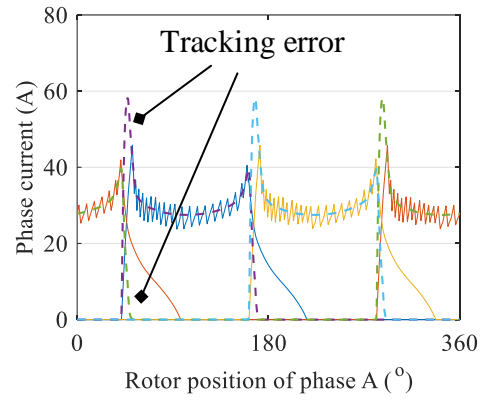
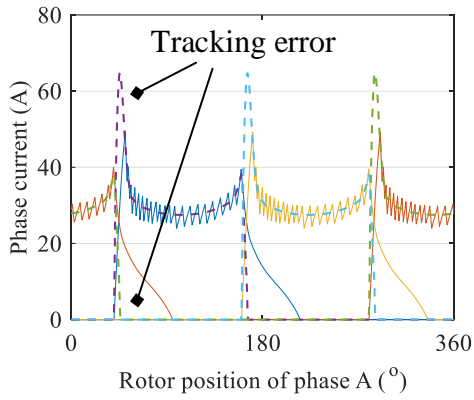
— Phase A response    — Phase B response    — Phase C response  
- - - Phase A reference    - - - Phase B reference    - - - Phase C reference



(a)

(b)

— Phase A response    — Phase B response    — Phase C response  
- - - Phase A reference    - - - Phase B reference    - - - Phase C reference



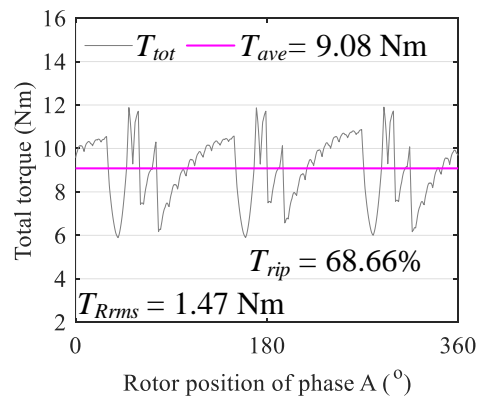
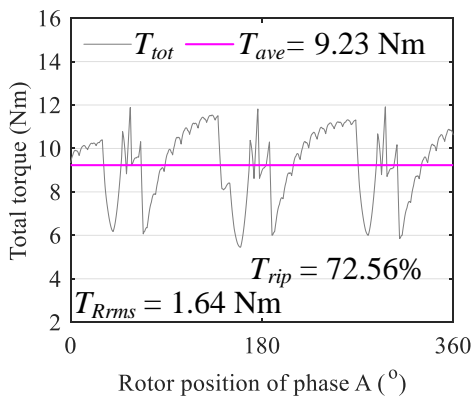
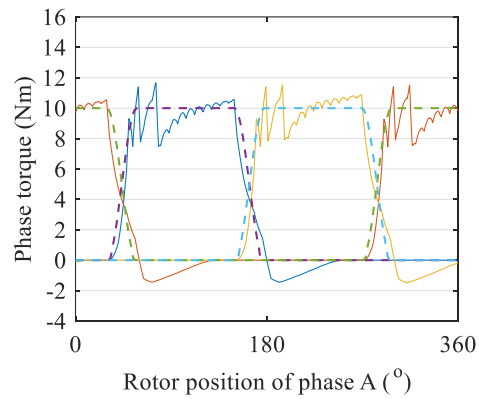
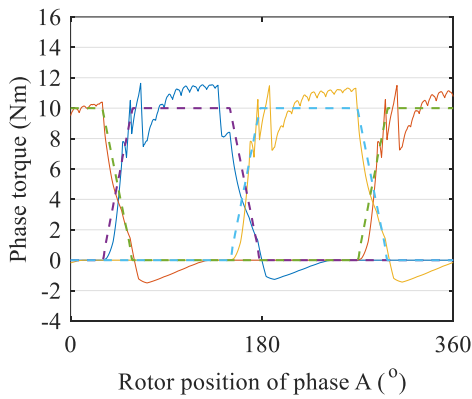
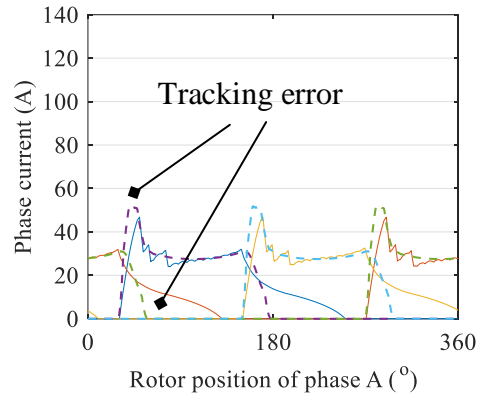
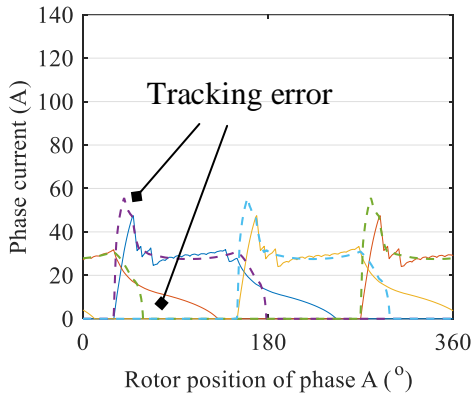
(c)

(d)



Dynamic simulation results at rated-speed (1000 r/min) and 10 Nm torque reference are shown in Fig. 6.7. It can be observed from Fig. 6.7(a) to (e) that, the current tracking performance degrades when the speed increases, which results in lower average torque and higher torque ripple. Only 9.08 Nm to 9.23 Nm are provided by the optimized conventional TSFs. Owing to the consideration of the induced EMF as expressed in (5.14), the TSF in [41] provides higher average torque (9.61 Nm) and lower torque ripple ( $T_{Rms} = 1.59$  Nm,  $T_{rip} = 75.88\%$ ), compared to the conventional TSFs. However, large current tracking error can be still observed, especially during commutation. This is because the current dynamics cannot be considered by (5.14). Compared to other TSFs, the proposed TSF still show lower torque ripple ( $T_{Rms} = 1.12$  Nm,  $T_{rip} = 49.18\%$ ) and higher average torque ( $T_{ave} = 9.92$  Nm).

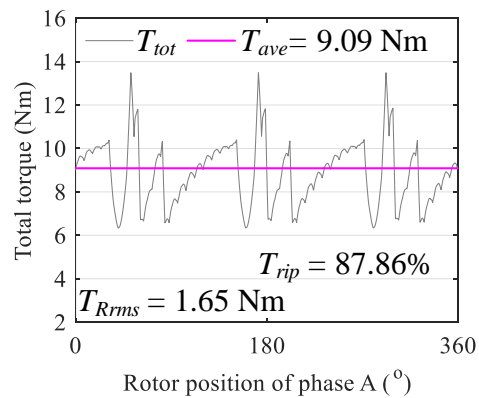
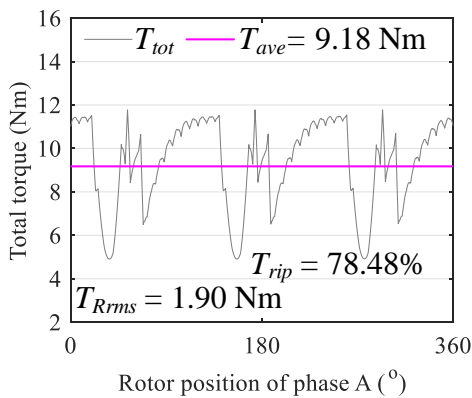
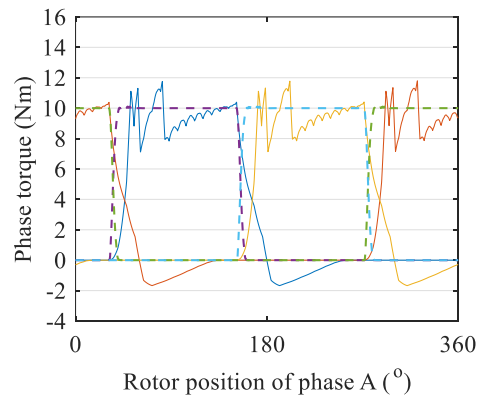
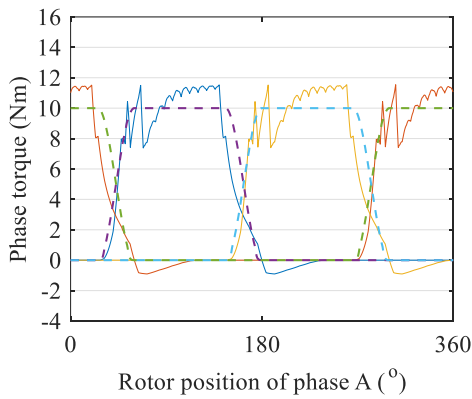
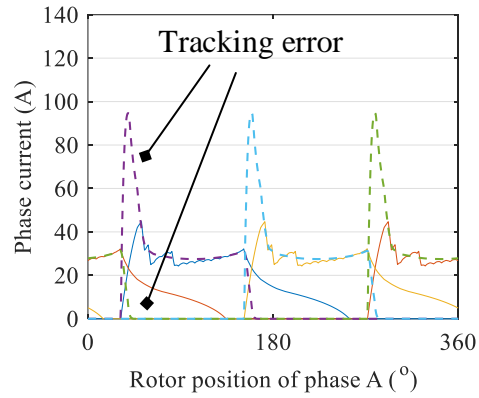
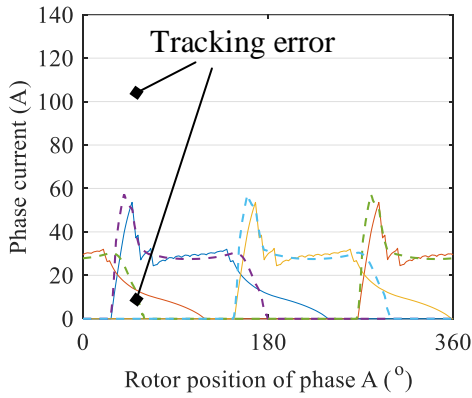
— Phase A response    — Phase B response    — Phase C response  
- - - Phase A reference    - - - Phase B reference    - - - Phase C reference



(a)

(b)

— Phase A response    — Phase B response    — Phase C response  
- - - Phase A reference    - - - Phase B reference    - - - Phase C reference



(c)

(d)

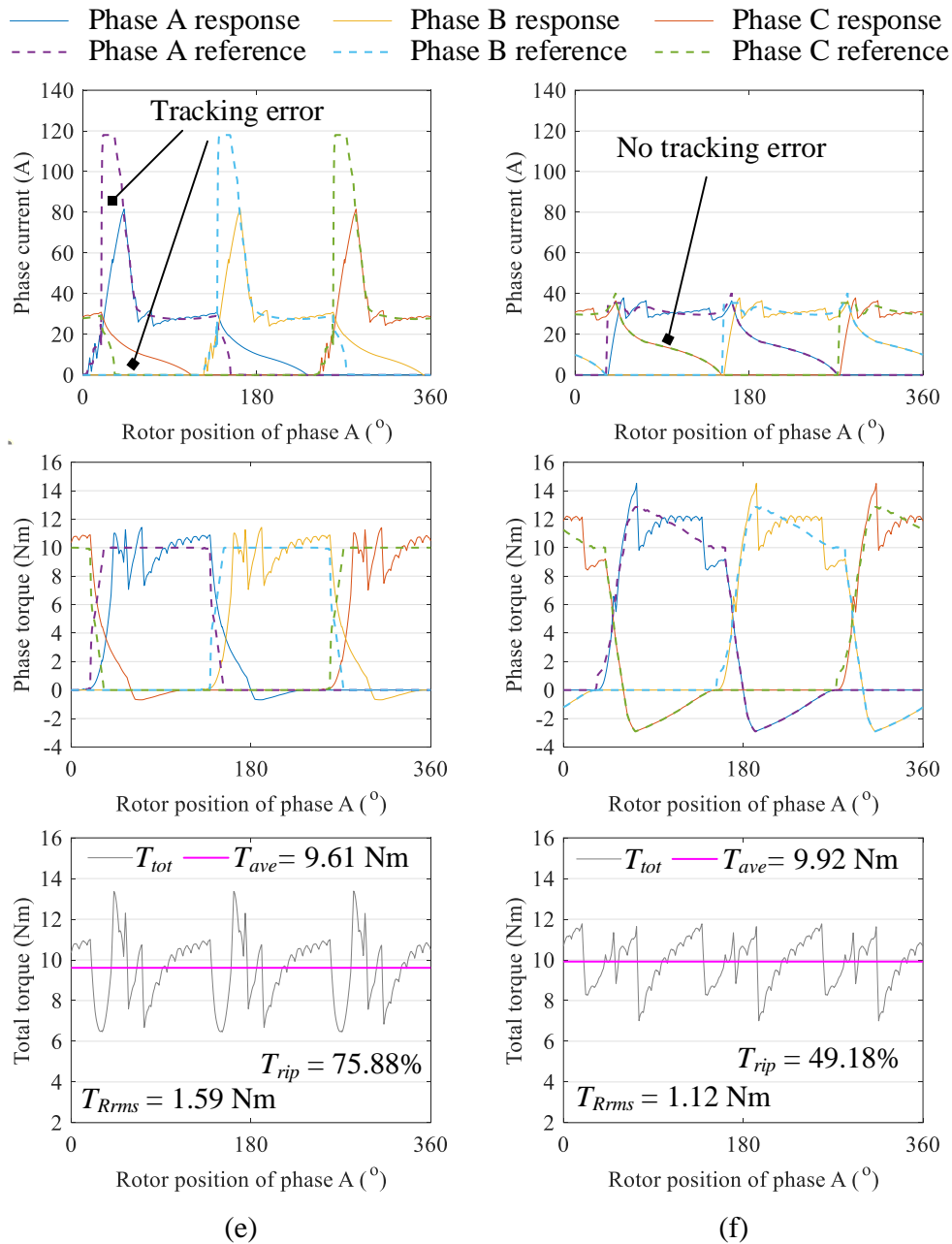
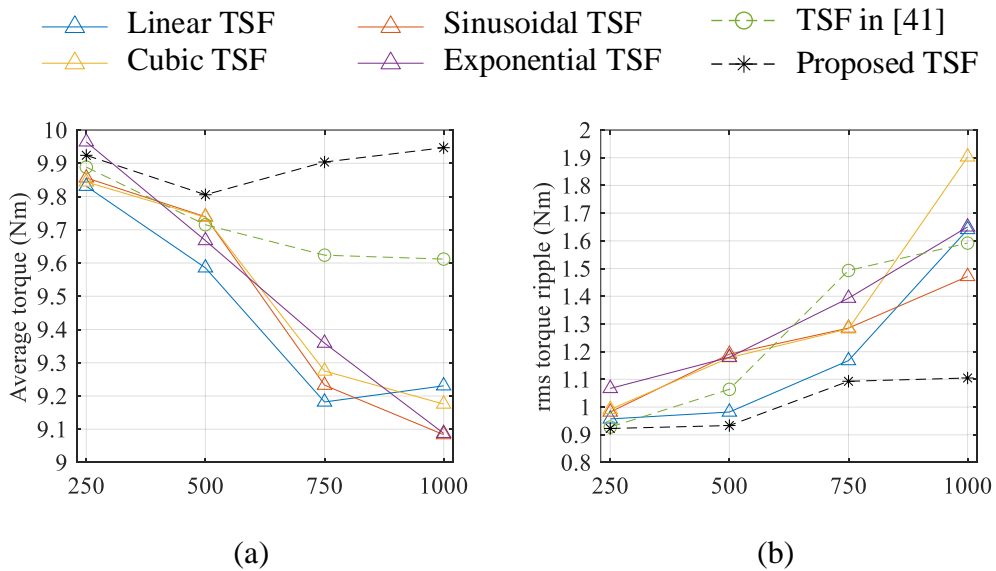


Fig. 6.7. Simulation results at 1000 r/min and 10 Nm torque reference. (a) Linear TSF,  $\theta_{on} = 29.84^\circ$ ,  $\theta_{ov} = 28.53^\circ$ . (b). Sinusoidal TSF,  $\theta_{on} = 29.18^\circ$ ,  $\theta_{ov} = 28.81^\circ$ . (c). Cubic TSF,  $\theta_{on} = 25.86^\circ$ ,  $\theta_{ov} = 33.91^\circ$ . (d). Exponential TSF,  $\theta_{on} = 31.51^\circ$ ,  $\theta_{ov} = 20.53^\circ$ . (e). TSF in [41],  $\sigma = 38.79$ . (f). Proposed online TSF,  $\theta_{on} = 34.07^\circ$ ,  $\theta_{off} = 162.05^\circ$ .

A quantitative comparison is shown in Fig. 6.8 for the proposed TSF, optimized conventional TSFs, and TSF in [41]. The torque reference is 10 Nm, and the operating speeds are varied from 250 r/min to 1000 r/min. The average output torque  $T_{ave}$ , rms torque ripple  $T_{Rrms}$ , rms current  $i_{rms}$ , and torque ripple percentage  $T_{rip}$  for one electrical cycle are compared. It can be observed from Fig. 6.8 that all the six TSFs can provide around 10 Nm at 250 r/min with low torque ripple. When the speed increases, the proposed TSF shows higher average torque and lower torque ripple. Unlike the proposed TSF, the performance of the conventional TSFs and the TSF in [41] degrade when the speed increases. From Fig. 6.8, it can be concluded that the proposed TSF provides improved torque-speed capability, reduced torque ripple, and better current tracking performance.



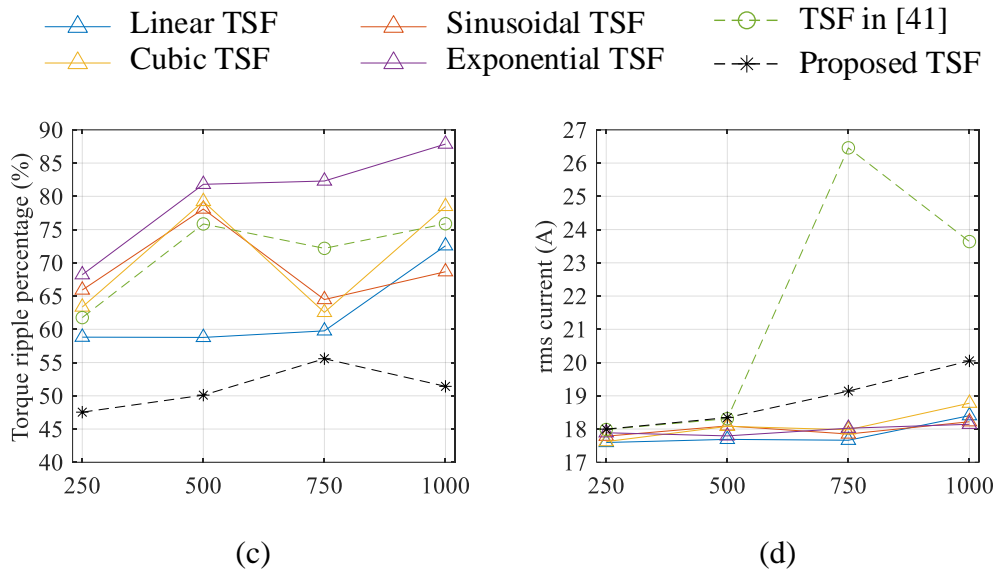
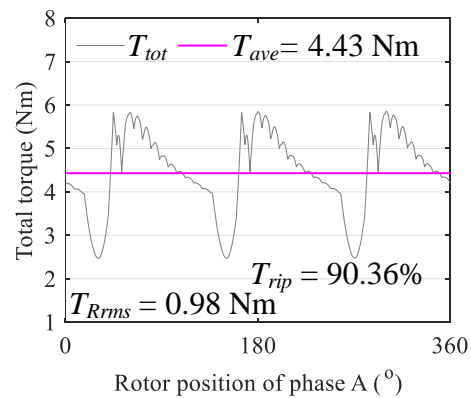
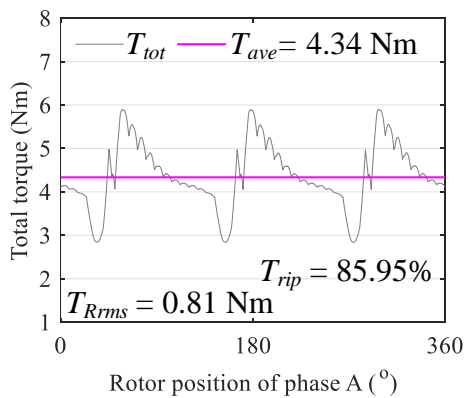
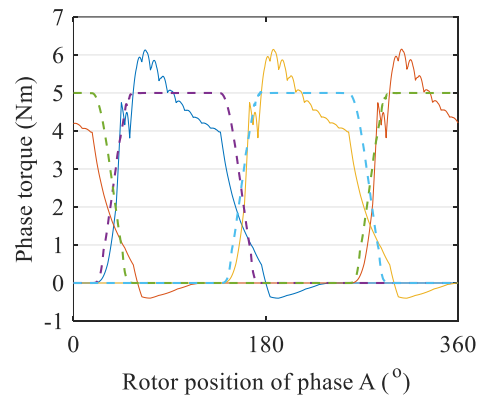
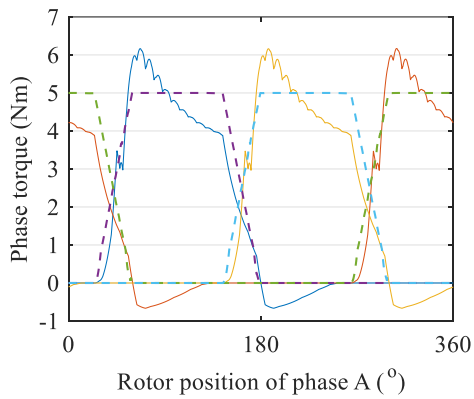
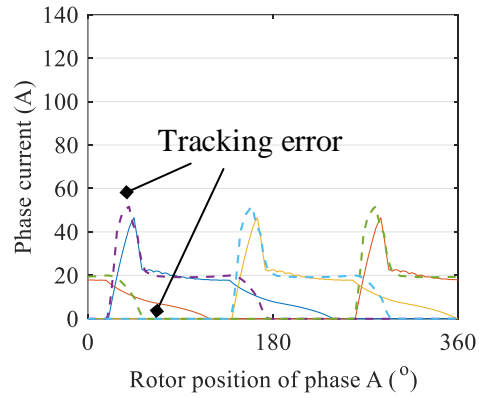
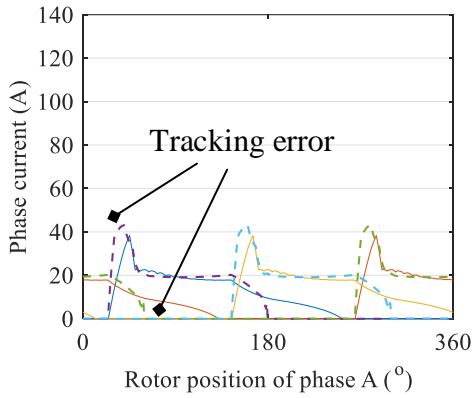


Fig. 6.8. Simulation comparison between different TSFs. (a). Average torque. (b). rms torque ripple. (c). rms current. (d). Torque ripple percentage.

Dynamic simulation results at higher speed (1500 r/min) and 5 Nm torque reference are shown in Fig. 6.9. It is worth noting that higher induced EMF is achieved at 1500 r/min, since it is beyond the rated-speed (1000 r/min) of the reference SRM. Thus, larger current tracking error can be observed in Fig. 6.9(a) to (e), which causes increased torque ripple and decreased average torque for the conventional TSFs and the TSF in [41]. However, due to the current dynamics consideration, the proposed TSF still provide lower torque ripple and higher average torque.

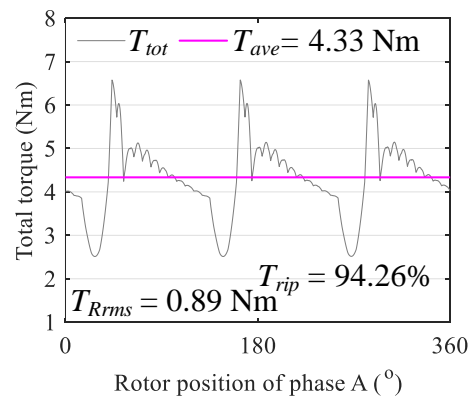
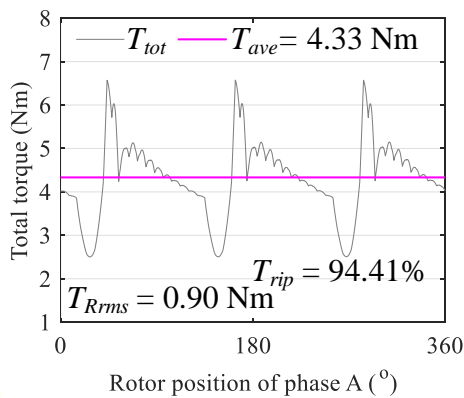
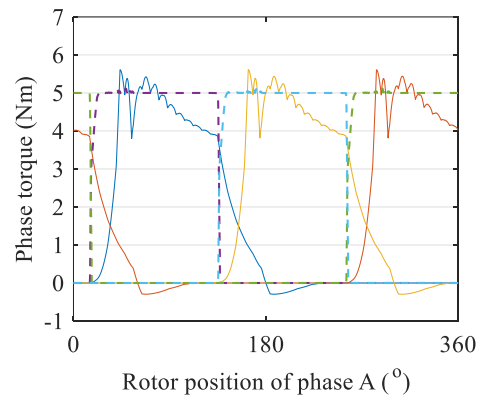
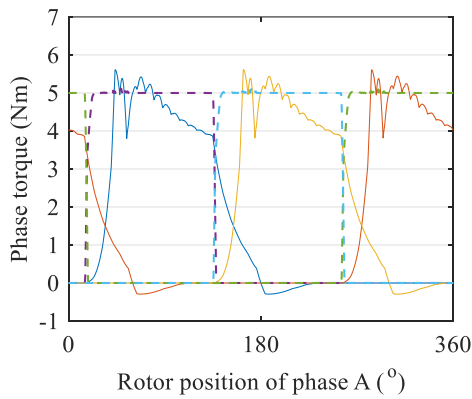
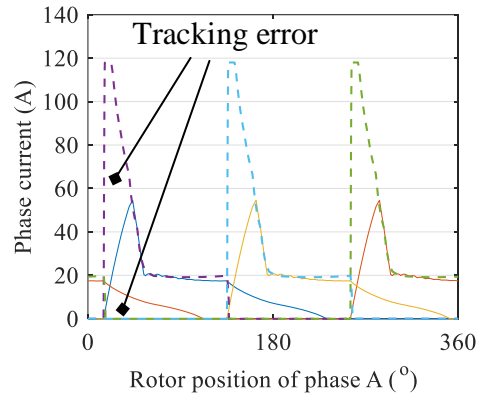
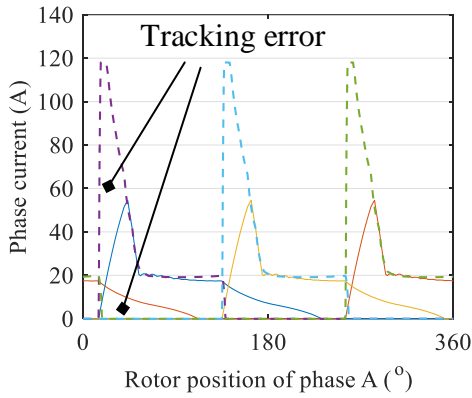
— Phase A response    — Phase B response    — Phase C response  
- - - Phase A reference    - - - Phase B reference    - - - Phase C reference



(a)

(b)

— Phase A response    — Phase B response    — Phase C response  
- - - Phase A reference    - - - Phase B reference    - - - Phase C reference



(c)

(d)



## 6.5 Experimental Validation

In this section, the evaluation of the proposed online TSF is performed by experiments on the same 3-phase SRM. As shown in Fig. 6.10, an induction machine operating in speed loop, is connected to the SRM. The control frequency of the digital controller Texas Instrument digital signal processor (DSP) TMS320F28335 is set as 40 kHz for all the experiments. The power converter is constructed by Infineon IGBT module F4-250R17MP4. The dc-link voltage is 72 V. For the conventional TSFs and TSF in [41], the optimal current references generated by offline GA optimization are stored as LUTs in the DSP. Unlike other TSFs, the proposed TSF generates the current reference online: (i)  $i_{ref1}$  in Fig. 6.5 is generated using the inversed torque-position-current LUT, which is stored in the DSP; (ii)  $i_{fall}$  is measured online and then used to generate  $i_{ref2}$ ; (iii)  $\theta_{on}$  and  $\theta_{off}$  are optimized based on the average torque and rms current, which are calculated using the real-time measured three-phase currents and rotor position. A hysteresis current controller is used to track all the current references. The instantaneous phase torque waveforms shown in this section are estimated using the measured rotor position and phase currents, and the total torque waveform is the sum of the estimated phase torque waveforms.

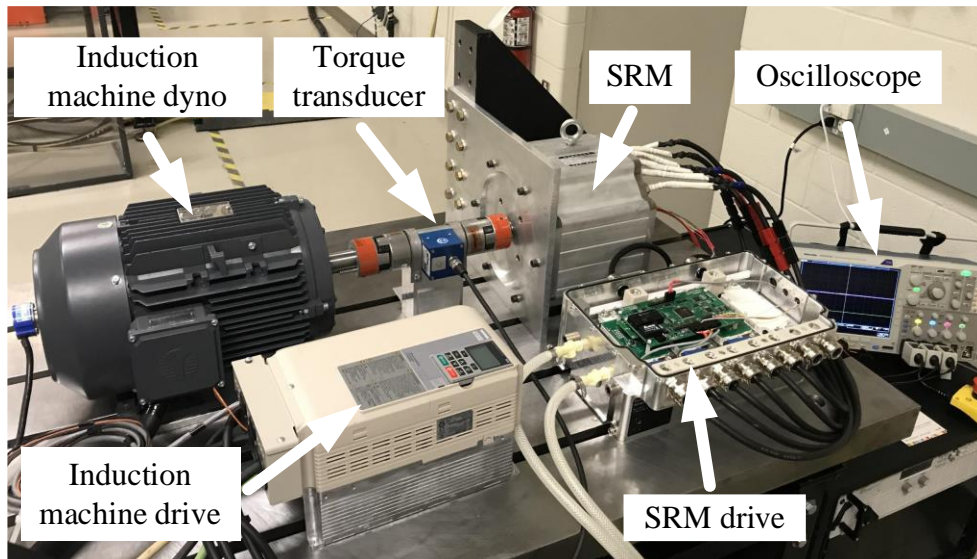
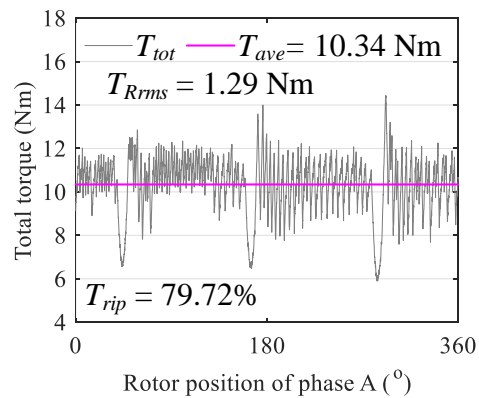
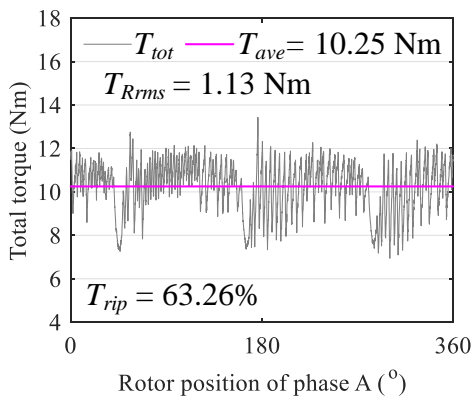
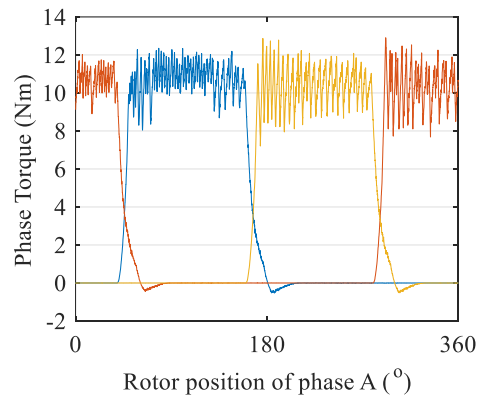
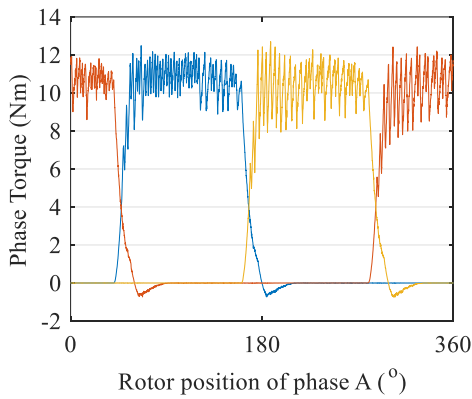
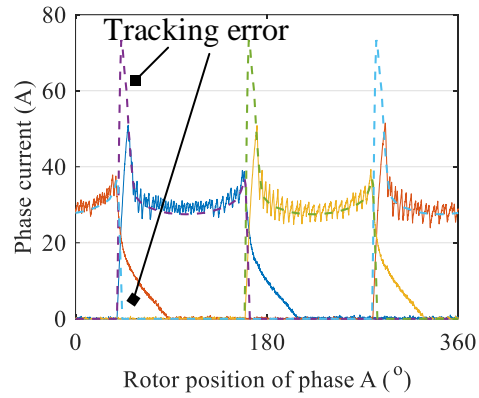
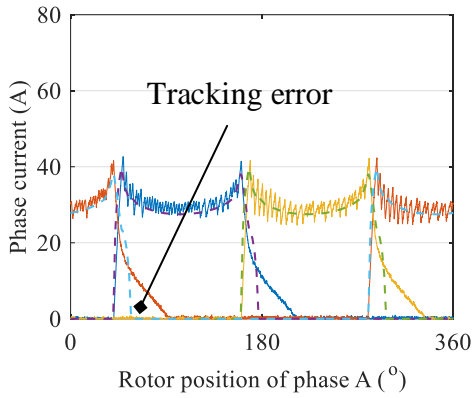


Fig. 6.10. Photograph of the experimental setup.

Fig. 6.11 shows the experimental results at 500 r/min and 10 Nm torque command. It can be observed that the values of the average torque provided by all the TSFs are larger than 10 Nm. For the conventional TSFs, the average torque varies from 10.25 Nm to 10.42 Nm. The TSF in [41] provides 10.20 Nm. The proposed TSF provides most accurate output torque (10.11 Nm), which is owing to the current dynamics consideration. Similar to the simulation results, there is no current tracking error in Fig. 6.11(f) for the proposed TSF. Only small current tracking errors can be observed in Fig. 6.11(a) to (e). This is because a fast rate-of-change-of current can be achieved at 500 r/min. Thus, the influence is not obvious when ignoring the current dynamics.

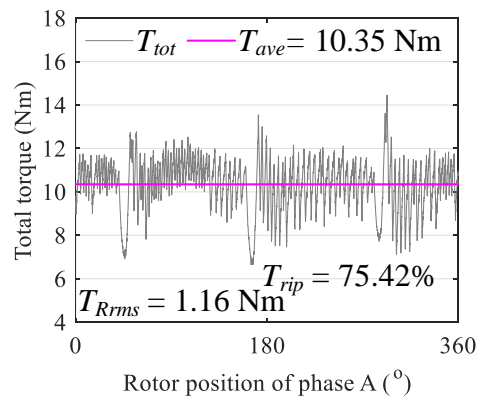
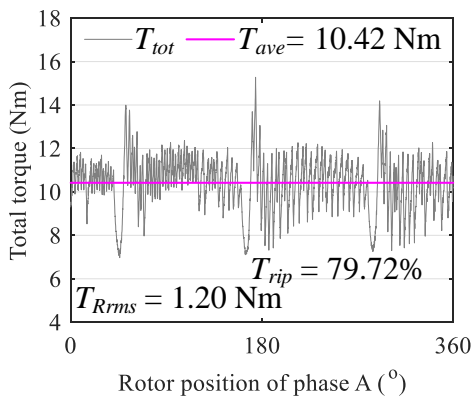
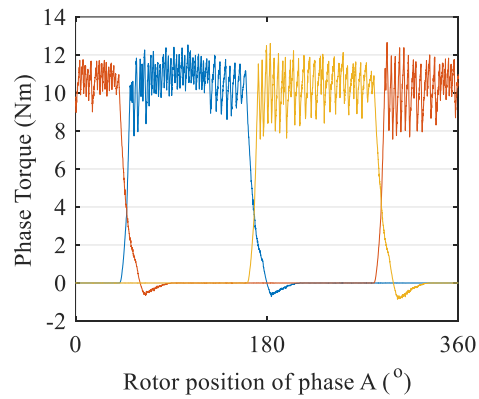
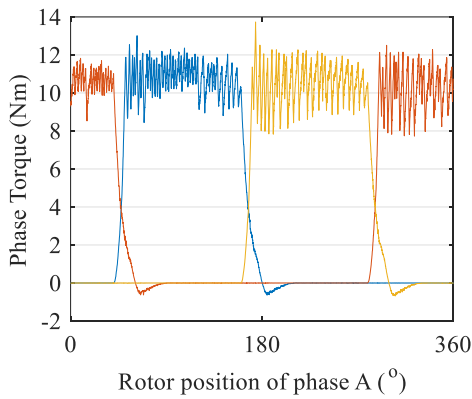
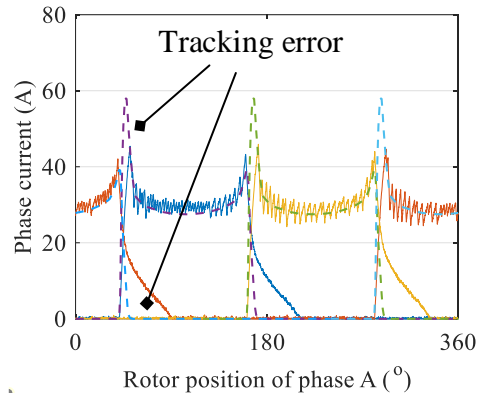
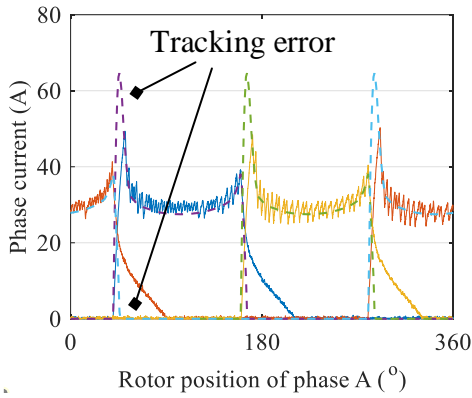
— Phase A response    — Phase B response    — Phase C response  
- - - Phase A reference    - - - Phase B reference    - - - Phase C reference



(a)

(b)

— Phase A response    — Phase B response    — Phase C response  
- - - Phase A reference    - - - Phase B reference    - - - Phase C reference



(c)

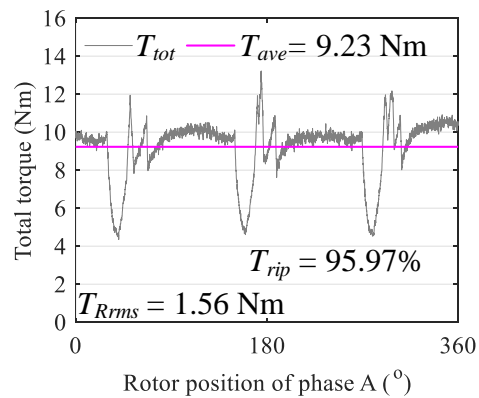
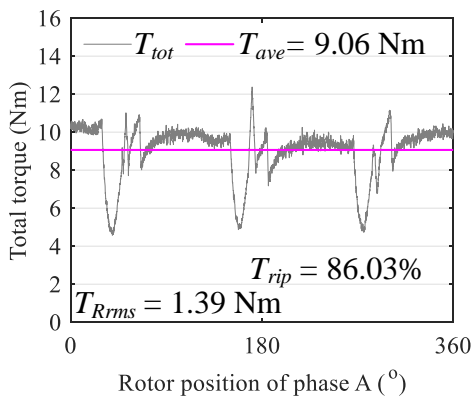
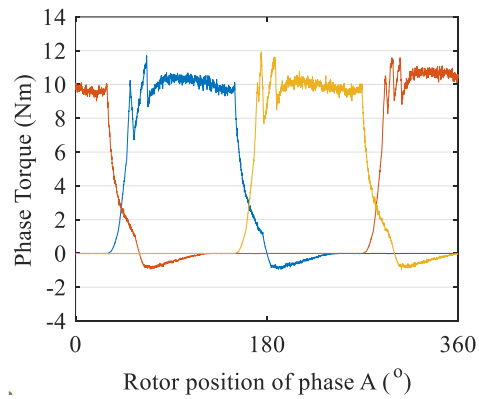
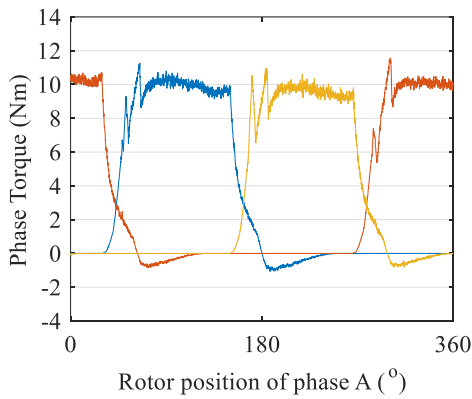
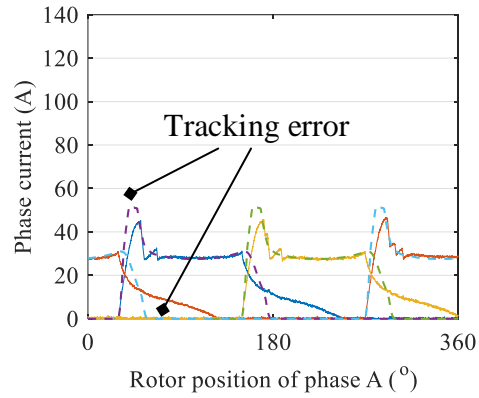
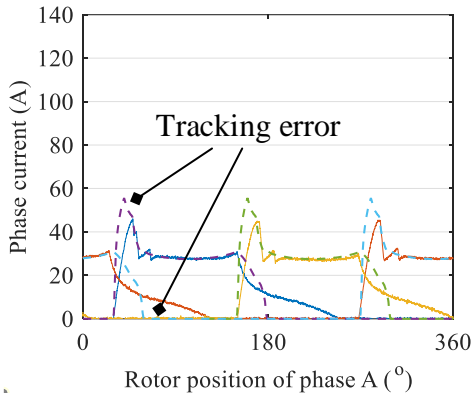
(d)



Fig. 6.12 shows the experimental results at the rated-speed (1000 r/min) and 10 Nm torque command. Compared to the conventional TSFs ( $T_{ave} = 9.06$  Nm to 9.24 Nm,  $T_{Rrms} = 1.39$  Nm to 1.69 Nm,  $T_{rip} = 80.86\%$  to 95.97%) and TSF in [41] ( $T_{ave} = 9.54$  Nm,  $T_{Rrms} = 1.82$  Nm,  $T_{rip} = 97.1\%$ ), the proposed TSF provide most accurate average torque ( $T_{ave} = 9.96$  Nm) and smallest torque ripple ( $T_{Rrms} = 0.55$  Nm,  $T_{rip} = 30.79\%$ ). Large current tracking error can be observed in Fig. 6.12(a) to (e), especially in the overlapping region, and the proposed TSF still provides almost no current tracking error. This is because the induced EMF is high at 1000 r/min, which results in a slow rate-of-change-of current. Therefore, the impact of the current dynamics consideration is significant.

Fig. 6.13 shows the experimental results at 1500 r/min and 5 Nm torque command. Only one or two switching operations can be observed in the hysteresis current control. This is because 1500 r/min, beyond the rated-speed (1000 r/min), enables a higher induced EMF. It leads to poor current control performance with the rated dc-link voltage. It can be observed that the values of the average torque provided by all the TSFs are less than 5 Nm. As shown in Fig. 6.13(a), the linear TSF provides the smallest torque ripple ( $T_{Rrms} = 0.58$  Nm,  $T_{rip} = 85.39\%$ ), but the average torque is also the lowest ( $T_{ave} = 3.39$  Nm). Compared to the conventional TSFs and TSF in [41], the proposed TSF provides the largest average torque and relatively small torque ripple ( $T_{Rrms} = 0.88$  Nm,  $T_{rip} = 94.68\%$ ).

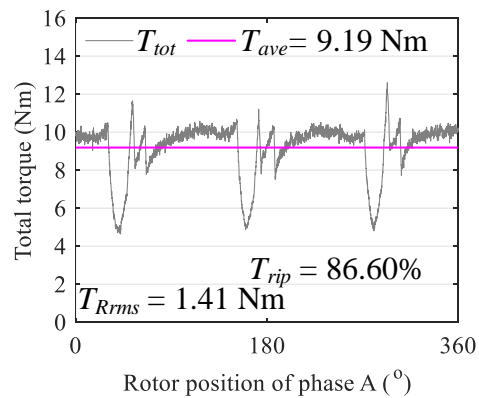
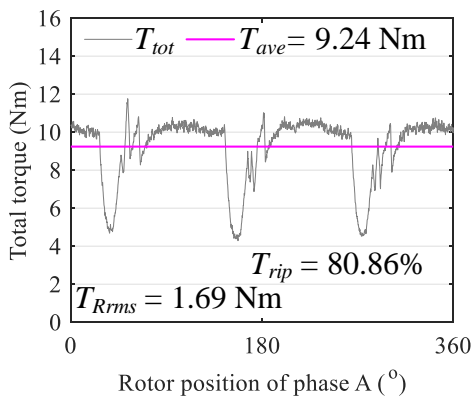
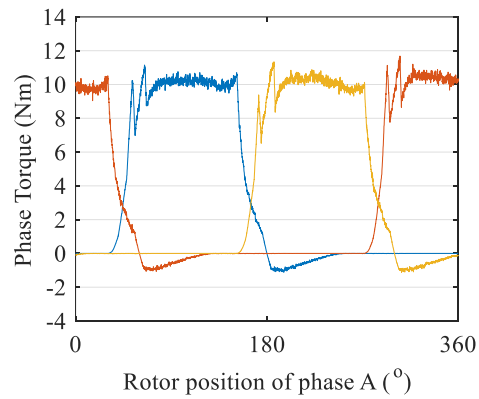
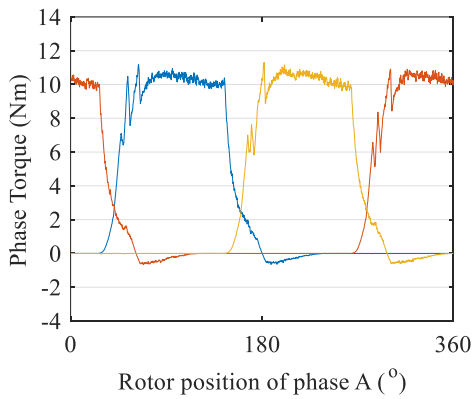
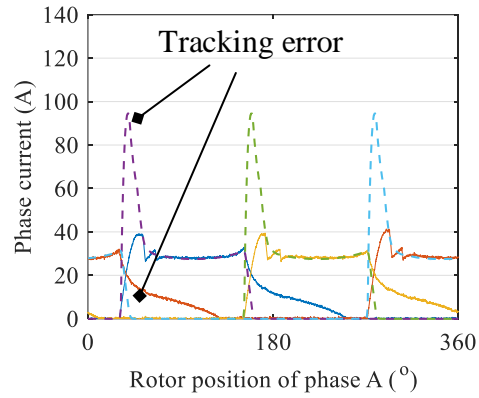
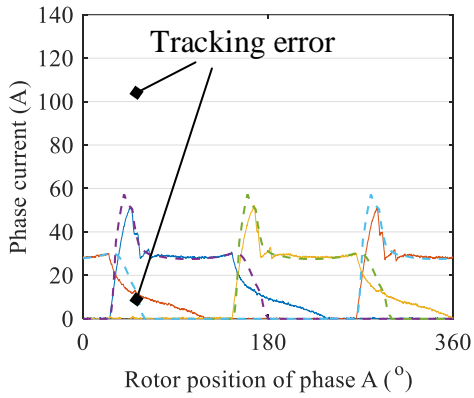
— Phase A response    — Phase B response    — Phase C response  
- - - Phase A reference    - - - Phase B reference    - - - Phase C reference



(a)

(b)

— Phase A response    — Phase B response    — Phase C response  
- - - Phase A reference    - - - Phase B reference    - - - Phase C reference



(c)

(d)

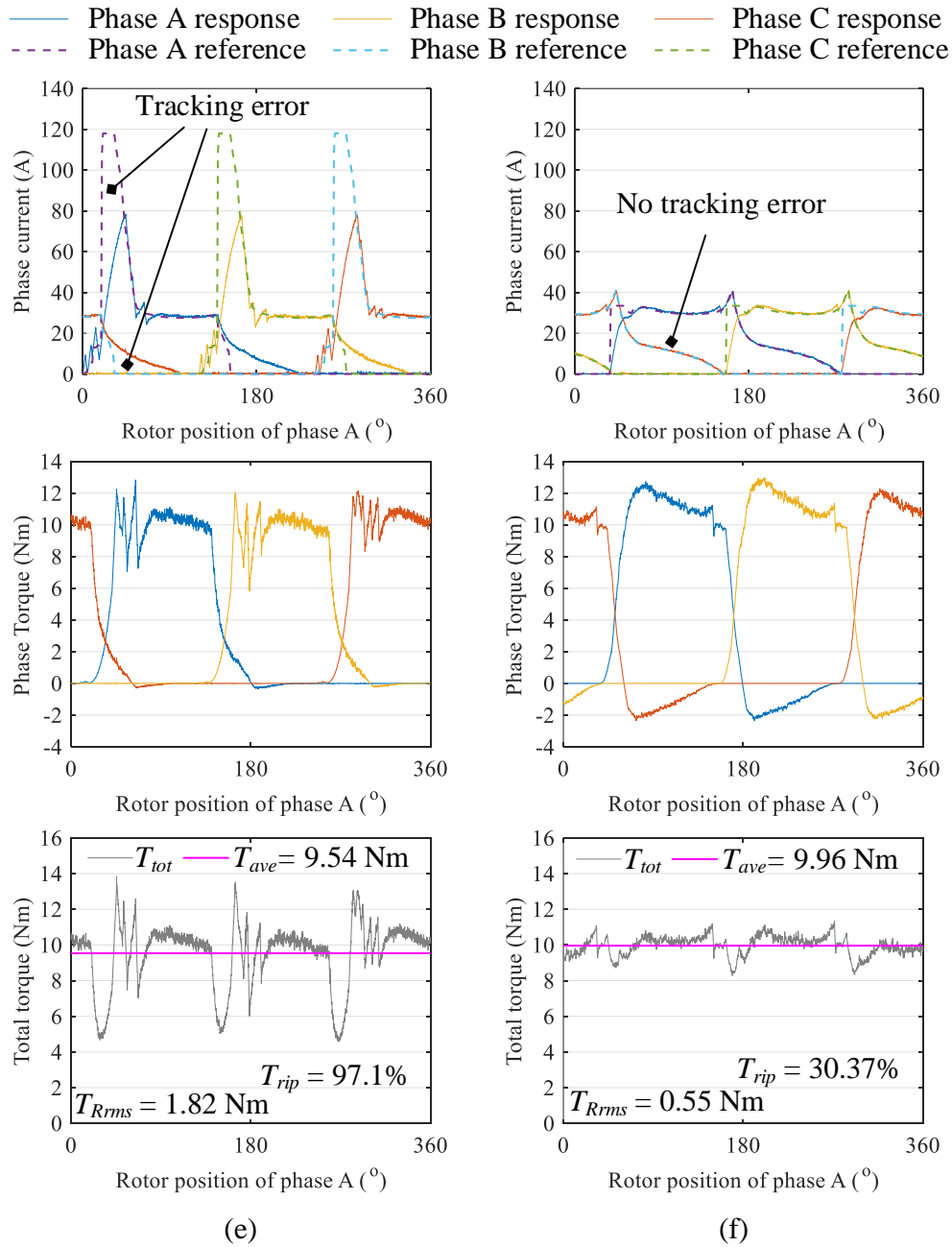
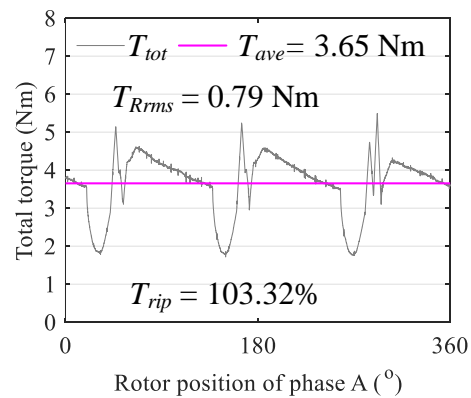
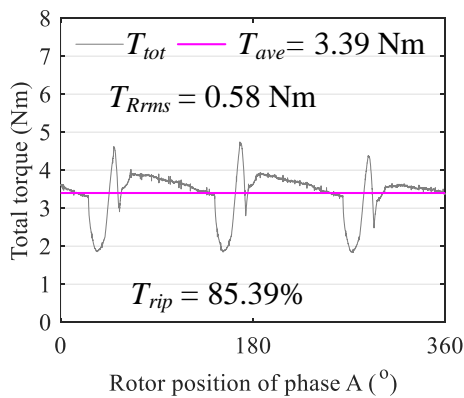
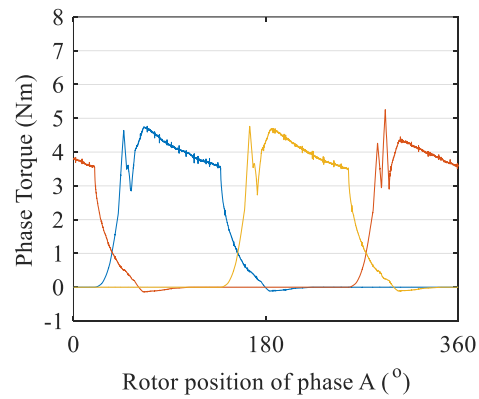
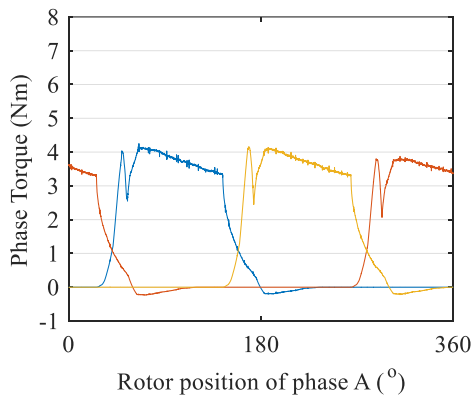
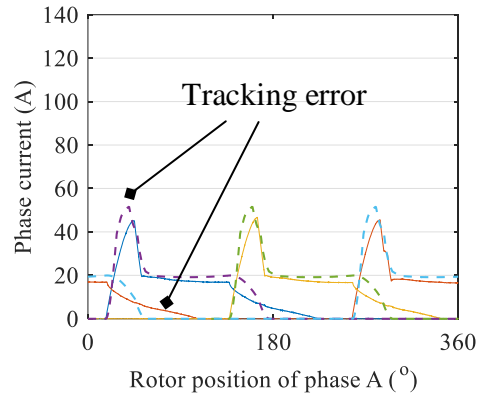
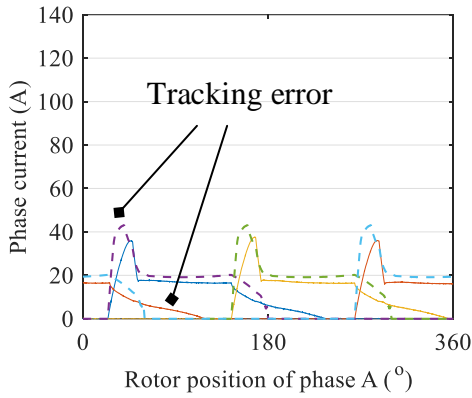


Fig. 6.12. Experimental results at 1000 r/min and 10 Nm torque reference. (a) Linear TSF,  $\theta_{on} = 29.84^{\circ}$ ,  $\theta_{ov} = 28.53^{\circ}$ . (b). Sinusoidal TSF,  $\theta_{on} = 29.18^{\circ}$ ,  $\theta_{ov} = 28.81^{\circ}$ . (c). Cubic TSF,  $\theta_{on} = 25.86^{\circ}$ ,  $\theta_{ov} = 33.91^{\circ}$ . (d). Exponential TSF,  $\theta_{on} = 31.51^{\circ}$ ,  $\theta_{ov} = 20.53^{\circ}$ . (e). TSF in [41],  $\sigma = 38.79$ . (f). Proposed online TSF,  $\theta_{on} = 36.14^{\circ}$ ,  $\theta_{off} = 163.11^{\circ}$ .

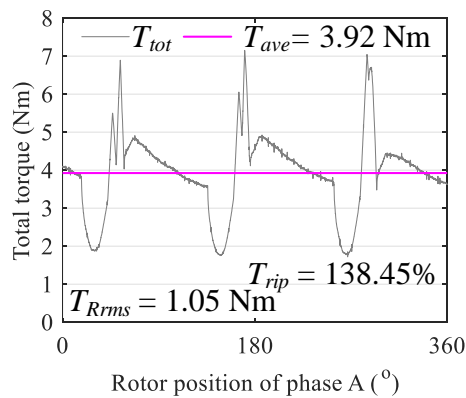
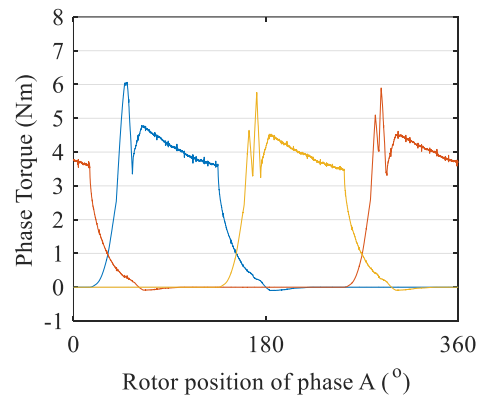
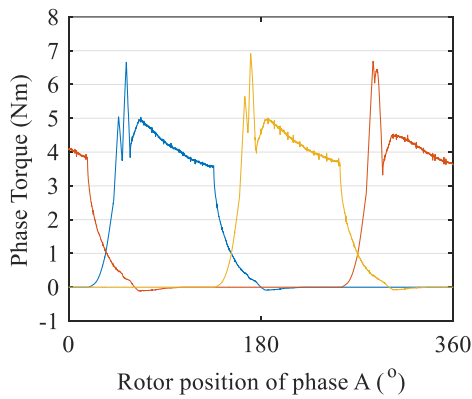
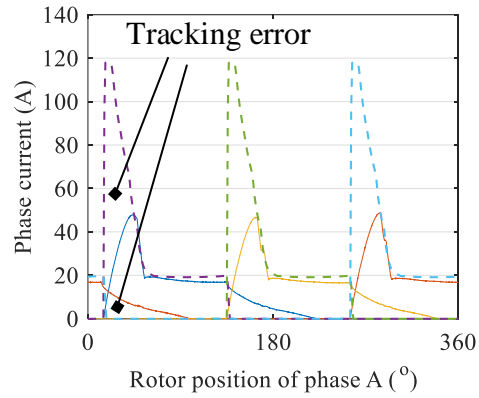
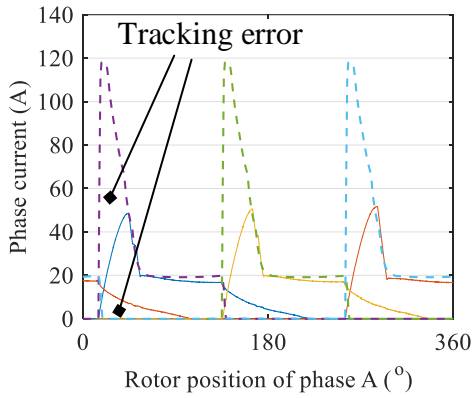
— Phase A response    — Phase B response    — Phase C response  
- - - Phase A reference    - - - Phase B reference    - - - Phase C reference



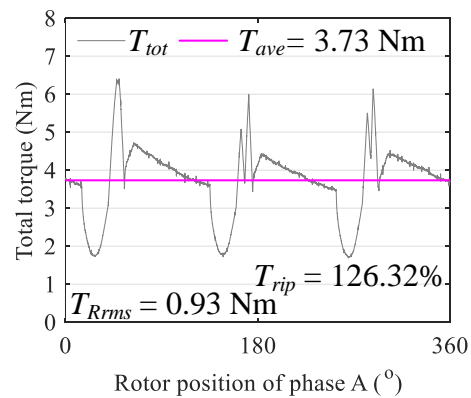
(a)

(b)

— Phase A response    — Phase B response    — Phase C response  
- - - Phase A reference    - - - Phase B reference    - - - Phase C reference



(c)



(d)

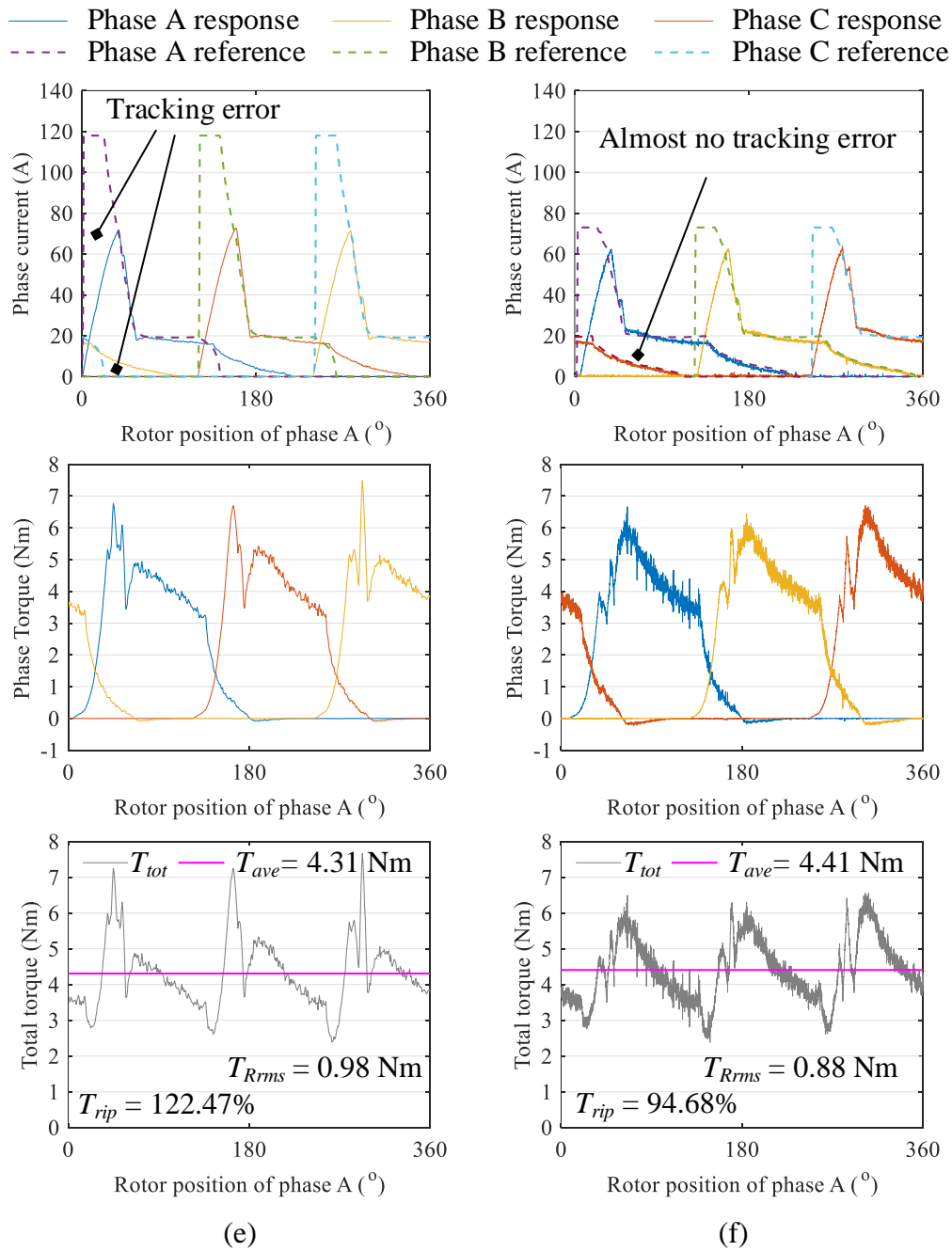


Fig. 6.13. Experimental results at 1500 r/min and 5 Nm torque reference. (a) Linear TSF,  $\theta_{on} = 24.24^\circ$ ,  $\theta_{ov} = 35.27^\circ$ . (b). Sinusoidal TSF,  $\theta_{on} = 17.49^\circ$ ,  $\theta_{ov} = 38.93^\circ$ . (c). Cubic TSF,  $\theta_{on} = 14.99^\circ$ ,  $\theta_{ov} = 3.81^\circ$ . (d). Exponential TSF,  $\theta_{on} = 15.07^\circ$ ,  $\theta_{ov} = 1.95^\circ$ . (e). TSF in [41],  $\sigma = 715.24$ . (f). Proposed online TSF,  $\theta_{on} = 5.82^\circ$ ,  $\theta_{off} = 138.89^\circ$ .

It is worth noting that for the proposed TSF at the same operating condition, the current reference generated offline in the simulation is different from the current reference generated online in the experiment. It should be noted that the dynamic SRM model used in the simulation is built using the experimentally-measured static flux linkage and torque characteristics. However, these two characteristics may vary in practical operation. In order to analyze this issue, an experiment is carried out at 1000 r/min at 10 Nm torque command, where the current reference is generated by the proposed TSF in the offline simulation. The results are shown in Fig. 6.14 and compared with the results where the current reference is generated online. It can be observed that compared to the conventional TSFs and TSF in [41] shown in Fig. 6.12(a) to (e), the proposed TSF ( $i_{ref}$  generated offline) still provides better average torque ( $T_{ave} = 10.37$  Nm) and lower torque ripple ( $T_{Rms} = 0.60$  Nm,  $T_{rip} = 39.25\%$ ). However, this performance is slightly worse than the proposed TSF when  $i_{ref}$  is generated online. As shown in Fig. 6.14(a), minor current tracking error can be observed after the turn-off angle. It means that the demagnetization current ( $i_{fall}$  in Fig. 6.5(b)) obtained by simulation is slightly different from itself obtained by experiment. This not only causes torque tracking error for the outgoing phase in the  $[\theta_{off}, \theta_{end}]$  interval, but also leads to the incorrect current reference generation for the incoming phase in the same interval. Therefore, the torque control performance may be affected. Fig. 6.14(c) shows the comparison of these two current references. It can be observed that  $i_{ref}$  generated offline is slightly larger than the  $i_{ref}$  generated online. Thus, the total output torque is also slightly higher.

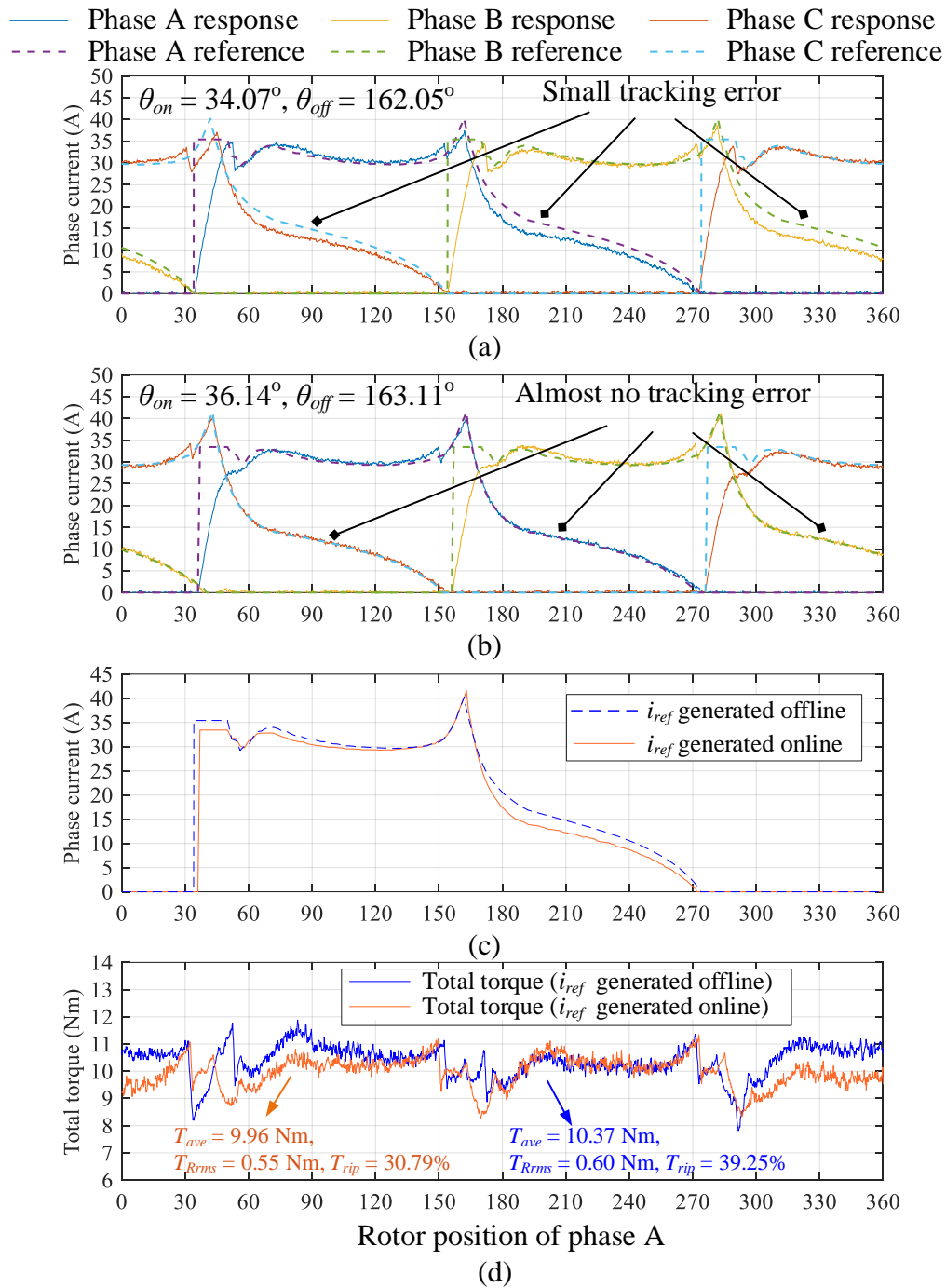


Fig. 6.14. Performance comparison at 1000 r/min and 10 Nm torque reference. (a)  $i_{ref}$  is generated offline. (b)  $i_{ref}$  is generated online. (c).  $i_{ref}$  comparison. (d) Total torque comparison.

## 6.6 Conclusion

In this chapter, a new online torque sharing function for torque ripple reduction in switched reluctance machines is provided. The proposed TSF takes the current dynamics and induced electromotive force into account by establishing a new online current profile generation technique. First, a primary phase current reference, which is derived from the torque reference, is applied when the SRM is in operation. Then, the decaying phase current after the turn-off angle is sampled and used to update the current reference. A new online optimization strategy is performed to shape the current reference during the operation of the machine, which is decoupled into two procedures to independently minimize the copper losses and torque ripple. Compared to the conventional and existing optimization-based TSFs, the proposed TSF achieves accurate torque control, improved torque-speed capability, reduced torque ripple, and better current tracking performance. Simulations and experiments are performed on a three-phase 12/8 SRM under various operating conditions to validate the proposed online TSF method.

## **Chapter 7**

### **Ripple-Free Torque-Speed**

### **Characteristic of Switched Reluctance**

### **Machines**

#### **7.1 Introduction**

The torque-speed characteristic is one of the essential properties of an electrical machine. It shows the maximum torque and maximum power that a machine can provide, which determines the application field of the machine. However, due to the high torque ripple of the SRM, the torque quality in the general torque-speed characteristic cannot be guaranteed. In this chapter, the output characteristic of an interior permanent magnet synchronous machine (IPMSM) is introduced for

comparison. Then, the torque-speed characteristics of the SRM are derived with and without considering the torque quality. The conduction angle control method, conventional TSF method, and the proposed TSF method are investigated and compared in terms of the torque-speed characteristic.

## 7.2 Torque-Speed Characteristic of IPMSMs

The torque-speed characteristic of an IPMSM can be analytically derived from the mathematical model (7.1)-(7.5), current and voltage constraints (7.6)-(7.7), and optimality criteria like maximum torque per ampere (MTPA) and maximum torque per volt (MTPV) conditions (7.8)-(7.9) [116].

$$v_d = Ri_d + \frac{d(\lambda_d + \lambda_m)}{dt} - \omega\lambda_q \quad (7.1)$$

$$v_q = Ri_q + \frac{d\lambda_q}{dt} + \omega(\lambda_d + \lambda_m) \quad (7.2)$$

$$T_e = \frac{3}{2} N_p [\lambda_m + (L_d - L_q)i_d]i_q \quad (7.3)$$

$$\lambda_d = L_d i_d \quad (7.4)$$

$$\lambda_q = L_q i_q \quad (7.5)$$

$$i_s = \sqrt{i_d^2 + i_q^2} \leq i_{\max} \quad (7.6)$$

$$v_s = \sqrt{v_d^2 + v_q^2} \leq v_{\max} \quad (7.7)$$

$$i_d + \frac{L_d - L_q}{\lambda_m} (i_d^2 - i_q^2) = 0 \quad (7.8)$$

$$i_d = -\frac{\lambda_m}{L_d} + \frac{-L_q \lambda_m + \sqrt{(L_q \lambda_m)^2 + 4L_q^2 (L_d - L_q)^2 i_q^2}}{2L_d (L_d - L_q)} \quad (7.9)$$

where  $i_d$ ,  $i_q$ ,  $u_d$ , and  $u_q$  are the currents and voltages in the  $dq$  frame, respectively;  $L_d$ ,  $L_q$ ,  $R_s$ ,  $\lambda_d$ , and  $\lambda_q$  represent the  $d$ - and  $q$ -axis stator inductances, stator winding resistance,  $d$ - and  $q$ -axis flux linkages, respectively;  $N_p$ ,  $\omega_e$ ,  $T_e$ , and  $\lambda_m$  represent the number of pole pairs, rotor electrical angular velocity, electromagnetic torque, and permanent magnet flux linkage, respectively.  $i_s$  and  $u_s$  denote the current and voltage total magnitudes, respectively;  $u_{max}$  and  $i_{max}$  denote the maximum voltage and maximum current magnitudes, respectively.

Based on the above equations (7.1)-(7.9), the  $dq$  plane and torque-speed characteristic of the IPMSM for the entire operating range can be analytically derived. For the given current limit  $i_{rated}$  as shown in Fig. 7.1 and Fig. 7.2, the maximum MTPA point  $P_{rated}$  can be found, which delivers the maximum electromagnetic torque  $T_{rated}$ . This operating point  $P_{rated}$  is the intersection of the MTPA trajectory and the current boundary. The  $i_d$  and  $i_q$  of Point  $P_{rated}$  can be derived by solving

$$\begin{cases} i_d + \frac{L_d - L_q}{\lambda_m} (i_d^2 - i_q^2) = 0 \\ i_{rated} = \sqrt{i_d^2 + i_q^2} \end{cases} \quad (7.10)$$

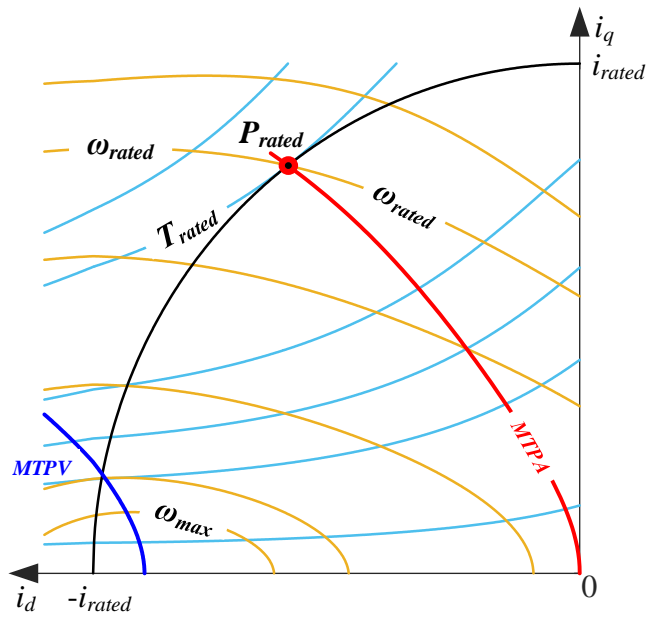


Fig. 7.1.  $dq$  plane of IPMSM.

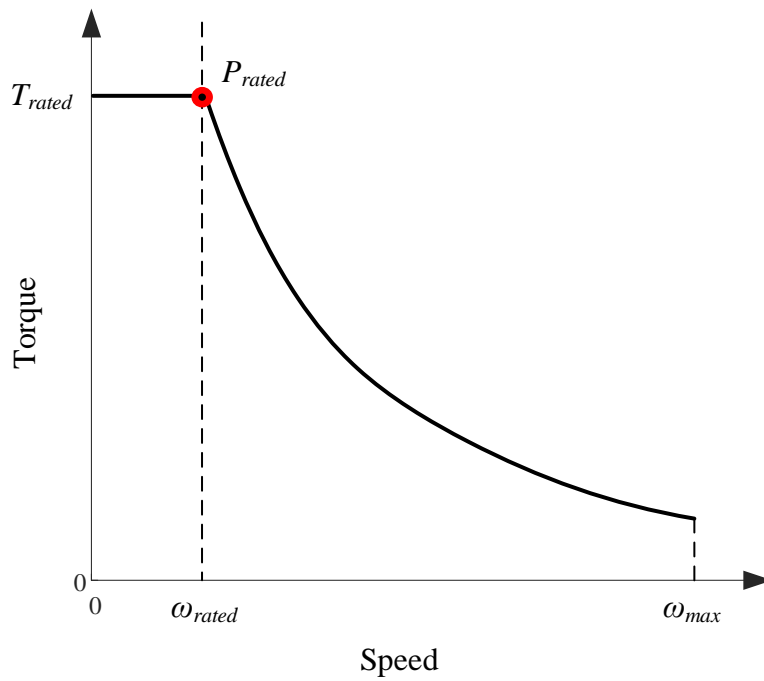


Fig. 7.2. Torque-speed characteristic of IPMSM.

### 7.3 Torque-Speed Characteristic of SRMs

Since SRMs are highly nonlinear machines, the torque-speed characteristic cannot be analytically calculated. In this thesis, the conduction angle control is used to generate the torque-speed characteristic of the SRM. For given operating speed and current reference, the turn-on and turn-off angles are optimized by GA optimization.

The optimization problem is presented as in (7.11), and the flowchart for the conduction angle optimization is shown in Fig. 7.3.

$$\begin{aligned} \min : \quad & f_1 = -T_{ave} \\ \text{Subject to} \quad & \begin{cases} -180^\circ \leq \theta_{on} \leq 180^\circ \\ -180^\circ \leq \theta_{off} \leq 180^\circ \\ \theta_{off} > \theta_{on} \end{cases} \end{aligned} \quad (7.11)$$

By solving (7.11), the optimal turn-on and turn-off angles can be found by GA, which generate maximum average torque at the given operating speed and current reference value. It should be noted that a wide range is applied to GA for searching the optimal turn-on and turn-off angles, which ensures that all the combinations of conduction angles are considered. In the optimization, the operating speed is varied from 100 r/min to 2500 r/min (maximum operating speed of the reference SRM). The constant current reference value  $I_{ref}$  is varied from 20 A to 110 A.

It is worth noting that in all simulations in this chapter, the current sampling frequency is 40 kHz, and the hysteresis current control band is 6 A. The dc-link voltage is set as 72 V.

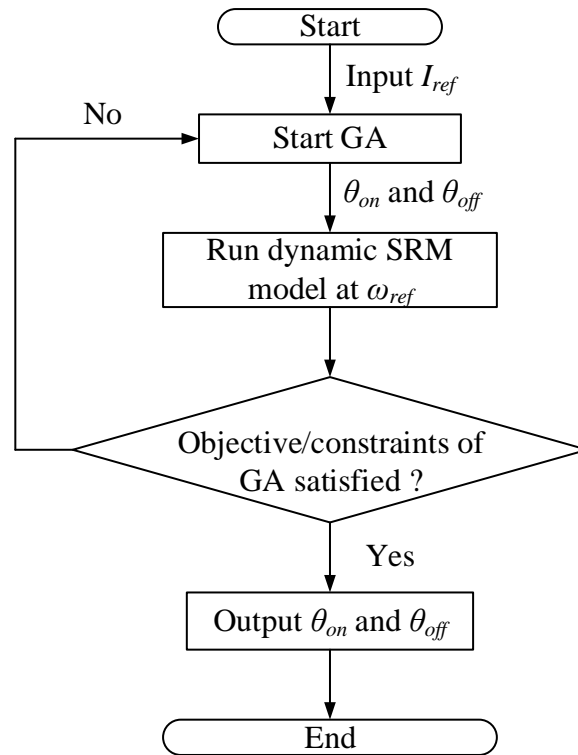
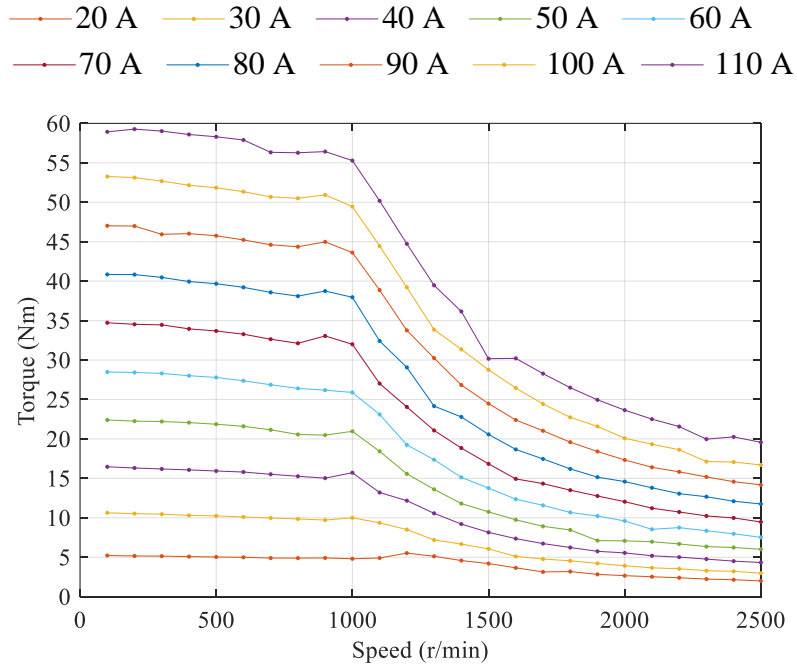
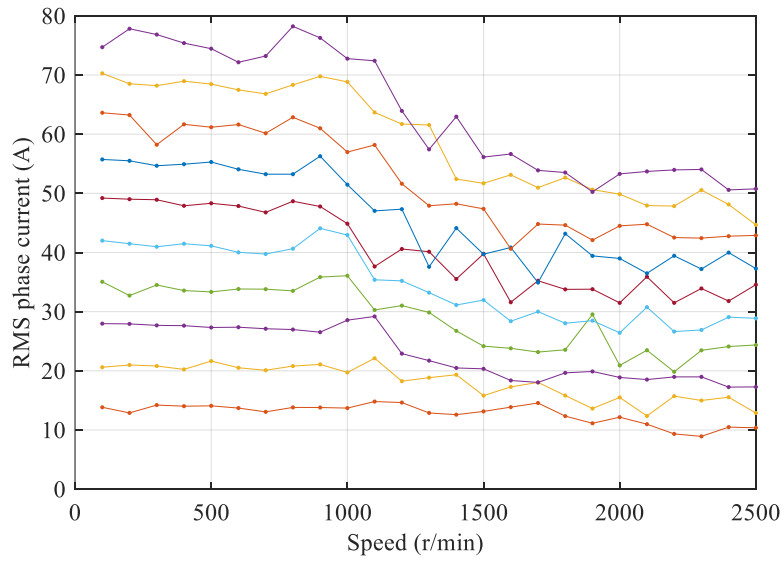


Fig. 7.3. Flowchart for the conduction angle optimization.

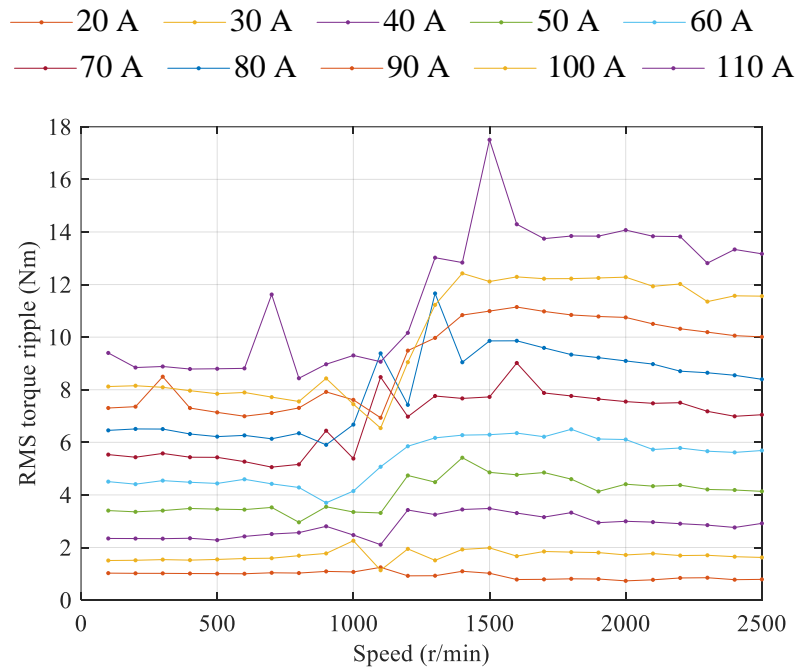
Fig. 7.4 shows the results of the above conduction angle optimization. It can be observed from Fig. 7.4(a) that the average torque,  $T_{ave}$  increases with the increase of the input current reference. For the same current reference,  $T_{ave}$  decreases with the rise of the speed, especially beyond 1000 r/min (rated speed). At the rated speed, the average torque achieves around 50 Nm when the input current reference is 100 A, which matches the SRM design specifications in Table 4.1.



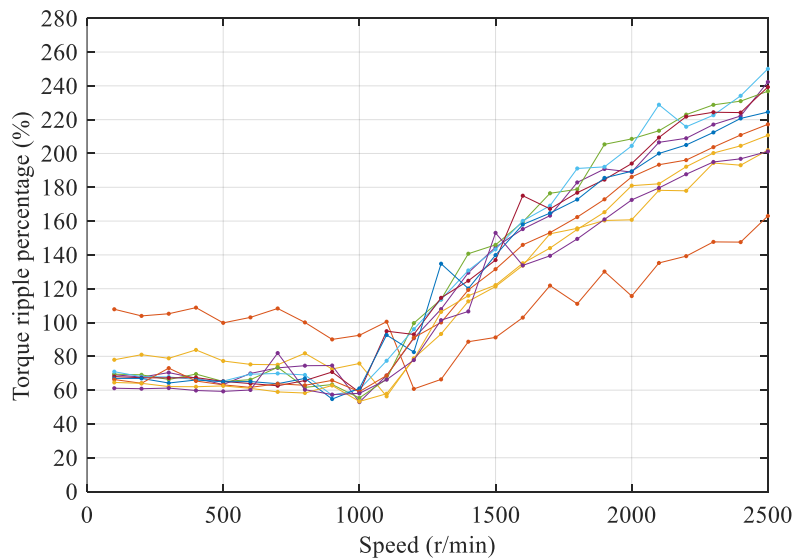
(a)



(b)



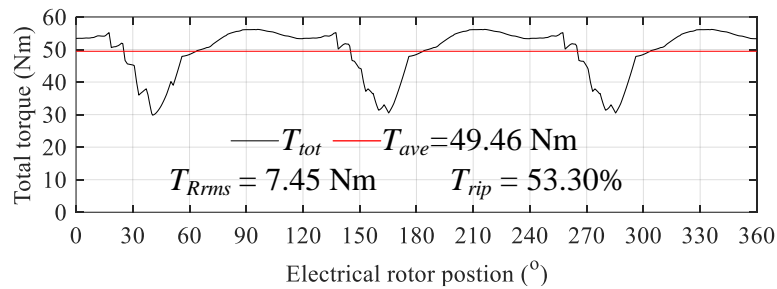
(c)



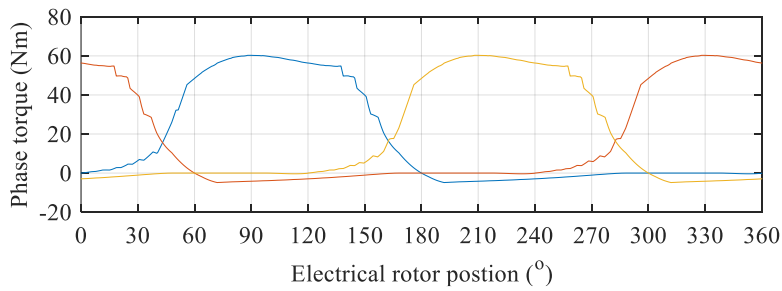
(d)

Fig. 7.4. Results of conduction angle optimization, when the objective function is  $f_1 = -T_{ave}$ . (a). Average torque. (b). RMS current. (c). RMS torque ripple. (d). Torque ripple percentage.

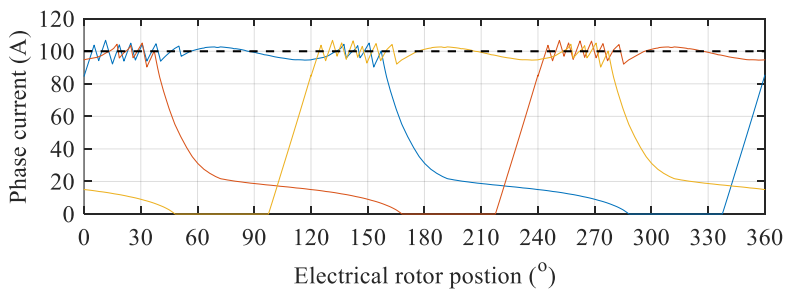
However, it can be observed from Fig. 7.4(c) and (d) that very high torque ripple are obtained, even in low-speed operation. This is because in the above GA optimization, the conduction angles are only optimized to achieve the highest average torque, and torque ripple is not taken into account. Fig. 7.5 shows the dynamic simulation results at 1000 r/min and 100 A current command. Large larger torque ripple can be observed ( $T_{Rms} = 7.45 \text{ Nm}$ ,  $T_{rip} = 53.30\%$ ).



(a)



(b)



(c)

Fig. 7.5. Dynamic simulation results at 1000 r/min and 100 A current command.

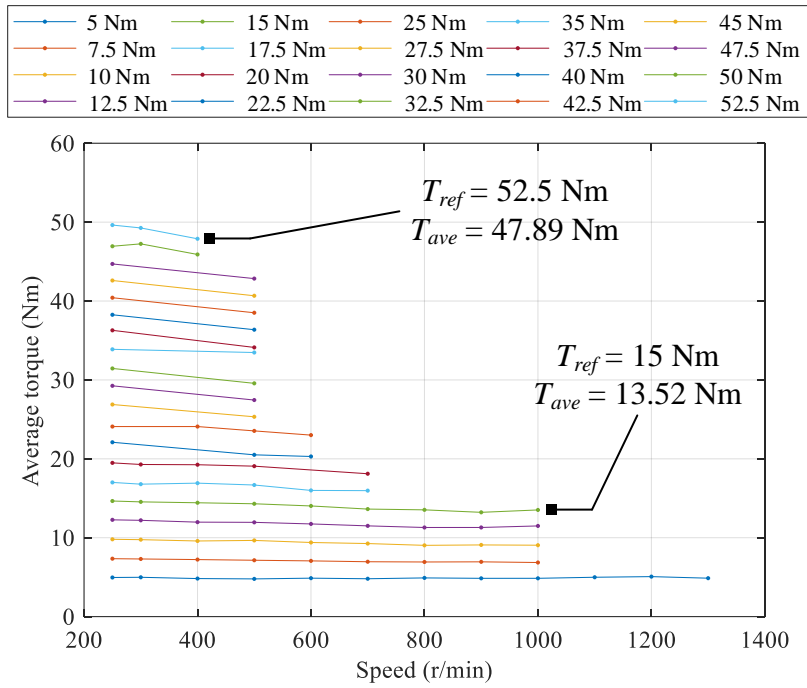
## 7.4 Ripple-Free Torque-Speed Characteristic of SRMs

By solving the optimization problem as illustrated in (7.11), the torque-speed characteristic can be obtained (Fig. 7.4(a)), and the results coincide with the design specifications of the reference SRM in Table 4.1. However, large torque ripple and poor torque quality can be found, which may not satisfy the requirement in some application fields in practice. In this thesis, the conventional cubic TSF and the proposed offline TSF are used to generate the ripple-free torque-speed characteristics of SRM. For the given torque command and operating speed, multi-objective optimization is carried out to minimize the RMS torque ripple and RMS phase current. The optimization problem for the cubic TSF and proposed offline TSF is expressed as in (7.12). The average torque needs to be larger than 90% and smaller than 110% of the reference torque.

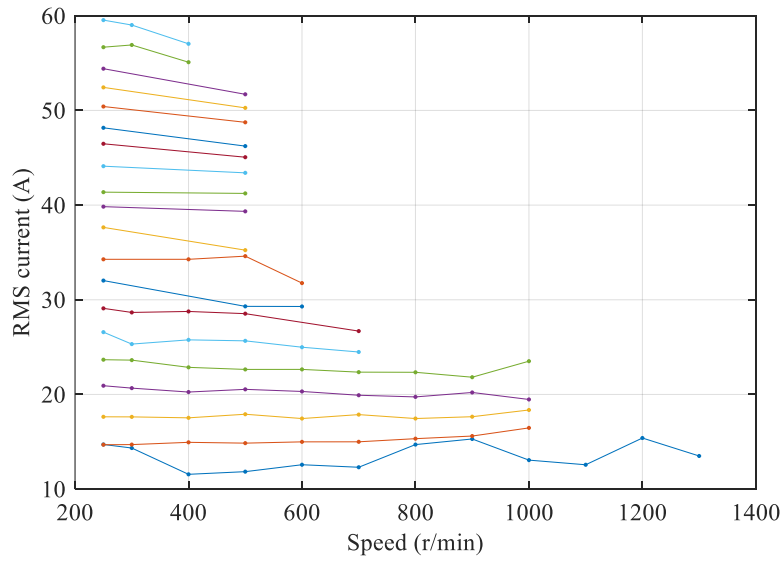
$$\begin{aligned} \min : \quad & f_2 = [T_{Rrms}, I_{rms}] \\ \text{Subject to} \quad & \left| \frac{T_{ave} - T_{ref}}{T_{ref}} \right| < 0.1 \end{aligned} \tag{7.12}$$

Fig. 7.6 and Fig. 7.7 show the optimization results for the conventional cubic TSF and proposed offline TSF, respectively. In the optimization, the torque command varies from 5 Nm to 52.5 Nm (rated torque), and the operating speed changes from 250 r/min to 2500 r/min (maximum speed). It should be noted that Fig. 7.6 and Fig. 7.7 only show the results that satisfy the torque constraint as expressed in (7.12).

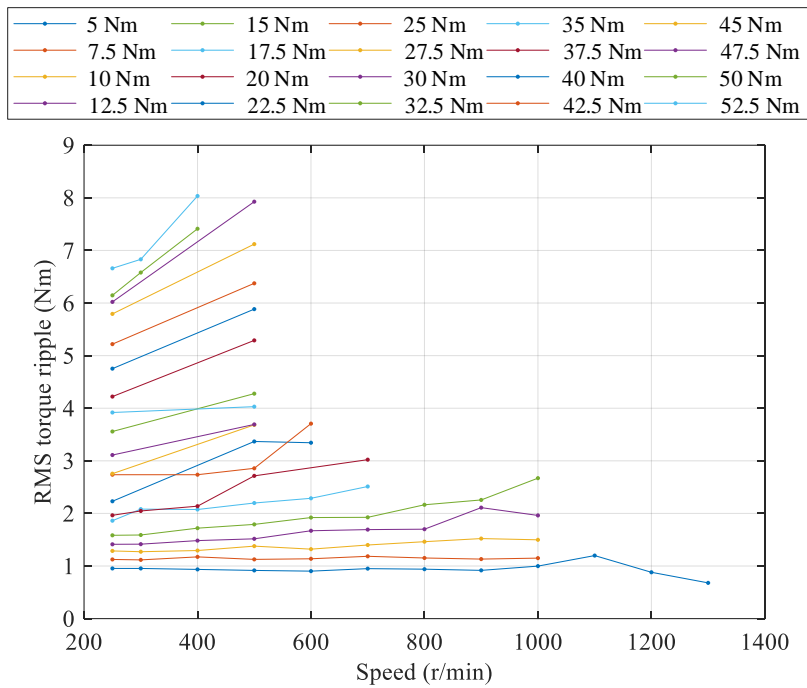
It can be observed from Fig. 7.6(a) that for the cubic TSF, the rated operating point (1000 r/min, 52.5Nm from Table 4.1) cannot be achieved. At the rated-speed (1000 r/min), the maximum average torque is around 13.52 Nm ( $T_{ref} = 15$  Nm), and the RMS torque ripple is 2.67 Nm. When the torque reference is 52.5 Nm, the maximum operating speed that satisfies that torque constraint is 400 r/min, and the average torque is 47.89 Nm. However, a very high torque ripple ( $T_{Rms} = 8.035$  Nm) is observed at this operating condition. This is similar to the results of the conduction angle optimization in Fig. 7.4, which does not consider the torque ripple minimization in the optimization.



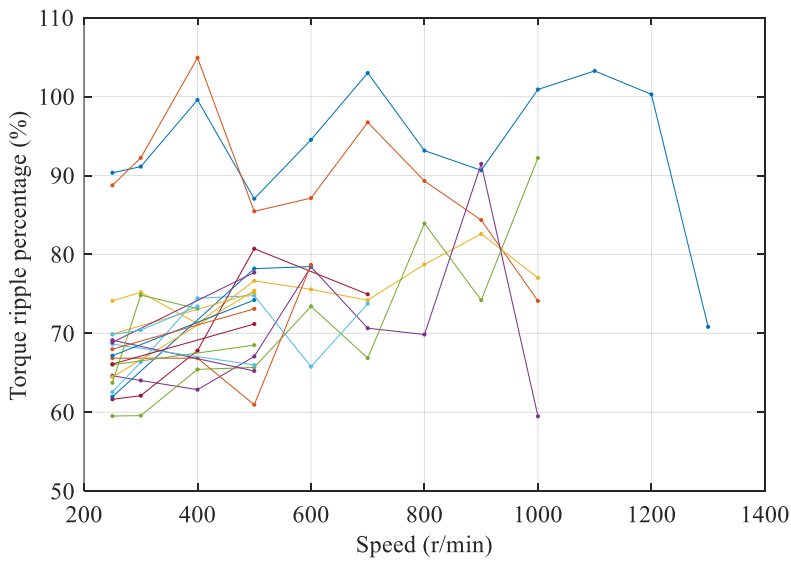
(a)



(b)



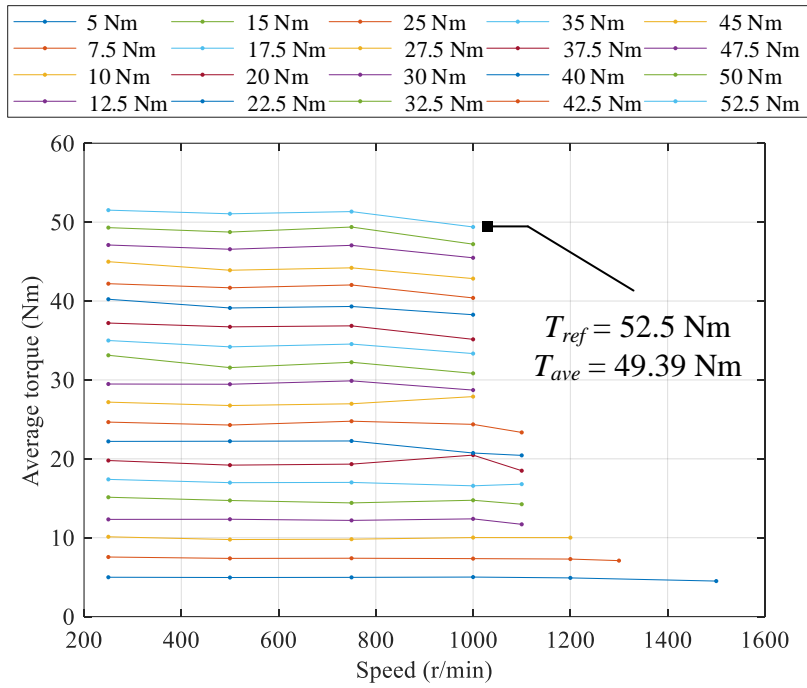
(c)



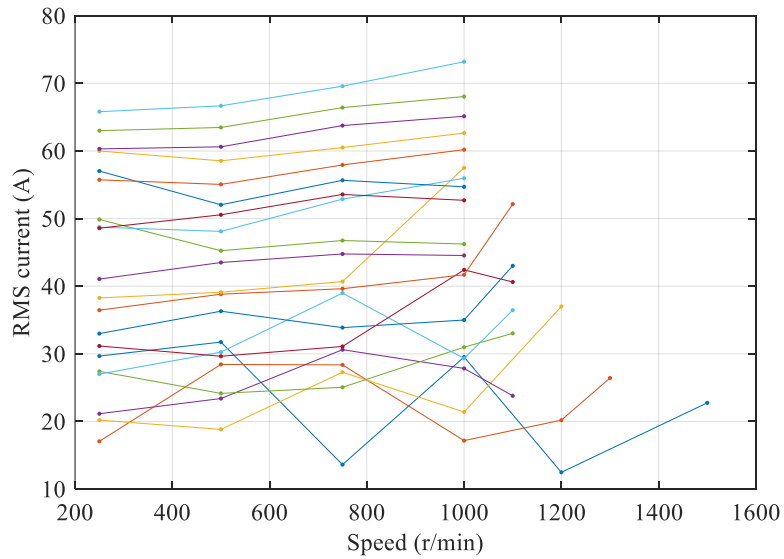
(d)

Fig. 7.6. Results of the cubic TSF optimization, when the objective function is  $f_2 = [T_{Rms}, I_{rms}]$ . (a). Average torque. (b). RMS current. (c). RMS torque ripple. (d). Torque ripple percentage.

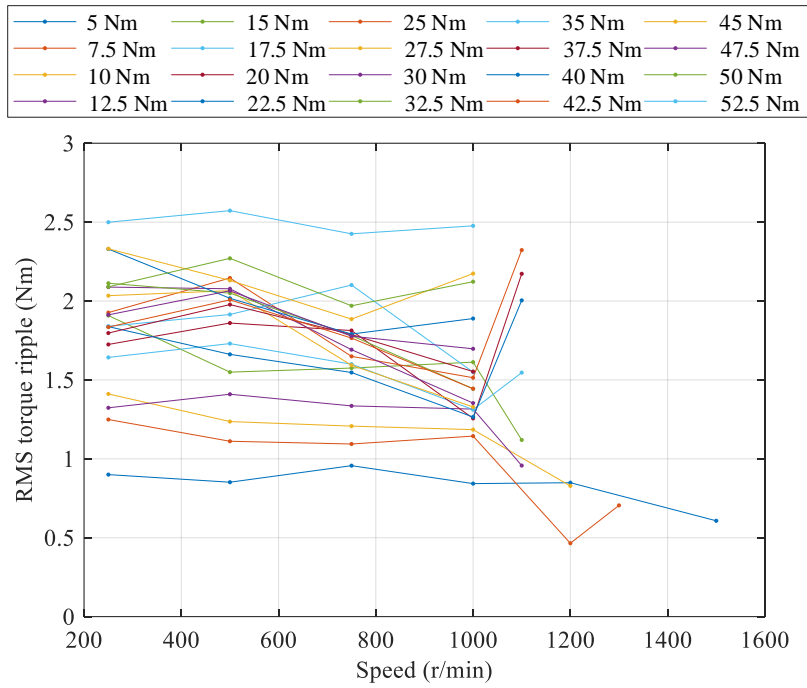
Fig. 7.7 shows the optimization results for the proposed TSF. It can be observed that the operating point (1000 r/min, 52.5Nm from Table 4.1) can be achieved. The average torque is 49.39 Nm (94.1% of 52.5 Nm) at 1000 r/min, and the torque ripple is relatively small ( $T_{Rms} = 2.48$  Nm,  $T_{rip} = 28.36\%$ ). This is owing to the current dynamics consideration in the proposed TSF method. It should be noted that all the values of the RMS torque ripple shown in Fig. 7.7 are smaller than 2.57 Nm, while the torque command varies from a low value (5 Nm) to the rated value (52.5 Nm) at the rated speed. For the high speed performance, the proposed TSF can achieve 23.34 Nm (93.30% of  $T_{ref} = 25$  Nm,  $T_{Rms} = 2.32$  Nm) at 1100 r/min, 10.01 Nm (100.10% of  $T_{ref} = 10$  Nm,  $T_{Rms} = 0.83$  Nm) at 1200 r/min, 7.10 Nm (94.7% of  $T_{ref} = 7.5$  Nm,  $T_{Rms} = 0.70$  Nm) at 1300 r/min, and 4.505 Nm (90.1% of  $T_{ref} = 5$  Nm,  $T_{Rms} = 0.61$  Nm) at 1500 r/min. Due to the higher induced voltage, it becomes harder to control the phase current with the rated DC link voltage when the speed is beyond 1000 r/min. Because the proposed TSF considers the current dynamics in the optimization, it shows better torque-speed performance.



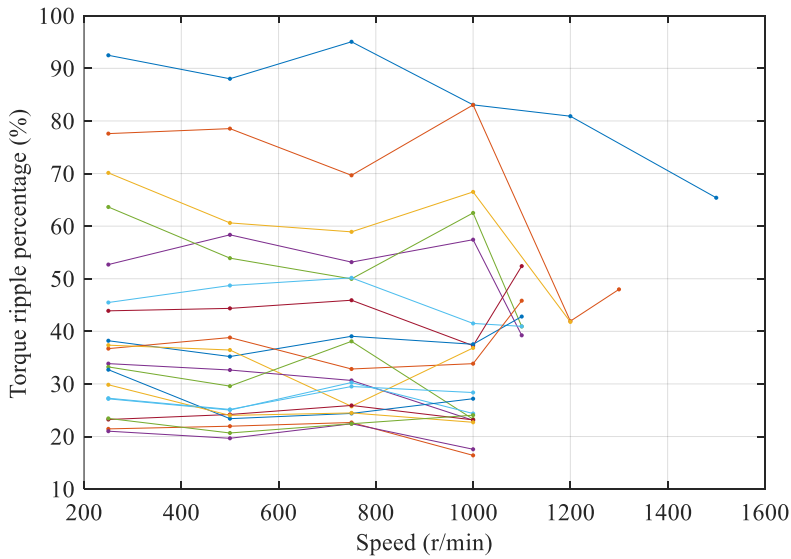
(a)



(b)

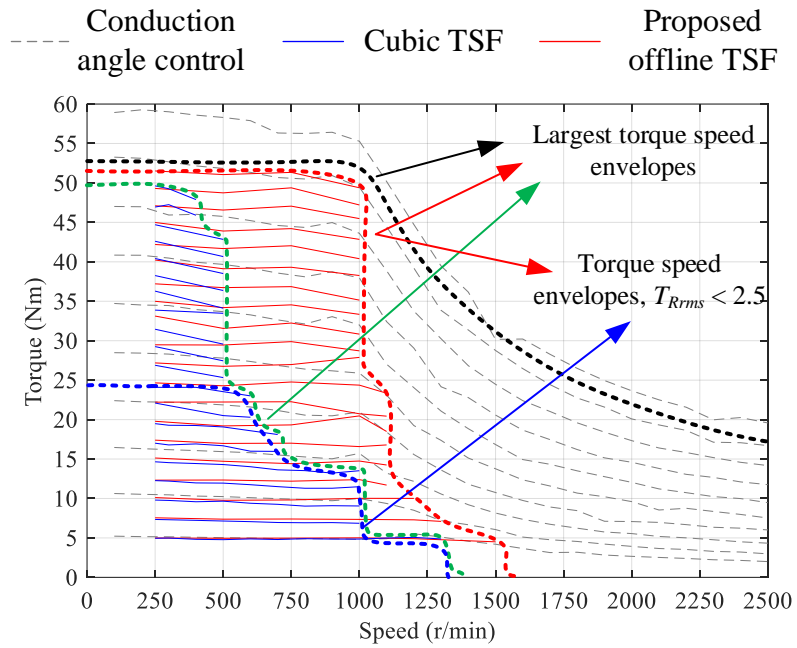


(c)

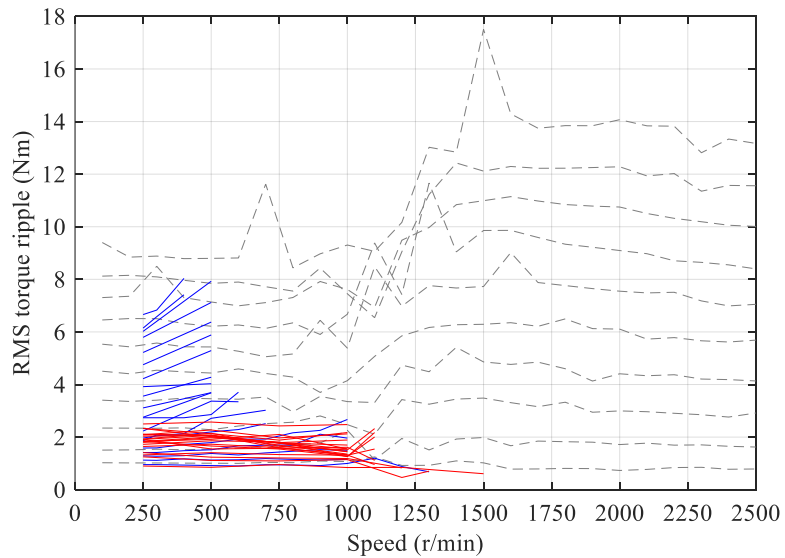


(d)

Fig. 7.7. Results of the proposed offline TSF optimization, when the objective function is  $f_2 = [T_{Rrms}, I_{rms}]$ . (a). Average torque. (b). RMS current. (c). RMS torque ripple. (d). Torque ripple percentage.



(a)



(b)

Fig. 7.8. Comparison of the torque-speed characteristics of SRMs. (a). Average torque versus speed. (b). RMS torque ripple versus speed.

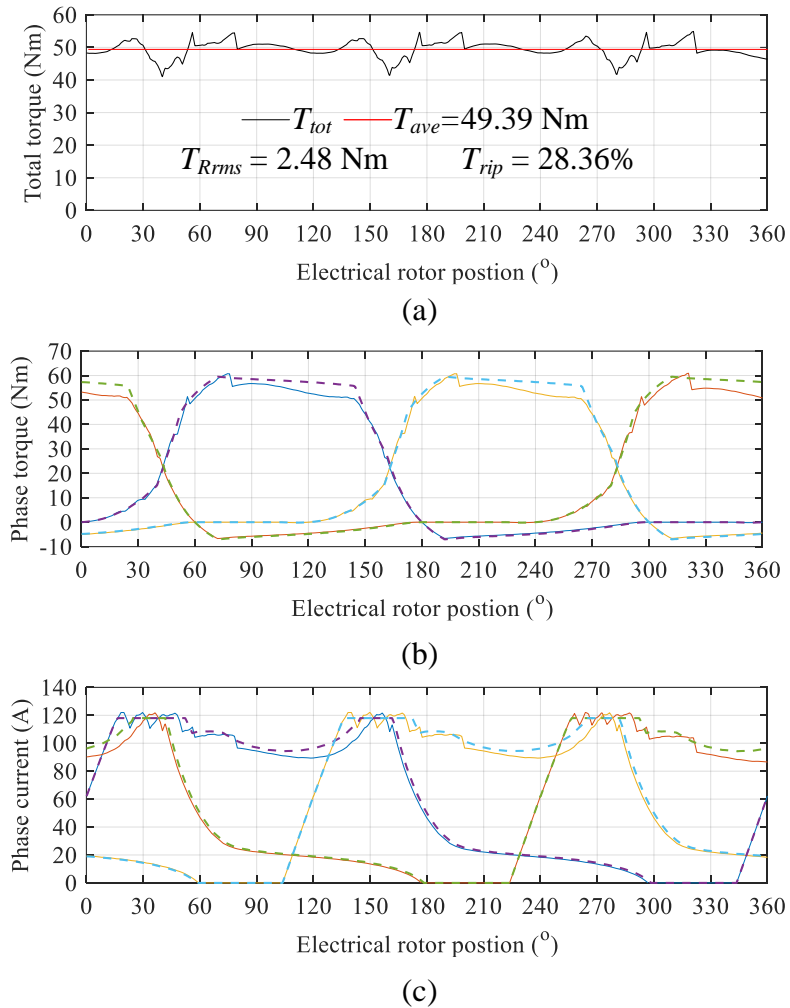


Fig. 7.9. Dynamic simulation results at 1000 r/min and 52.5 Nm torque command.

(a). Total torque. (b). Phase torque. (c). Phase current.

Fig. 7.8 shows a more intuitive comparison of the torque-speed characteristics using conduction angle control, cubic TSF, and proposed TSF. Compared to the maximum torque-speed envelop generated by the optimized conduction angle control, the proposed TSF achieves almost the same average torque with lower torque ripple below the rated-speed. Compared to the

conventional cubic TSF, the proposed TSF achieves much better torque-speed capability. At the rated-speed, the average torque generated by the proposed TSF is 3.65 times as high as that of the conventional cubic TSF. Fig. 7.9 shows the dynamic simulation results at 1000 r/min and 52.5 Nm torque command for the proposed offline TSF method.

## 7.5 Conclusion

This chapter presents the torque-speed characteristics of SRMs. Firstly, the output characteristic of an interior permanent magnet synchronous machine is introduced for comparison. Then, the torque-speed characteristics of the SRM are derived with and without considering the torque quality. The conduction angle control method, conventional TSF method, and the proposed TSF method are investigated and compared in terms of the torque-speed characteristic.

## **Chapter 8**

# **Conclusions and Future Work**

### **8.1 Conclusions**

This thesis presents advanced torque control methods for torque ripple reduction and performance improvement for switched reluctance motor (SRM) drives.

A comprehensive review of torque ripple reduction methods for switched reluctance machine drives is presented from three aspects, namely motor geometry improvements, motor drive developments, and control method developments. A comprehensive analysis of the machine dynamics and current/torque tracking performance for switched reluctance machines is presented. The drawbacks of the existing conventional and optimization-based TSFs are analyzed in detail. It is concluded that for all the existing TSF methods, the machine dynamics are not

considered or not fully considered. This is why the current tracking error may exist, which causes torque ripple.

To reduce the torque ripple in SRMs, an offline TSF method is proposed. The proposed offline TSF achieves lower current tracking error by establishing a new current reference generation strategy. The phase current reference is first derived from the torque command using offline calculations and also from the phase current response that is obtained from the dynamic model of the SRM. Then, an optimization problem is formulated to shape the current reference for the objective of minimizing the torque ripple and copper losses, while maintaining the required average output torque at the given operating speed. The dynamic simulation of the SRM model is also utilized in the optimization problem. Compared to the existing conventional and optimization-based TSFs, the proposed TSF exhibits better torque-speed performance with improved average torque and reduced torque ripple, especially during commutation.

Then an online TSF method is proposed. The proposed TSF takes the current dynamics and induced electromotive force into account by establishing a new online current profile generation technique. First, a primary phase current reference derived from the torque reference is applied to the SRM. Then, the decaying phase current after the turn-off angle is sampled and it is used to update the current reference. A new online optimization strategy is performed to shape the current reference during the operation of the machine. Owing to the proposed current profile generation technique, the optimization process is decoupled to

independently minimize the torque ripple by optimizing the turn-on angle and minimizing copper losses by optimizing the turn-off angle. Compared to the conventional TSFs and existing optimization-based TSFs, the proposed TSF achieves accurate torque control, improved torque-speed capability, reduced torque ripple, and better current tracking performance.

The torque-speed characteristics of the SRM are derived with and without considering the torque quality. The conduction angle control method, conventional TSF method, and the proposed TSF method are investigated and compared in terms of the torque-speed characteristic. Comparing to the conventional TSF, the proposed TSF achieves much better torque-speed capability. At the rated-speed, the rated torque can be achieved by the proposed TSF with a relatively low torque ripple. The average torque generated by the proposed TSF is 3.65 times as high as that of the conventional cubic TSF at the rated speed.

A new experimental setup was designed and built with an off-the-shelf 5.5 kW, 1000 r/min, 3-phase 12/8 SRM. The flux linkage-current-position and torque-current-position characteristics are experimentally-measured.

## 8.2 Future Work

This thesis proposed two TSF methods, which take the machine dynamics into account. Comparing to the existing TSFs, a better torque-speed capability is obtained. In this thesis, the torque ripple caused by the switching or current

chopping is not considered, which can be further investigated. In the simulation and experimental validations, the control frequency is set as 40 kHz. Investigations on higher control frequency or higher switching frequency can be explored.

Due to the machine dynamics consideration, low current tracking error can be observed for the proposed TSF methods. The strategy, which this thesis proposes to consider the machine dynamics, can be used to improve the current/torque tracking performance of other control methods, like the DITC method and radial force sharing method.

## Reference

- [1] A. Emadi, *Advanced Electric Drive Vehicles*, Boca Raton, FL: CRC Press, Oct. 2014.
- [2] A. Emadi, *Handbook of Automotive Power Electronics and Motor Drives*. New York, NY, USA: Marcel Dekker, May 2005.
- [3] B. Bilgin and A. Emadi, “Electric motors in electrified transportation: A step toward achieving a sustainable and highly efficient transportation system,” *IEEE Power Electron. Mag.*, vol. 1, no. 2, pp. 10–17, Jun. 2014.
- [4] B. Bilgin et al., “Making the case for electrified transportation,” *IEEE Trans. Transp. Electrific.*, vol. 1, no. 1, pp. 4–17, Jun. 2015.
- [5] A. Emadi, “Transportation 2.0,” *IEEE Power & Energy Magazine*, vol. 9, no. 4, pp. 18-29, July/August 2011.
- [6] J. Nerg, M. Rilla, V. Ruuskanen, J. Pyrhonen, and S. Ruotsalainen, “Direct-driven interior magnet permanent-magnet synchronous motors for a full electric sports car,” *IEEE Trans. Ind. Electron.*, vol. 61, no. 8, pp. 4286–4294, Aug. 2014.

- [7] S. S. Williamson, A. K. Rathore, and F. Musavi, “Industrial electronics for electric transportation: Current state-of-the-art and future challenges,” *IEEE Trans. Ind. Electron.*, vol. 62, no. 5, pp. 3021–3032, May 2015.
- [8] X. Liu, H. Chen, J. Zhao, and A. Belahcen, “Research on the performances and parameters of interior PMSM used for electric vehicles”, *IEEE Trans. Ind. Electron.* vol. 63, no. 6, pp. 3533-3545, Feb. 2016.
- [9] K. D. Hoang and H. K. A. Aorith, “Online control of IPMSM drives for traction applications considering machine parameter and inverter nonlinearities,” *IEEE Trans. Transp. Electrification.*, vol. 1, no. 4, pp. 312–325, Dec. 2015.
- [10] H. Ge, Y. Miao, B. Bilgin, B. Nahid-Mobarakeh, and A. Emadi, “Speed range-extended maximum torque per ampere control for PM drives considering inverter and motor nonlinearities,” *IEEE Trans. Power Electron.*, vol. 32, no. 9, pp. 7151–7159, Sept. 2017.
- [11] L. Chen, R. Davis, S. Stella, T. Tesch, and A. Fischer-Antze, “Improved control techniques for IPM motor drives on vehicle application,” in *Conf. Rec. IEEE-IAS Annu. Meeting*, 2002, pp. 2051–2056.
- [12] K. Kiyota and A. Chiba, “Design of switched reluctance motor competitive to 60-kW IPMSM in third-generation hybrid electric vehicle,” *IEEE Trans. Ind. Appl.*, vol. 48, no. 6, pp. 2303–2309, 2012.

- [13] K. Kiyota, T. Kakishima, H. Sugimoto, and A. Chiba, “Comparison of the test result and 3D-FEM analysis at the knee point of a 60 kW SRM for a HEV,” *IEEE Trans. Magn.*, vol. 49, no. 5, pp. 2291–2294, May 2013.
- [14] K. Kiyota, T. Kakishima, and A. Chiba, “Comparison of test result and design stage prediction of switched reluctance motor competitive with 60-kW rare-earth PM motor,” *IEEE Trans. Ind. Electron.*, vol. 61, no. 10, pp. 5712–5721, Oct. 2014.
- [15] B. Bilgin, A. Emadi, and M. Krishnamurthy, “Design considerations for switched reluctance machines with a higher number of rotor poles,” *IEEE Trans. Ind. Electron.*, vol. 59, no. 10, pp. 3745–3756, Oct. 2012.
- [16] Y. Yang, N. Schofield, and A. Emadi, “Double-rotor switched reluctance machine (DRSRM),” *IEEE Trans. Energy Convers.*, vol. 30, no. 2, pp. 671–680, Jun. 2015.
- [17] J. W. Jiang, B. Bilgin, and A. Emadi, “Three-phase 24/16 switched reluctance machine for a hybrid electric powertrain,” *IEEE Trans. Transport. Electrific.*, vol. 3, no. 1, pp. 76–85, Mar. 2017.
- [18] S. M. Castano, R. Yang, C. Mak, B. Bilgin, and A. Emadi, “External-rotor switched reluctance motor for direct-drive home appliances,” in *Proc. 44th Annu. Conf. IEEE Ind. Electron. Soc. (IECON)*, Oct. 2018, pp. 514–521.
- [19] J. Kim and R. Krishnan, “Novel two-switch-based switched reluctance motor drive for low-cost high-volume applications,” *IEEE Trans. Ind. Appl.*, vol. 45, no. 4, pp. 1241–1248, Jul./Aug. 2009.

- [20] U. Jakobsen, K. Lu, P. O. Rasmussen, D. H. Lee, and J. W. Ahn, “Sensorless control of low-cost single-phase hybrid switched reluctance motor drive,” *IEEE Trans. Ind. Appl.*, vol. 51, no. 3, pp. 2381–2387, May/Jun. 2015.
- [21] M. M. Namazi, S. M. Saghaian Nezhad, A. Tabesh, A. Rashidi, and M. Liserre, “Passivity-based control of switched reluctance-based wind system supplying constant power load,” *IEEE Trans. Ind. Electron.*, vol. 65, no. 12, pp. 9550–9560, Dec. 2018.
- [22] D. Panda and V. Ramanarayanan, “Reduced acoustic noise variable dc-bus-voltage-based sensorless switched reluctance motor drive for HVAC applications,” *IEEE Trans. Ind. Electron.*, vol. 54, no. 4, pp. 2065–2078, Aug. 2007.
- [23] C. Gan, Q. Sun, J. Wu, C. Shi, and Y. Hu, “A universal two-sensor current detection scheme for current control of multiphase switched reluctance motors with multiphase excitation,” *IEEE Trans. Power Electron.*, vol. 34, no. 2, pp. 1526–1539, Feb. 2019.
- [24] Y.-C. Wu, W.-T. Tseng, and Y.-T. Chen, “Torque ripple suppression in an external-meshed magnetic gear train,” *Adv. Mech. Eng.*, vol. 5, Jan. 2013, Art. ID 178909.
- [25] S. M. Castano, B. Bilgin, E. Fairall, and A. Emadi, “Acoustic noise analysis of a high-speed high-power switched reluctance machine: Frame effects,” *IEEE Trans. Energy Convers.*, vol. 31, no. 1, pp. 69–77, Mar. 2016.

- [26] A. M. Omekanda, “Switched reluctance machines for EV and HEV propulsion: State-of-the-art,” in *Proc. IEEE Workshop Elect. Mach. Design Control Diagnosis*, Paris, France, Mar. 2013, pp. 70–74.
- [27] X. Xue, K. Cheng, and S. Ho, “Optimization and evaluation of torque sharing functions for torque ripple minimization in switched reluctance motor drives,” *IEEE Trans. Power Electron.*, vol. 24, no. 9, pp. 2076–2090, Sep. 2009.
- [28] H. S. Ro, H. G. Jeong, K. G. Lee, J. S. Lee, and K. B. Lee, “Torque ripple minimization scheme using torque sharing function based fuzzy logic control for a switched reluctance motor,” *J. Electr. Eng. Technol.*, vol. 10, no. 1, pp. 118–127, Jan. 2015.
- [29] X. D. Xue and K. W. E. Cheng, “A control scheme of torque ripple minimization for SRM drives based on flux linkage controller and torque sharing function,” in *Proc. Int. Conf. Power Electron. Syst. Appl.*, Hong Kong, 2006, pp. 79–84.
- [30] D.-H. Lee, S.-Y. Ahn, J.-W. Ahn, and J.-M. Kim, “Modified TSF for the high speed switched reluctance motor,” in *Proc. IEEE Int. Symp. Ind. Electron.*, Gdansk, Poland, Jun. 2011, pp. 655–660.
- [31] M. Dowlatshahi, S. M. S. Nejad, and J. W. Ahn, “Torque ripple minimization of switched reluctance motor using modified torque sharing function,” in *Proc. Iranian Conf. Elect. Eng.*, Mashhad, Iran, 2013, pp. 1–6.

- [32] S. Mousavi-Aghdam, A. Moradi, and A. Dolatkah, “Torque ripple reduction of switched reluctance motor using improved torque sharing functions,” in *Proc. Iranian Conf. Elect. Eng.*, Tehran, Iran, May 2017, pp. 1043–1047.
- [33] H.-U. Shin, K. Park, and K.-B. Lee, “A non-unity torque sharing function for torque ripple minimization of switched reluctance generators in wind power systems,” *Energies*, vol. 8, no. 10, pp. 11685–11701, 2015.
- [34] T. Kojima and R. W. De Doncker, “Optimal torque sharing in direct instantaneous torque control of switched reluctance motors,” in *Proc. IEEE Energy Convers. Congr. Expo.*, Montreal, Canada, Sep. 2015, pp. 327–333.
- [35] C. Choi, S. Kim, Y. Kim, and K. Park, “A new torque control method of a switched reluctance motor using a torque-sharing function,” *IEEE Trans. Magn.*, vol. 38, no. 5, pp. 3288–3290, Sep. 2002.
- [36] D. H. Lee, J. Liang, Z. G. Lee, and J. W. Ahn, “A Simple nonlinear logical torque sharing function for low-torque ripple SR drive,” *IEEE Trans. Ind. Electron.*, vol. 56, no. 8, pp. 3021–3028, Aug. 2009.
- [37] R. Mikail, I. Husain, Y. Sozer, M. S. Islam, and T. Sebastian, “Torque ripple minimization of switched reluctance machines through current profiling,” *IEEE Trans. Ind. Appl.*, vol. 49, no. 3, pp. 1258–1267, May/Jun. 2013.
- [38] A.-C. Pop, V. Petrus, C. Martis, V. Iancu, and J. Gyselinck, “Comparative study of different torque sharing functions for losses minimization in switched reluctance motors used in electric vehicles propulsion,” in *Proc. Conf. Rec. Optim. Electr. Electron. Equip.*, Brasov, Romania, May 2012, pp. 356–365.

- [39] V. P. Vujić, “Minimization of torque ripple and copper losses in switched reluctance drive,” *IEEE Trans. Power Electron.*, vol. 27, no. 1, pp. 388–399, Jan. 2012.
- [40] J. Ye, B. Bilgin, and A. Emadi, “An offline torque sharing function for torque ripple reduction in switched reluctance motor drives,” *IEEE Trans. Energy Convers.*, vol. 30, no. 2, pp. 726–735, Jun. 2015.
- [41] H. Li, B. Bilgin, and A. Emadi, “An improved torque sharing function for torque ripple reduction in switched reluctance machines,” *IEEE Trans. Power Electron.*, vol. 34, no. 2, pp. 1635–1644, Feb. 2019.
- [42] B. Li, X. Ling, Y. Huang, L. Gong, and C. Liu, “Multiphysics modeling and optimal current profiling for switched reluctance machine drive,” in *Proc. Annu. Conf. IEEE Ind. Electron. Soc.*, Washington, USA, Oct. 2018, pp. 595–600.
- [43] L. Ge, I. Ralev, A. K. Hessling, S. Song, and R. W. D. Doncker, “A simple reluctance calibration strategy to obtain the flux-linkage characteristics of switched reluctance machines,” *IEEE Trans. Power Electron.* vol. 35, no. 3, pp. 2787–2798, Mar. 2020.
- [44] C. E. Carstensen, N. H. Fuengwarodsakul, and R. W. De Doncker, “Flux linkage determination for correct modeling of switched reluctance machines—Dynamic measurement versus static computation,” in *Proc. IEEE Int. Electr. Mach. Drives Conf.*, May 2007, vol. 2, pp. 1317–1323.

- [45] S. Yao and W. Zhang, “A simple strategy for parameters identification of SRM direct instantaneous torque control,” *IEEE Trans. Power Electron.*, vol. 33, no. 4, pp. 3622–3630, Apr. 2018.
- [46] C. Gan, Q. Sun, Y. Hu, J. Wu, S. Yang, and L. Jin, “Low-cost direct instantaneous torque control for switched reluctance motors with bus current detection under soft-chopping mode,” *IET Power Electron.*, vol. 9, no. 3, pp. 482–490, Mar. 2016.
- [47] Y. Sozer and D.A. Torrey, “Optimal turn-off angle control in the face of automatic turn-on angle control for switched-reluctance motors,” *IET Elect. Power Appl.*, vol. 1, no. 3, pp. 395–401, May 2007.
- [48] K. W. Hu, Y. Y. Chen, and C. M. Liaw, “A reversible position sensorless controlled switched-reluctance motor drive with adaptive and intuitive commutation tunings,” *IEEE Trans. Power Electron.*, vol. 30, no. 7, pp. 3781–3793, Jul. 2015.
- [49] Q. Sun, J. Wu and C. Gan, “Optimized direct instantaneous torque control for SRMs with efficiency improvement,” *IEEE Trans. Ind. Electron.*, Early Access, DOI: 10.1109/TIE.2020.2975481.
- [50] S. Song, G. Fang, R. Hei, J. Jiang, R. Ma, and W. Liu, “Torque ripple and efficiency online optimization of switched reluctance machine based on torque per ampere characteristics,” *IEEE Trans. Power Electron.*, Early Access, DOI: 10.1109/TPEL.2020.2974662.

- [51] H. N. Husain, K. W. Hu, and Y. W. Wu, “A current control scheme with back EMF cancellation and tracking error adapted commutation shift for switched-reluctance motor drive,” *IEEE Trans. Ind. Electron.*, vol. 63, no. 12, pp. 7381–7392, Dec. 2016.
- [52] S. K. Sahoo, S. K. Panda, and J. Xu, “Indirect torque control of switched reluctance motors using iterative learning control,” *IEEE Trans. Power Electron.*, vol. 20, no. 1, pp. 200–208, Jan. 2005.
- [53] S. K. Sahoo, S. K. Panda, and J. Xu, “Iterative learning-based high-performance current controller for switched reluctance motors,” *IEEE Trans. Energy Convers.*, vol. 19, no. 3, pp. 491–498, Sep. 2004.
- [54] J. Ye, B. Bilgin, and A. Emadi, “An extended-speed low-ripple torque control of switched reluctance motor drives,” *IEEE Trans. Power Electron.*, vol. 30, no. 3, pp. 1457–1470, Mar. 2015.
- [55] R. Hari Krishnan and F. M. Fernandez, “Improved online torque-sharing-function based low ripple torque control of switched reluctance motor drives,” in *Proc. IEEE Int. Conf. Power Electron., Drives Energy Syst*, Dec. 2016, pp. 1–6.
- [56] J. Kim, K. Ha, and R. Krishnan, “Single-controllable-switch-based switched reluctance motor drive for low cost, variable-speed applications,” *IEEE Trans. Power Electron.*, vol. 27, no. 1, pp. 379–387, Jan. 2012.

- [57] X. D. Xue, K. W. E. Cheng, and Y. J. Bao, “Control and integrated half bridge to winding circuit development for switched reluctance motors,” *IEEE Trans. Ind. Inf.*, vol. 10, no. 1, pp. 109–116, Feb. 2014.
- [58] S. Song, Z. Xia, Z. Zhang, and W. Liu, “Control performance analysis and improvement of a modular power converter for three-phase SRM with Y-connected windings and neutral line,” *IEEE Trans. Ind. Electron.*, vol. 63, no. 10, pp. 6020–6030, Oct. 2016.
- [59] M. Barnes and C. Pollock, “Power electronic converters for switched reluctance drives,” *IEEE Trans. Power Electron.*, vol. 13, no. 6, pp. 1100–1111, Nov. 1998.
- [60] R. Krishnan and P. N. Materu, “Design of a single-switch-per-phase converter for switched reluctance motor drives,” *IEEE Trans. Ind. Electron.*, vol. 37, no. 6, pp. 469–476, Dec. 1990.
- [61] P. C. Desai, M. Krishnamurthy, N. Schofield, and A. Emadi, “Novel switched reluctance machine configuration with higher number of rotor poles than stator poles: Concept of implementation,” *IEEE Trans. Ind. Electron.*, vol. 57, no. 2, pp. 649–659, Feb. 2010.
- [62] J. Zhu, K. W. Cheng, and X. Xue, “Torque analysis for in-wheel switched reluctance motors with varied number of rotor poles,” in *Proc. Int. Symp. Elect. Eng.*, Hong Kong, Dec. 2016, pp. 1–5.

- [63] H. Bechaouech, A. V. D. Bosshe and M. N. Ibrahim, “Comparison between 12/8 and 12/16 combinations of switched reluctance machine,” in *Proc. Eur. Conf. Electr. Eng. Comput. Sci.*, Bern, Switzerland, Dec. 2018, pp. 174–177.
- [64] X. Sun, K. Diao, G. Lei, Y. Guo, and J. Zhu, “Study on segmented rotor switched reluctance motors with different rotor pole numbers for BSG system of hybrid electric vehicles,” *IEEE Trans. Veh. Technol.* vol. 68, no. 6, Jun. 2019.
- [65] F. Sahin, H. B. Ertan, and K. Leblebicioglu, “Optimum geometry for torque ripple minimization of switched reluctance motors,” *IEEE Trans. Energy Convers.*, vol. 15, no. 1, pp. 30–39, Mar. 2000.
- [66] N. K. Sheth and K. R. Rajagopal, “Optimum pole arcs for a switched reluctance motor for higher torque with reduced ripple,” *IEEE Trans. Magn.*, vol. 39, no. 5, pp. 3214–3216, Sep. 2003.
- [67] R. Arumugam, J. F. Lindsay, and R. Krishnan, “Sensitivity of pole arc/pole pitch ratio on switched reluctance motor performance,” in *Proc. IEEE IAS Annu. Meeting*, Oct. 1988, vol. 1, pp. 50–54.
- [68] Y. K. Choi, H. S. Yoon, and C. S. Koh, “Pole-shape optimization of a switched reluctance motor for torque ripple reduction,” *IEEE Trans. Magn.*, vol. 43, no. 4, pp. 1797–1800, Apr. 2007.
- [69] C. Sahin, A. E. Amac, M. Karacor, and A. Emadi, “Reducing torque ripple of switched reluctance machines by relocation of rotor moulding clinches,” *IET Elect. Power Appl.*, vol. 6, pp. 753–760, 2012.

- [70] Z. Xia and J. Bauman, “An Integrated modular converter for switched reluctance motor drives in range-extended electric vehicles,” in *Proc. IEEE Transp. Electrific. Conf. Expo*, Detroit, USA, Jun. 2019, pp. 1–6.
- [71] M. Ma, Z. Chang, Y. Hu, F. Li, C. Gan, and W. Cao, “An integrated switched reluctance motor drive topology with voltage-boosting and on-board charging capabilities for plug-in hybrid electric vehicles (PHEVs),” *IEEE Access*, vol. 6, pp. 2169–3536, Feb. 2018.
- [72] F. Yi and W. Cai, “Modeling, control, and seamless transition of the bidirectional battery-driven switched reluctance motor/generator drive based on integrated multiport power converter for electric vehicle applications” *IEEE Trans. Power Electron.*, vol. 31, no. 10, pp. 7099–7111, Oct. 2016.
- [73] S. R. K. Huseini, E. Farjah, N. Tashakor, and T. Ghanbari, “Development of an integrated switched-reluctance motor drive with battery charging capability for electric vehicle propulsion system,” in *Proc. 6th PEDSTC*, Feb. 3–4, 2015, pp. 579–584.
- [74] Y. Hu, X. Song, W. Cao, and B. Ji, “New SR drive with integrated charging capacity for plug-in hybrid electric vehicles (PHEVs),” *IEEE Trans. Ind. Electron.*, vol. 61, no. 10, pp. 5722–5731, Oct. 2014.
- [75] Q. Sun, J. Wu, C. Gan, and J. Wang, “A novel boost chopper converter-based torque sharing function control strategy for switched reluctance motors,” in *Proc. Inter. Conf. Elect. Mach. Syst.*, Sydney, Australia, Aug. 2017, pp. 1–6.

- [76] C. Gan, J. Wu, Y. Hu, S. Yang, W. Cao, and J. M. Guerrero, “New integrated multilevel converter for switched reluctance motor drives in plug-in hybrid electric vehicles with flexible energy conversion,” *IEEE Trans. on Power Electron.*, vol. 32, no. 5, pp. 3754–3766, May 2017.
- [77] B. P. Reddy, B. P. Reddy and K. S. Kumar, “Asymmetrical 7-level neutral point clamped converter for switch reluctance motors,” in *Proc. Int. Conf. Power Electron. Smart Grid, Renew. Energ.* Cochin, India, Jan. 2020, pp. 1–6.
- [78] J. Liang, D. H. Lee, and J.W. Ahn, “Direct instantaneous torque control of switched reluctance machines using 4-level converters,” *IET Elect. Power Appl.*, vol. 3, no. 4, pp. 313–323, Jul. 2009.
- [79] M. M. Bosra, M. Saniei and R. Kianinezhad, “Direct instantaneous torque control of switched reluctance motors using five level converter,” in *Proc. Int. Univ. Power Eng. Conf.*, Soest, Germany, Sept. 2011, pp. 1–6.
- [80] S. Song, C. Peng, Z. Guo, R. Ma and W. Liu, “Direct instantaneous torque control of switched reluctance machine based on modular multi-level power converter,” in *Proc. Int. Conf. Elect. Mach. Syst.*, Harbin, China, Aug. 2019, pp. 1–6.
- [81] A. D. Cheok and Y. Fukuda, “A new torque and flux control method for switched reluctance motor drives,” *IEEE Trans. Power Electron.*, vol. 17, no. 4, pp. 543–557, Jul. 2002.

- [82] P. K. Reddy, D. Ronanki, and P. Parthiban, “Direct torque and flux control of switched reluctance motor with enhanced torque per ampere ratio and torque ripple reduction,” *Electron. Lett.*, vol. 55, no. 8, pp. 477–478, Apr. 2019.
- [83] N. Yan, X. Cao, and Z. Deng, “Direct torque control for switched reluctance motor to obtain high torque–ampere ratio,” *IEEE Trans. Ind. Electron.*, vol. 66, no. 7, pp. 5144–5152, Jul. 2019.
- [84] A. Dekka, D. Ronanki, K. R. Pittam, P. Perumal and A. R. Beig, “Modified direct torque and flux control of switched reluctance motor drive with reduced source current ripple for vehicular applications,” in *Proc. IEEE Appl. Power Electron. Conf. Expo.*, New Orleans, USA, Jun. 2020, pp. 2920–2925.
- [85] R. B. Inderka and R. W. A. A. De Doncker, “DITC—Direct instantaneous torque control of switched reluctance drives,” *IEEE Trans. Ind. Appl.*, vol. 39, no. 4, pp. 1046–1051, Jul. 2003.
- [86] H. Zeng, H. Chen, and J. Shi, “Direct instantaneous torque control with wide operating range for switched reluctance motors,” *IET Electr. Power. Appl.*, vol. 9, pp. 578–585, 2015.
- [87] J. Castro, P. Andrada, and B. Blanqué, “Minimization of torque ripple in switched reluctance motor drives using an enhanced direct instantaneous torque control,” in *Proc. Int. Conf. Elect. Mach.*, Marseille, France, Sept. 2012, pp. 1021–1026

- [88] S. Wang, Z. Hu and X. Cui, “Research on novel direct instantaneous torque control strategy for switched reluctance motor,” *IEEE Access*, vol. 8, pp. 66910-66916, Apr. 2020.
- [89] J. W. Jiang, B. Bilgin, and A. Emadi, “Three-phase 24/16 switched reluctance machine for a hybrid electric powertrain,” *IEEE Trans. Transport. Electrific.*, vol. 3, no. 1, pp. 76–85, Mar. 2017.
- [90] K. M. Rahman and S. E. Schulz, “High-performance fully digital switched reluctance motor controller for vehicle propulsion,” *IEEE Trans. Ind. Appl.*, vol. 38, no. 4, pp. 1062–1071, Jul./Aug. 2002.
- [91] Y. Sozer, D. A. Torrey, and E. Mese, “Automatic control of excitation parameters for switched-reluctance motor drives,” *IEEE Trans. Power Electron.*, vol. 18, no. 2, pp. 594–603, Mar. 2003.
- [92] B. Fahimi, G. Suresh, J. P. Johnson, M. Ehsani, M. Arefeen, and I. Panahi, “Self-tuning control of switched reluctance motors for optimized torque per ampere at all operating points,” in *Proc. Annu. Appl. Power Electron. Conf. Expo.*, Feb. 1998, pp. 778–783.
- [93] X. D. Xue, K. W. E. Cheng, J. K. Lin, Z. Zhang, K. F. Luk, T. W. Ng, and N. C. Cheung, “Optimal control method of motoring operation for SRM drives in electric vehicles,” *IEEE Trans. Veh. Technol.*, vol. 59, no. 3, pp. 1191–1204, Mar. 2010.

- [94] C. Mademlis and I. Kioskeridis, “Gain-scheduling regulator for high-performance position control of switched reluctance motor drives,” *IEEE Trans. Ind. Electron.*, vol. 57, no. 9, pp. 2922–2931, Sept. 2010.
- [95] R. Gobbi and K. Ramar, “Optimisation techniques for a hysteresis current controller to minimise torque ripple in switched reluctance motors,” *IET Electr. Power Appl.*, vol. 3, no. 5, pp. 453–460, Sep. 2009.
- [96] H. Hannoun, M. Hilairet, and C. Marchand, “Comparison of instantaneous and average torque control for a switched reluctance motor,” in *Proc. IEEE Int. Symp. Ind. Electron.*, Cambridge, U.K., 2008, pp. 675–680.
- [97] H. Hannoun, M. Hilairet and C. Marchand, “Design of an SRM speed control strategy for a wide range of operating speeds,” *IEEE Trans. Ind. Electron.*, vol. 57, no. 9, pp. 2911–2921, Sep. 2010.
- [98] H. Cheng, H. Chen, and Z. Yang, “Average torque control of switched reluctance machine drives for electric vehicles,” *IET Electr. Power Appl.*, vol. 9, no. 7, pp. 459–468, Aug. 2015.
- [99] X. Li and P. Shamsi, “Model predictive current control of switched reluctance motors with inductance auto-calibration,” *IEEE Trans. Ind. Electron.*, vol. 63, no. 6, pp. 3934–3941, Jun. 2016.
- [100] X. Li and P. Shamsi, “Inductance surface learning for model predictive current control of switched reluctance motors,” *IEEE Trans. Transport. Electrific.*, vol. 1, no. 3, pp. 287–297, Oct. 2015.

- [101] C. Li, G. Wang, Y. Li and A. Xu, “An improved finite-state predictive torque control for switched reluctance motor drive,” *IET Elect. Power Appl.*, vol. 12, no. 1, pp. 144-151, 1 2018.
- [102] C. Hui, M. Li, W. Hui, S. Q. Shen, and W. Wang, “Torque ripple minimization for switched reluctance motor with predictive current control method,” in *Proc. Int. Conf. Elect. Mach. syst.*, Sydney, Australia, 2017, pp. 1–4.
- [103] R. Abdel-Fadil and L. Szamel, ”Enhancement Of the Switched Reluctance Motor Performance for Electric Vehicles Applications Using Predictive Current Control,” *2018 International IEEE Conference and Workshop in Obuda on Electrical and Power Engineering (CANDO-EPE)*, Budapest, pp. 195–200, 2018.
- [104] R. Tarvirdilu-Asl, S. Nalakath, B. Bilgin and A. Emadi, “A Finite control set model predictive torque control for switched reluctance motor drives with adaptive turn-off angle,” in *Proc. 45th Annu. Conf. IEEE Ind. Electron. Soc.*, Lisbon, Portugal, 2019, pp. 840-845.
- [105] D. S. Reay, M. Mirkazemi-Moud, T. C. Green, and B. W. Williams, “Switched reluctance motor control via fuzzy adaptive systems,” *IEEE Control Syst.*, vol. 15, no. 3, pp. 8–15, Jun. 1995.
- [106] S. Mir, M. E. Elbuluk, and I. Husain, “Torque-ripple minimization in switched reluctance motors using adaptive fuzzy control,” *IEEE Trans. Ind. Appl.*, vol. 35, no. 2, pp. 461–468, 1999.

- [107] L. O. A. P. Henriques, P. J. C. Branco, L. G. B. Rolim, and W. I. Suemitsu, “Proposition of an offline learning current modulation for torque-ripple reduction in switched reluctance motors: Design and experimental evaluation,” *IEEE Trans. Ind. Electron.*, vol. 49, no. 3, pp. 665–676, Jun. 2002.
- [108] M. Ma, F. Ling, F. Li and F. Liu, “Torque ripple suppression of switched reluctance motor by segmented harmonic currents injection based on adaptive fuzzy logic control,” *IET Electr. Power Appl.*, vol. 14, no. 2, pp. 325–335, 2020.
- [109] C. Shang, D. Reay, and B. Williams, “Adapting CMAC neural networks with constrained LMS algorithm for efficient torque ripple reduction in switched reluctance motors,” *IEEE Trans. Control Syst. Technol.*, vol. 7, no. 4, pp. 401–413, Jul. 1999.
- [110] N. C. Sahoo, J. X. Xu, and S. K. Panda, “Low torque ripple control of switched reluctance motors using iterative learning,” *IEEE Trans. Energy Convers.*, vol. 16, no. 4, pp. 318–326, Dec. 2001.
- [111] B. Bilgin, J. W. Jiang, and A. Emadi, *Switched Reluctance Motor Drives: Fundamentals to Applications*. Boca Raton, FL, USA: CRC Press, ch. 4, pp. 141–154, Apr. 2019.
- [112] S. Song, L. Ge, S. Ma, M. Zhang and L. Wang, “Accurate measurement and detailed evaluation of static electromagnetic characteristics of switched

- reluctance machines,” *IEEE Trans. Instrum. Meas.*, vol. 64, no. 3, pp. 704–714, Mar. 2015.
- [113] B. Parreira, S. Rafael, A. J. Pires, and P. J. Costa Branco, “Obtaining the magnetic characteristics of an 8/6 switched reluctance machine: From FEM analysis to the experimental tests,” *IEEE Trans. Ind. Electron.*, vol. 52, no. 6, pp. 1635–1643, Dec. 2005.
- [114] S. Boyd and L. Vandenberghe, *Convex Optimization*. Cambridge, U.K.: Cambridge Univ. Press, Mar. 2004.
- [115] A. Ruszczyński, “Unconstrained optimization of differentiable functions,” in *Nonlinear Optimization*. Princeton, NJ, USA: Princeton University Press, 2006.
- [116] Z. Xia, S. Nalakath, R. Tarvirdilu-Asl, Y. Sun, J. Wiseman, and A. Emadi, “Online optimal tracking method for interior permanent magnet machines with improved MTPA and MTPV in whole speed and torque ranges,” *IEEE Trans. Power Electron.*, vol. 35, no. 9, pp. 9755–9771, Sept. 2020.